Fast Simulation Methods for Non-Planar Phase and Multilayer Defects in DUV and EUV Photomasks for Lithography

Michael Lam

Electrical Engineering and Computer Sciences
University of California at Berkeley

December 19, 2005

Fast Simulation Methods for Non-Planar Phase and Multilayer Defects in DUV and EUV
Photomasks for Lithography

by

Michael Christopher Lam

B.S. (University of California, San Diego) 2001
B.A. (University of California, San Diego) 2001
M.S. (University of California, Berkeley) 2003

A dissertation submitted in partial satisfaction of the requirements for the degree of
Doctor of Philosophy
in

Applied Science and Technology

in the

GRADUATE DIVISION

of the

UNIVERSITY OF CALIFORNIA, BERKELEY

Committee in charge:

Professor Andrew R. Neureuther, Chair
Professor Jeffrey Bokor
Professor John Strain

Fall 2005

Fast Simulation Methods for Non-Planar Phase and Multilayer Defects in DUV and EUV
Photomasks for Lithography

© 2005

by

Michael Christopher Lam

Abstract

Fast Simulation Methods for Non-Planar Phase and Multilayer Defects in DUV and EUV
Photomasks for Lithography

by

Michael Christopher Lam

Doctor of Philosophy in Applied Science and Technology

University of California, Berkeley

Professor Andrew R. Neureuther, Chair

This dissertation develops rapid modeling methodologies for the printability and inspectability of various types of defects on photomasks in DUV and EUV lithography. Several fast and approximate methods for defect simulation are introduced and validated by comparing their results with Finite Difference Time Domain (FDTD) calculations of scattering from the same geometry. The common strategy is to decompose the electromagnetic (EM) scattering into individual signal contributions by analyzing rigorous simulations, and then to develop efficient alternative models for each contribution.

Two methods are introduced to calculate the observed scattering from DUV phase defects. First, the through focus behavior of an isolated defect can be used to extract two defect parameters, size and phase, which fully characterize the defect by means of an EM equivalent thin mask model. Post and void defects can also be differentiated based on the side of defocus that their peak signal occurs. Second, a defect projector methodology is introduced that allows results for an isolated defect and a defect-free pattern to be combined to predict their interaction for any defect location. The defect projector is four orders of magnitude faster than 3D FDTD simulation, and can correctly predict the defect induced dimension change to within 30% for worst case.

1

The main emphasis of this dissertation is on scattering from non-planar multilayer structures to understand the printability of buried defects inside of EUV mask blanks. A new method based on ray tracing is developed by exploiting the small non-specular forward angular scattering of individual bilayers, which is 10X smaller than the back scatter, and its approximation as zero allows a new and tractable mathematical factoring. The method is tested for various deposition strategies, defect sizes, defect shapes, as well as various illumination angles of incidence and polarization. Smoothing of the defect shape during deposition is confirmed to help mitigate isolated defect printability to a size less than about 70nm for 3D defects. The method is 4 to 5 orders of magnitude faster than FDTD simulation, takes 40X less memory, and still achieves equivalent accuracy. FDTD results for resonant multilayers were also found to suffer from convergence lulls and reflection errors at angles >10º due to small wavelength shifts from numerical dispersion.

The new methodology is then extended to model the interaction between absorber features and buried defects by developing a new 2D thin mask model for features. FDTD studies of signal components from an isolated absorber edge show that the scattering can be approximated to first order by adding phased line sources to vertically propagating waves at the edges of the thin mask model. The ray tracing method was also extended to model the case of optical inspection of EUV masks. The Single Surface Approximation and ray tracing method produce nearly identical results, while FDTD suffers from numerical errors due to the abnormally high cell densities of 700 cells per wavelength.

                                              _____

Professor Andrew R. Neureuther

Committee Chairman

Dedicated to my grandparents,
who worked so hard so that I may have a better life

Acknowledgements

Table of Contents

Index of Acronyms

ACR	Analytic Correction for Resonance
CAD	Computer Aided Design
CD	Critical Dimension
CEF	Corner Error Function
DDM	Domain Decomposition Method
DUV	Deep Ultra-Violet
EM	Electromagnetic
EUV	Extreme Ultra-Violet
EUVL	Extreme Ultra-Violet Lithography
FBC	Fourier Boundary Condition
FDTD	Finite Difference Time Domain
FWHM	Full Width at Half Maximum
FFT	Fast Fourier Transform
GHz	Giga-Hertz
GTD	Geometrical Theory of Diffraction
IC	Integrated Circuit
IFFT	Inverse Fast Fourier Transform
LTE	Low Thermal Expansion
MBW	Multiply Bounced Wave
MMFE	Model Method by Fourier Expansion
NA	Numerical Aperture
NILS	Normalized Image Log Slope
NMSE	Normalized Mean Square Error
OPC	Optical Proximity Correction
PRW	Primary Reflected Wave
PSM	Phase Shifting Mask
PTW	Primary Transmitted Wave
PWA	Primary Wave Approximation
RCWA	Rigorous Coupled Wave Analysis
RET	Resolution Enhancement Technique
RU	Rayleigh Unit
SSA	Single Surface Approximation
TE	Transverse Electric
TM	Transverse Magnetic
TRW	Total Reflected Wave
TTL	Through the Lens
TTW	Total Transmitted Wave

1   Introduction

1.1 Motivation

Technology has become critically necessary to design and build even newer technology, and this is especially true today in optical lithography for semiconductor manufacturing. Computer simulation has become an integral part of the lithographic process for quickly and efficiently examining the design and production of Integrated Circuits (ICs). However, newly designed microprocessor complexities grow faster than the computational power of available processors and demand ever increasing accuracy within a shorter span of time. This is because the physical and mathematical models used to predict imaging have become increasingly detailed and rigorous, and often need to be applied to every feature in the layout to pre-compensate the design. These detailed models are thus a significant increased burden to engineering design.

The necessity of rigorous models combined with their computational constraints, has created a movement to develop new fast-CAD simulation paradigms that retain the necessary accuracy, but with dramatic increases in speed. These paradigms often leverage a problem's physical characteristics to allow new approximations to be exploited. New paradigms have been successful implemented on several fronts. Model based Optical Proximity Correction (OPC) methods [1], Domain Decomposition Methods (DDM) [2,3], Boundary Layer Methods [4], and the Single Surface Approximation (SSA) [5] are just a

few of the fast simulation methods that have been proposed or adopted within the industry. Fast simulation methodologies enhance the quality and quantity of information that can be used to support the design process, and will become even more important as the industry moves towards a fully virtual manufacturing process, whereby all aspects are simulated prior to first silicon.

This dissertation explores two new forms of fast-CAD simulation paradigms for the electromagnetic scattering from defective photomasks. The goal is to identify new approximations that can be leveraged to enable fast diffraction calculations at Deep Ultra Violet (DUV) and Extreme Ultra Violet (EUV) wavelengths. The strategy here is to decompose a complex domain into individual pieces and understand how each individual piece behaves. Then the linearity of a defect's electric field, combined with the non-linearity of the total intensity, will enable approximations based on perturbation theory [6]. Finally, the resulting approximations are used to build a variety of new methods that are accurate, require fewer computational resources, and significantly quicker at evaluating and adjusting the hundreds of millions of scenarios in a design.

1.2 The Defect Printability Challenge

All photomasks contain defects, but not all defects cause defective products. A major problem in lithography deals with understanding which defects are critical (will create a defective product) and which defects do not impair the end product. When a photomask is found to be defective, the mask must either be fixed (defect removed) or remade (a respin). Modern photomasks have become very expensive, making it

prohibitively expensive to continuously respin a mask until it is defect free. It is therefore necessary to understand how many critical defects exist on the photomask, and fix only the critical defects. This problem becomes more pronounced since photomask complexity rises with the complexity of new ICs, increasing both the number and probability of critical defects on the mask. A delicate minimization is sought which ensures the photomask is free of critical defects, while avoiding the cost of unnecessary mask respins. Simulation can be used to differentiate critical defects from non-critical defects to help minimize the cost of generating an acceptable photomask.

Defects, however, are particularly challenging to simulate, since they can occur in any location, near any feature and be of any size, 3-D shape, and material. Understanding how each of these parameters affects defect printability requires numerous simulations. Additionally, defect sizes are typically sub-wavelength, creating interesting electromagnetic effects that cannot be accurately captured in simple scalar diffraction theory. It has been shown that "real" defects behave electromagnetically different from their ideal physical dimensions [7], confirming that their sub-wavelength nature requires more time-consuming rigorous models to be used when determining their imaging severity. Combining both the large parameter space and the need for rigorous models, it becomes easy to understand why fast and accurate methods would be a boon to defect printability studies.

1.3 Dissertation Content

The dissertation begins by reviewing relevant background material on optical lithography, its EUV extensions, and computational methods in Chapter 2. Special emphasis is placed on the imaging behavior of phase defects and their impact on the printability of features. These concepts are then extended to extreme ultra violet lithography (EUVL) and defective EUV mask blanks, where a phase defect is manifested via particles buried underneath multilayer mirror structures. Finally, current simulation techniques that are relevant to the dissertation content will be reviewed, which include Domain Decomposition Methods (DDM), Finite Difference Time Domain (FDTD) [8], the Single Surface Approximation (SSA), and others.

Chapter 3 looks into the limits on the applicability of edge-DDM. As mask dimensions shrink, electromagnetic cross-talk between adjacent and connecting edges becomes more pronounced until these effects can no longer be ignored, and the mask structure can no longer be thought of as a sum of diffractions from isolated edges. An understanding of the threshold for electromagnetic cross-talk among edges is important for assessing when the edge-DDM method is applicable for a given layout. General rules of thumb are developed to determine the smallest feature size that edge-DDM may accurately simulate to the desired tolerance. The concept of a defect projector is also introduced, which allows a large number of defect locations to be accurately examined in a short amount of time. The accuracy and speed of this method will be discussed in greater detail. Finally, an interesting and challenging question is whether or not edge-DDM can be used quickly and accurately for the simulation of photomasks during

inspection. If true, a very fast die-to-database comparison may be made during inspection where the database will be synthesized "on the fly" from edge-DDM. The applicability of edge-DDM for inspection is assessed, and a new corner-DDM is proposed for mitigating the high frequency errors of edge-DDM.

Chapter 4 addresses the troubling problem that phase-shifting mask (PSM) defects, as observed in experiment, do not perform as their ideal counterparts in thin mask simulations. Specifically, a 3 parameter model is demonstrated to be sufficient to link together these seemingly contradictory results. Since at small dimensions, the size and magnitude of phase defects are degenerate, only 2 of the 3 parameters are necessary to characterize their focal behavior, allowing two physically different defects to become indistinguishable when comparing their scattered fields. Data extraction from the behavior of real defects can then be used to find electromagnetically equivalent ideal defects that can be simulated much quicker. Intuitive physical explanations are also given for understanding why real and ideal defects behave differently.

Chapter 5 reexamines the physical characteristics of the buried defect problem within EUVL and describes a new method for rapidly simulating buried defects within EUV mask blanks. The optical homogeneity and smoothness of EUV mask blanks, combined with the small numerical aperture of the EUV optical system, allow efficient and accurate simulations to be accomplished in very minimal time, and thus opens the door to more thorough, quantitative studies on buried defect printability. The optical homogeneity of the multilayer stack also allows a primary wave approximation to be used, where only the primary wave scattering of the defective layers is computed. The primary wave scattering is then only allowed to interact with the defect-free structure for

the purposes of calculating the interaction resonance, effectively casting the new method as a perturbational approach.

A comparison between the new method and two popular methods for simulating EUV buried defects is presented in Chapter 6. These are the FDTD method and the SSA method. The Chapter's goals are to understand the tradeoffs in accuracy to achieve speed, and address the memory constraints (2GB limit) of large problems on single desktop computers. The goal of the new method is to produce orders of magnitude improvement in speed for 2D and 3D simulations, and make the results at least as reliable and accurate as the FDTD method, which is generally considered to be the "gold standard" for simulating EUV buried defects. This includes testing the accuracy for various shapes and sizes of defects, for various locations within the multilayer stack, for off-axis illumination, as well as both the standard and the smoothing multilayer growth methods. A speed analysis of the three methods will show that the new method in 3D is 5 orders of magnitude faster than FDTD and uses about 40X less memory.

In studying the accuracy of the new method, it was required to make a careful investigation of the FDTD method, and this is also included in Chapter 6. A surprising result was uncovered that questions the underlying assumption that FDTD is a gold standard for simulations at EUV wavelengths. When using FDTD to simulate EUV multilayers, a temporary lull in convergence can be obtained as resonant energy gathers coherence within the multilayer, slowly leaking energy out until equilibrium is reached. The effects of numerical dispersion on the calculated reflectivity of the EUV multilayers are also documented. Numerical dispersion changes the simulated wavelength by fractions of a percent, which is normally not noticeable for most applications; however,

the resonant nature of the multilayer enhances the sensitivity of the structure to small wavelength changes. Numerical dispersion is shown to significantly impact the diffracted spectrum for angles greater than about 9º.

Chapter 7 will show applications of the new simulator to predict the printability impact of various defect types on EUV multilayer blanks. Understanding the defect's electromagnetic signature and printability becomes crucial to understanding the necessary levels of inspection and tolerances needed for producing acceptable mask blanks for the semiconductor industry. While several programmed defect printability studies have been performed over the years [9,10,11], thorough and predictive defect landscape maps are still needed. Therefore, landscape maps that vary the aspect ratios and defect shapes will be presented for both 2D and 3D defects. These maps can be used as engineering tools for developing defect size and density requirements on the production of EUV mask blanks. General rules of thumb are developed to aid engineers when determining the printability of defects.

Finally, Chapter 8 will explore the extension of the new buried defect simulator to inspection and for predicting defect-feature interactions. Many options exist for the inspection of EUV mask blanks [12, 13], including optical inspection at 488nm or 266nm wavelengths and actinic (at wavelength) inspection. Both types of inspection involve using light to illuminate a mask blank and looking for deviations from the background intensity. In the case of actinic inspection, the new method should provide excellent results, since the wavelength used to inspect the system remains unchanged relative to the wavelength used during printing. For inspection at optical wavelengths, the assumptions exploited in the new method are changed due to the higher material refractive index and

absence of resonant reflection. An assessment of the new method's performance in simulating the inspection case will be presented. A systematic method for understanding EUV buried defect printability in the presence of features is also shown.

1.4 Dissertation Contributions

Chapters 3 and 4 contain data for simulating phase defects at DUV wavelengths and attempt to bridge the gap between "ideal" defects and "real" defects. The defect projector presented in Chapter 3 is a new method that will allow engineers to rapidly sift through the large defect parameter space to hone in on critical defects or find feature areas that are sensitive to defects that need to be monitored closely during production. It combines the scattered fields of the defect and the feature (neglecting re-scattering), and is validated through simulation of a PSM. Also, edge-DDM was augmented by the use of a new corner-DDM, which can enable the application of DDM for inspection simulations. The major contribution of Chapter 4 is a method for extracting equivalent thin mask defect model parameters from the focal behavior of real defects, allowing equivalent ideal defects to be simulated very rapidly in lieu of the real defect.

By far, the major contributions of the dissertation are contained within Chapters 5-8. The introduction of a new simulation methodology in Chapter 5 will allow the vast parameter space of defective EUV mask blanks to be explored more thoroughly than was possible before. The computational constraints of simulating 3D buried defects for EUV have been significantly reduced. Time requirements have dropped by 5 orders of

magnitude and memory requirements have been reduced by 40X, allowing formerly intractable simulations to be performed on a desktop machine.

The accuracy (Chapter 6) of the new simulator will provide even more reliable information from simulation than was possible with FDTD. The simulation problems uncovered when applying the FDTD method to resonant multilayers allow a greater physical understanding of the complicated scattering that occurs inside a resonant cavity prior to equilibrium. The new method was successfully used to generate defect printability maps in Chapter 7, which will help set engineering tolerances for the production of new EUV mask blanks. Finally, the extensions discussed in Chapter 8 will further aid in understanding buried defect printability in the presence of features, as well as the development of inspection systems for EUVL mask blanks. The new simulation approach will also aid other areas of research involving optically homogeneous materials where non-planar, stratified media might occur. Other applications of x-ray and EUV optics such as astronomical telescopes [14] could be impacted as well.

2   Background

This Chapter reviews a number of key aspects of projection printing at DUV and EUV wavelengths that are utilized in describing the technical challenges, simulation methods, and design studies in this dissertation. The following review is by no means complete, as it focuses on only the relevant details to later chapters. The reader is encourage to read the texts [15,16,17] to obtain further details on the optical science, [18,19,20] for semiconductor manufacturing and the lithographic process, as well as the mathematical models describing the system.

2.1 Optical Lithography

A typical lithography imaging tool is shown in Figure 2.1 and contains three major aspects: the illumination system, the photomask, and the projection optics. Each aspect of the tool is highly engineered to provide maximum resolution and image quality. The individual photomasks are the objects that can be imaged by the lithography tool.

2.1.1 Resolution

The resolution, R, of a lithography tool is dependent on the wavelength of the light used to illuminate the photomask, as well as the numerical aperture (NA) of the imaging optics:

$$R = k_1 \frac{\lambda}{NA}$$

Modern steppers and scanners at the 90nm node use a DUV excimer laser at a

wavelength of 193nm. A typical NA for a modern tool is around 0.85 and is expected to

grow to 1.05 – 1.2 in immersion lithography. The k1 parameter is usually on the order of

0.6 and is called the "technology factor", which encompasses all the engineering

Resolution Enhancement Techniques (RETs) (off-axis illumination, sub-resolution assist

features, etc) that can push the resolution smaller [21,22]. Using the typical parameters
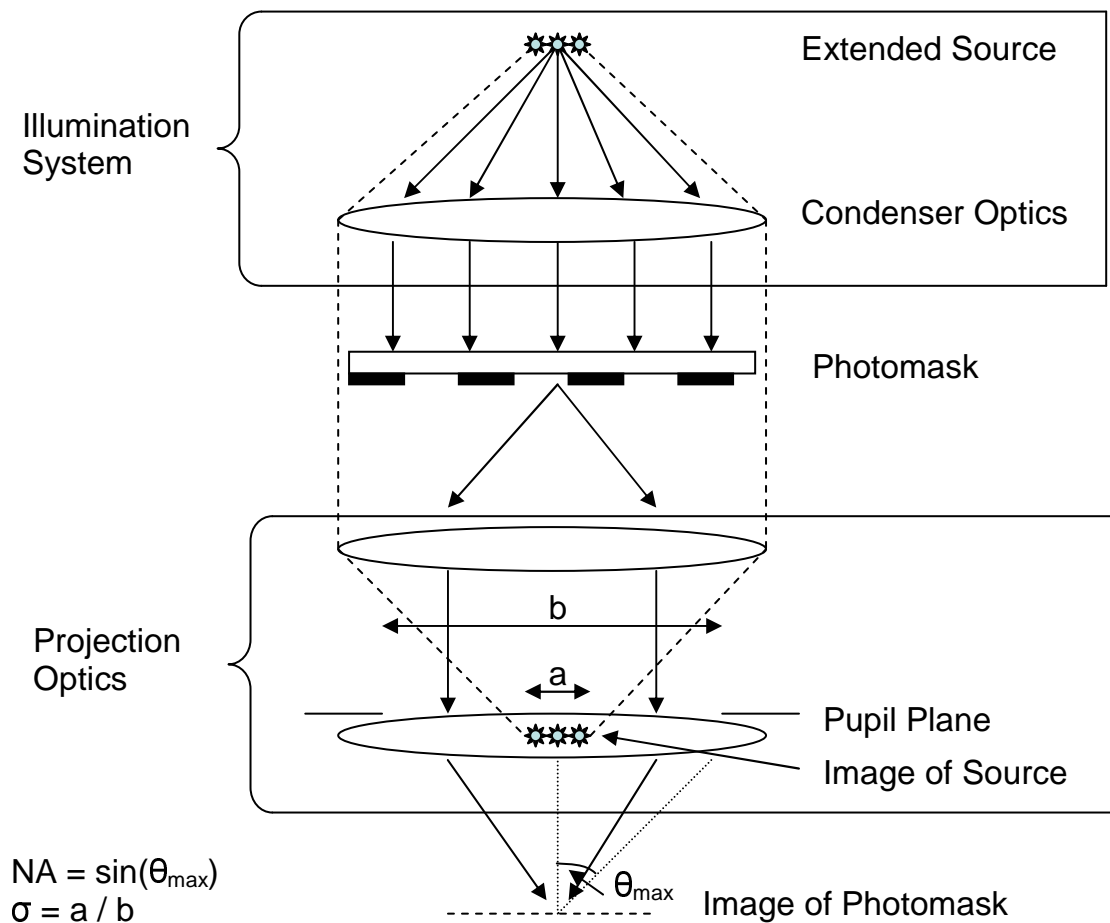
Figure 2.1. A schematic of an optical lithography system.

given above, a k1 factor of about 0.40 is needed to make semiconductor products at the 90nm node.

2.1.2 Illumination System

The illumination system is typically a Kohler illumination system, which places an image of the source into the pupil plane of the projection optics. Kohler systems allow all aspects of the object to be imaged equally well, providing uniform image quality regardless of location on the photomask. The illumination system provides a uniform set of plane waves which diffract as they pass through the photomask and are collected by the projection optics. The angular spectrum of plane waves illuminating the mask, which is called the partial coherence and is denoted by the parameter σ, can alter the resolution of the entire system. Pistor [23] showed that for modeling projection printing, the observed mask scattering is constant for illumination angles within 10º of normal incidence. This observation allows a single computation of the mask diffraction to be used for all illuminating plane waves when simulating the projection imaging optics. Inspection systems, however, allow illumination angles that are much greater than 10º, and therefore require multiple calculations of the mask scattering at different angles of incidence. Multiple diffraction calculations increases the required simulation time by at least 5X, making inspection simulations difficult to complete. Thus, fast simulation methods could have a major impact on inspection simulations.

2.1.3 Projection Optics and Final Image

Calculating of the image from an arbitrary mask can be performed by Fourier transforming the electric field directly below the photomask, producing a plane wave decomposition of the fields. These plane waves are then low-pass filtered by the angular acceptance cone of the projection optics at the pupil plane, whose maximum angle is given by:

$$\theta_{max} = \sin^{-1}(\frac{NA}{R})$$

Where R is the reduction of the system, usually 4X. The projection optics integrate the partially coherent illumination to reproduce a demagnified image of the photomask down at the image plane. A silicon wafer is coated with a photosensitive chemical, called photoresist, and placed into the image plane. The photoresist changes chemical properties based on its exposure to light, and can then be developed. Further processing steps can be used to transfer the pattern onto the silicon wafer itself.

2.1.4 Photomasks and their defects

The photomask is a 6x6 inch square piece of quartz (glass) that is covered with a very thin layer (~80nm) of chrome on one side. Patterns can be etched into the chrome that will allow light to pass through the photomask, and the patterns can then be imaged by the lithography tool. These masks are referred to as "binary", since light is either blocked (0) or transmitted (1). Defects located on binary masks are either opaque (pinspot) or clear (pinhole). An opaque defect is a piece of chrome that was incorrectly left within a clear transmissive area, usually because a small piece of photoresist was never removed. Clear defects are chrome regions that should be dark, but have a piece of
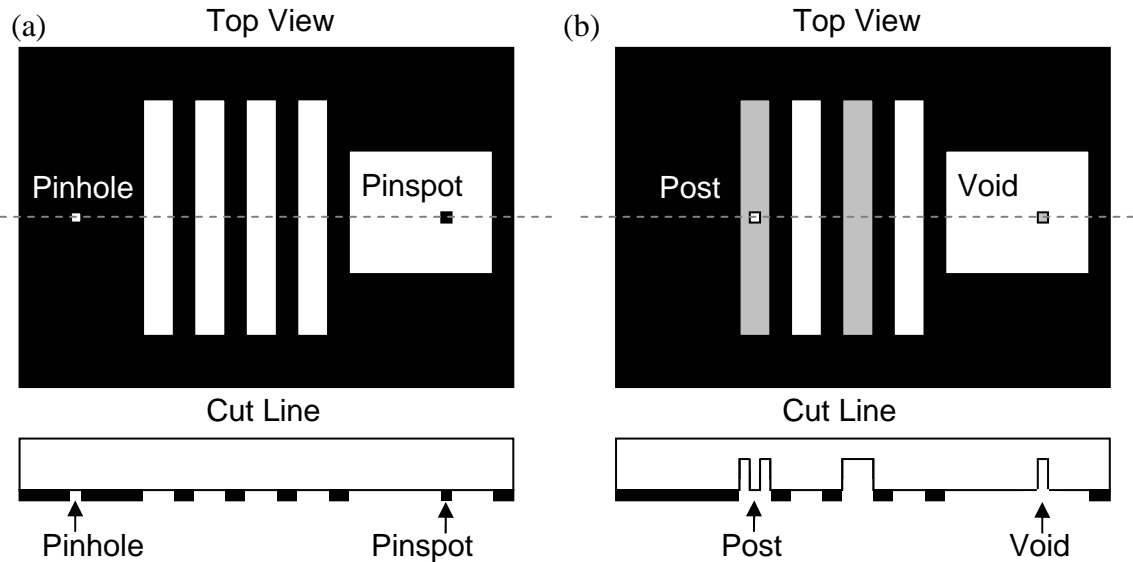
Figure 2.2. (a) Example of a binary mask with pinhole and pinspot defects. (b) Example of a PSM with post and void defects.

chrome missing, usually because a small piece of photoresist was inappropriately removed. Figure 2.2a shows the top view and the associated cut line of an example binary mask, along with both an opaque and a clear defect.

Phase-shifting masks (PSMs) are similar to binary masks, except that some of the quartz is etched away within various clear regions on the mask. These trenches allow light to be slowed less and emerge phase shifted relative to other clear areas where no trenches are present. The possibility of generating electric fields with various phases results in more favorable imaging. The removal of quartz from clear regions on the mask gives rise to a new type of defect: the phase defect. Phase defects might arise during etching of the mask substrate as posts of incompletely etched material in phase shifted regions due to pin spots of resist, or as voids etched through pin holes in nominally unshifted regions. Figure 2.2b shows the top view and the associated cut line of an example PSM, along with a post and void defect. With the introduction of phase-shifting masks in projection printing, the ability to screen phase defects for their impact on

14

imaging is very important. Because these defects change the phase of the light passing through clear regions, their imaging severity can be significantly worse than simple binary defects. Additionally, since the phase of the defect can interplay with phase changes in defocus, the worst case printability may not even be at best focus [24].

Unfortunately, the characterization of the printability of phase defects on PSMs is very complex. Recent work by Adam, et al. [7] shows that phase defects do not behave electromagnetically as their physical phase height indicates, as expected from using an ideal mask model with scalar diffraction theory. Electromagnetic effects produce defects with different average brightness (amplitude squared) and lower average phase beneath the geometrical shadow of the defect. Rigorous methods are therefore required to accurately predict the printability of phase defects, however, the general imaging behavior of phase defects can be understood by simple algebraic models.

2.1.5 Algebraic Defect Models

Since Chapter 4 will introduce a method for extracting 3 defect parameters (its area A, its amplitude M, and its phase φ_{defect}) for use in previous scattering models, it is useful to review them. Algebraic models for clear and opaque defects have been demonstrated by Neureuther, et al. [25] and Mastromarco, et al. [26]. These defect models were then extended to phase defects by Neureuther [27]. Each model was based on perturbation theory and confirmed from simulations with the aerial image simulator SPLAT[28].

The electric fields from a defective feature can be decomposed into the electric field from a defect free feature, combined with the electric field from an isolated, clear or opaque defect:

Equation 2.1: $\qquad E_d = kA = kd^2 \qquad$ Where $\qquad E_c = E_f \pm E_d$

where E_c is the composite field, E_f is the feature field, and E_d is the defect field which is proportional to its area (d^2). The feature and defect fields are added (if a clear defect) or subtracted (if an opaque defect). The image formed from this small perturbation on the feature's field becomes:

$$I_c = (E_c)^2 = (E_f)^2 \pm 2\mu_{eff}E_f E_d + (E_d)^2$$

which can be further simplified to:

$$I_c \approx I_f \pm 2\mu_{eff}E_f E_d$$

when the defect is sufficiently small. The parameter μ_{eff} is the mutual coherence function, which is determined by the partial coherence (σ) and the defect's distance away from the feature edge.

The change in intensity produced by the defect can now be expressed as:

$$\Delta I = I_c - I_f = \pm 2\mu_{eff}E_f E_d$$

The above equation shows that the electric field of the defect can coherently interact with the electric field from a nearby feature, demonstrating how a nominally subprintable isolated defect, can become printable in the presence of features. Thus, the evaluation of critical defects cannot be determined by looking just at the defect's own characteristics, the feature must also be included. Finally, the change in CD can be determined by knowledge of the defect free feature's slope:
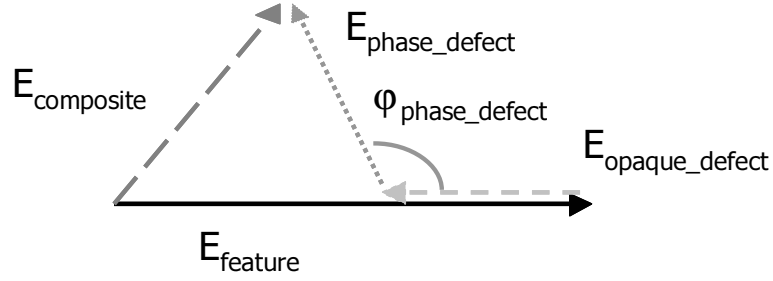
Figure 2.3. Vector addition representation of algebraic model for phase defects. An opaque defect's E-field is first subtracted from the features E-field, the phase defect reinjects the E-field at a phase changed angle, resulting in the composite E-field.

Equation 2.2: $\qquad \Delta CD = \dfrac{\Delta I}{\dfrac{dI_f}{dx}} = \dfrac{\pm 2\mu_{eff} E_f E_d}{\dfrac{dI_f}{dx}}$

The extension of Equation 2.2 to phase defects simply requires a factor of [1-Mcos(φ_{defect})], representing the defect as first subtracting out the light, and then injecting the light back into the structure with an different phase.

$$E_c = E_{feature} - E_{opaque\_defect} + E_{phase\_defect}$$

$$= E_{feature} - E_{opaque\_defect}[1 - M\cos(\varphi_{defect})]$$

Since

$$E_{phase\_defect} = Me^{j\varphi_{defect}} E_{opaque\_defect}$$

This process can be understood by the vector addition shown in Figure 2.3, producing a final form of:

Equation 2.3: $\qquad \Delta CD = \dfrac{\Delta I}{\dfrac{dI_f}{dx}} = \dfrac{\pm 2\mu_{eff} E_f E_d[1 - M\cos(\varphi_{defect})]}{\dfrac{dI_f}{dx}}$

2.2 EUV Lithography

Extreme Ultra Violet Lithography (EUVL)[29] is conceptually similar to optical lithography and the entire mathematical framework for imaging at optical wavelengths is applicable to EUV wavelengths as well. EUVL is a promising candidate for imaging below the 32nm node, since it provides a large potential resolution enhancement from the 13.4nm wavelength light (nearly 15X better than 193nm optical lithography). The potential increase in resolution is tempered, however, since the optical system must be implemented much differently. Materials are both highly absorptive (large k), and are optically homogeneous since their refractive indices are very close to air (n=1). The optical homogeneity of materials makes it very difficult to bend or focus EUV wavelengths to high angles, resulting in systems with that are based on reflective optics with smaller NAs (NA = 0.3). The reflective optics require the EUV imaging system to be telecentric about an off-axis angle, which is nominally about 6º. Pistor [30] discusses some of the computation challenges of calculating aerial images from a telecentric EUV system. The reflective optics are constructed via a multilayer, which forms the basic unit of the EUV optical system. The mask blanks are also made of these multilayers, which are described in more detail in the next section.

2.2.1 EUV Mask Blanks and Buried Defects

EUVL mask blanks consist of a multilayered structure (usually 40 bilayers) of alternating silicon and molybdenum layers, sitting atop a Low Thermal Expansion (LTE)
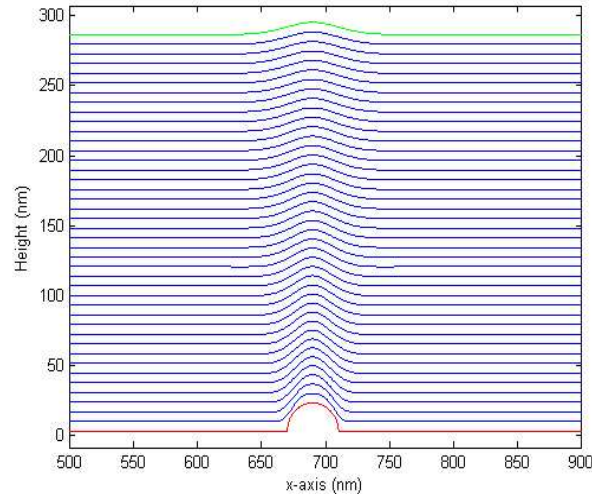
Figure 2.4. EUVL mask blank with buried defect.

substrate. The spacing between each layer is tuned such that incident radiation on each

surface will be reflected in phase with every other surface in the multilayer, essentially

satisfying the Bragg reflectivity condition [31]. A typical layer for silicon and

molybdenum will be 4.14nm and 2.76nm thick, respectively. A thin capping layer (made

of ruthenium or silicon) is deposited on top of the multilayer to resist oxidation and other

aging effects. Researchers have shown that reflectivities as high as ~70% are achievable

with appropriate multilayer spacings [29]. The EUVL mask blank is prone to defects

buried underneath the multilayer, which disrupt the coherent multilayer spacings, and

produce a dip in the reflected field. Such defects arise when the LTE substrate is non-

planer or when a particle falls on the substrate prior to multilayer coating. Most of these

buried defects are typically molybdenum or silicon agglomerations that form during the

deposition process [72]. One example of a buried defect is shown in Figure 2.4. These

buried defects are analogous to phase defects in optical lithography, since they locally

change the phase of the reflected field within open areas.

One of the major obstacles in EUVL is the production of defect free mask blanks, which is considered to be a possible "show stopper" for the implementation of the technology. The improved resolution allows for better imaging of very small defects. Compounding this problem is that a small, localized, substrate defect is broadened upon deposition of the multilayer, allowing subprintable defects to become printable as multilayers are deposited. These "decorated" defects [32] are quite numerous and cause many problems. Buried defects also present complications because they are very difficult, if not impossible, to repair. Various techniques [33,34] have been proposed to fix different EUV defect types. E-beam techniques [35] lower the defect height by contracting the local volume of the multilayer, but are not practical since they result in a broad destruction of the multilayer surrounding the defect as well. The inability to repair buried defects means that a mask blank will have potential "land mines" sitting beneath the surface, whose presence may become known depending on which features are placed around the defect (as shown in section 2.1.5). The use of OPC methods has been proposed to help correct the imaging characteristics when such an event occurs [36].

The physical scattering of a buried defect depends on the manner in which the layers above it are deposited. Work as been done to characterize defect printability[37], as well as to develop a coating process that will help smooth away residual traces of the substrate defect as each layer is grown[38,39,40,41]; a useful mathematical model for describing the smoothing process has been shown by Stearns [42]. The smoothing process uses a combination of deposition and etching to hide a substrate defect's physical presence at the multilayer surface. Figure 2.5 shows the same substrate defect in Figure 2.4, except coated by the new smoothing deposition, using Stearn's growth model. The

20
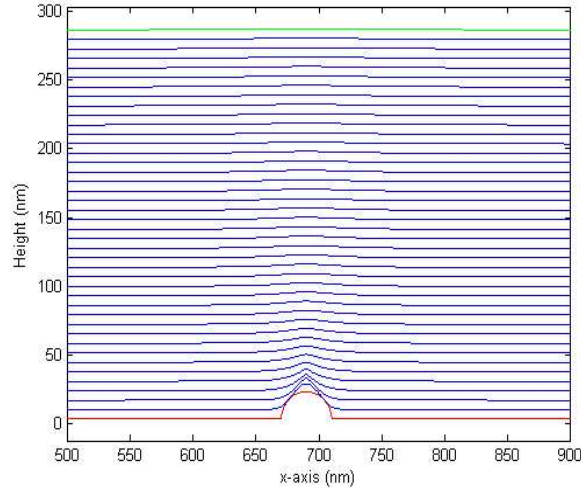
Figure 2.5. EUVL mask blank with buried defect coated with the smoothing technique.

physical height at the surface of the multilayer is dramatically reduced when using the

smoothing deposition technique, and thus, the imaging severity as well. Predicting the

imaging behavior of smoothed defects will be critical to evaluating the future use of the

smoothing technique. Stearns' model will be used extensively in this dissertation to

model EUV buried defects, to allow reflection comparisons between normal deposition

methods and the smoothing method.

The top surface of the mask blank can be coated with a patterned absorbing

material, as shown in Figure 2.6. Various thicknesses and materials have been proposed
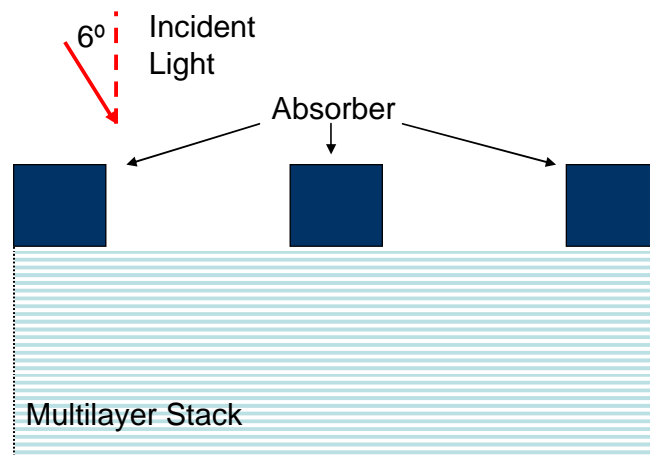
Figure 2.6. Example of a full EUVL patterned mask.

for the absorbing layer, such as 70nms of TaN or 100nms chrome [73]. All options for

the absorbing layer pose complications since they are all electrically thick (many

wavelengths thick), opening the possibility of numerous electromagnetic effects that

could complicate the observed scattering. In fact, the off-axis nature of an EUV optical

system creates an intrinsic horizontal and vertical bias for the imaging system [43], as

features aligned in certain directions cast geometric shadows from the off-axis

illumination. The patterned absorber can also suffer from the clear and opaque defects

that were discussed earlier; however, they can be fixed by the same methods used on

optical lithography masks.

2.2.2 Simulation Methods for EUV Buried Defects

Early defect simulations were performed with thin mask models [44] in an

attempt to understand the general defect behavior in the EUV regime; however, the

electrically thick nature of an EUV mask implies that a rigorous simulation methodology

is needed to correctly compute its scattering. The multilayer stack of a 40 bilayer mask

blank is over 20λ thick, and the absorbing material placed on top adds at least another 5λ.

Additionally, the simulation method must be robust enough to handle substrate defects

coated with both the smoothing deposition and standard deposition. Many researchers use

electromagnetic field (EMF) solvers to compute the scattering from an EUV mask, and

Finite Difference Time Domain (FDTD) is one of the most popular numerical methods

for EMF solvers.

FDTD simulators such as UC Berkeley's TEMPEST[8] are often referred to as

"rigorous" or "thick mask" simulators because they actually solve Maxwell's equations

on a discretized grid for the steady state solution to an electromagnetic problem. They are

very accurate and are considered to be a "gold standard" for computing mask diffraction;

however, FDTD also requires long simulation times and large amounts of memory, even

in 2D. EUV simulations in 3D require about 12 hours to run and 2Gbs of memory on

modern computers for even a small 250nm by 250nm patch of mask blank. Various

authors [45,46] have implemented example FDTD flows for EUV simulation of buried

defects. Memory requirements explode since the electrically large mask geometries

(simulation domains) require sub-nanometer discretizations to accurately resolve the

individual layers in the bilayer. Even sub-nanometer discretizations are insufficient to

guarantee the correct geometry resolution since an arbitrary free flowing line will be

geometrically approximated by boxes when the domain is discretized, transforming

smoothly varying layers into boxy, crude lines. Deng [47,48] showed that these boxy

lines can cause significantly incorrect reflections to be computed unless blended

materials are used for the EUV multilayers. Figure 2.7 shows the benefits of using
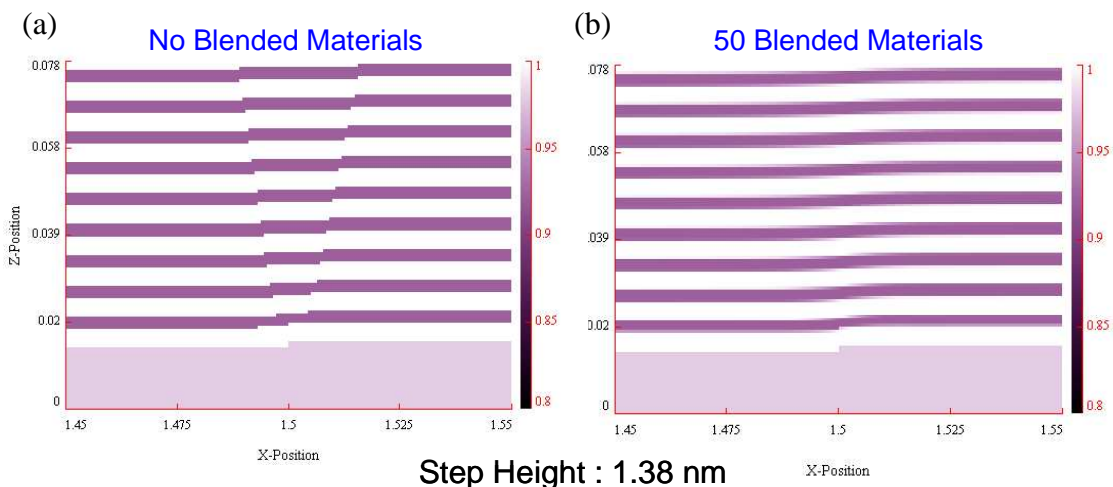
Figure 2.7. (a) EUVL mask blank geometry representation with 1.38nm step height without using blended materials. Notice the two prominent dislocations moving upwards. (b) same EUVL mask blank geometry using blended materials. The dislocations have been smoothed away.

23

blended materials for more accurate geometrical representations on an EUV multilayer. Pistor [49] introduced the Fourier Boundary Condition (FBC) which linked FDTD methods for EUV features with an analytic representation of the multilayer, which greatly sped up calculations, but was limited to perfect multilayers.

Ito [50] has proposed an analytic method based on Fresnel reflections, which systematically separates the multilayer domain into vertical strips. These strips are then approximated as parallel multilayers based on their midpoint values, where the reflectivity from the strips (with varied d spacings) can be calculated by Fresnel equations. The full field can then be synthesized by taking the reflection from each strip as the local electric field value of the reflection. Hybrid methods have been proposed by Evanschitzky [51,52,53] and Sambale [54], by linking FDTD simulators together with variations on Ito's method to obtain calculations of buried defect printability in the presence of features. While these hybrid approaches are faster than traditional FDTD simulations, they still lack the required speed for thorough printability studies. Rigorous coupled wave analysis[1] (RCWA) [55] has been used to accurately simulate 2D buried defects in the presence of features, with greatly reduced time relative to FDTD [56,57]. RCWA methods, however, suffer from a lack of extendibility to arbitrary 3D geometries, and no examples of 3D scattering have been published to date. Simplified modal methods have also been proposed based on the Rayleigh method [58]. Bollepalli [59] implemented a simulation method which uses scattering theory [60] to understand defect printability.

Finally, the Single Surface Approximation (SSA) [5] simply uses the top surface of the defective multilayer structure and converts it into a thin mask transmission function by turning the geometrical height variation across the surface into a phase

---

[1] Also called "Modal Method by Fourier Expansion" (MMFE)

mapping across the domain. The phase is then multiplied by a factor of 2 to account for the roundtrip of the reflection. The phase from a reflected surface is computed by the simple equation:

Equation 2.4: $$\varphi(x) = 2k(z(x) - z_0) = \frac{4\pi(z(x) - z_0)}{\lambda}$$

Where $z(x)$ is the surface height, z_0 is the surface height of the defect free surface, k is the wave number, and λ is the wavelength. This simple approach contains a number of assumptions that limit its broad application, but has been found to work relatively well at small defect sizes[61]. First, it assumes that all the layers beneath the surface layer are identical in shape to the top surface layer. A quick look at Figure 2.4 or 2.5 will show that this assumption is not very good unless the defect is very small. Second, it assumes that no amplitude disruptions occur in the near field. Investigations of defect printing will later show that this assumption is also false. Finally, the SSA method assumes that light is normally incident on the mask, and thus can never capture asymmetries that arise from the off-axis telecentricity of the EUV system. All of these assumptions significantly break down when the defect is large, or when it is coated with the smoothing process. The SSA approach achieves more than enough speed and, despite its assumptions, gives a good indication of the defect's behavior, but it lacks the required accuracy for quantitative study unless working in a tight range of applicability [5].

2.3 Domain Decomposition Methods

Adam introduced edge-DDM [2] which consists of first fracturing the mask geometry into a set of its edges, and then combining the electromagnetic spectra of each isolated edge from a library of presimulated, rigorous 2D edge diffractions. Edge-DDM has provided a simple method to simulate any arbitrary, Manhattan geometry (especially large 3D structures) to an accuracy level equal to rigorous thick mask simulations with a speed that facilitates very large scale mask calculations. The initial results at optical wavelengths [2,62,63] are truly spectacular, and DDM has been used to simulate scattering from EUVL patterned masks [3] with good results as well.

For its implementation, the library should contain the edge diffraction data from all types of edges that will be encountered in the mask geometry. The edge fracturing of an arbitrary layout is demonstrated in Figure 2.8. Horizontal and vertical edges will be
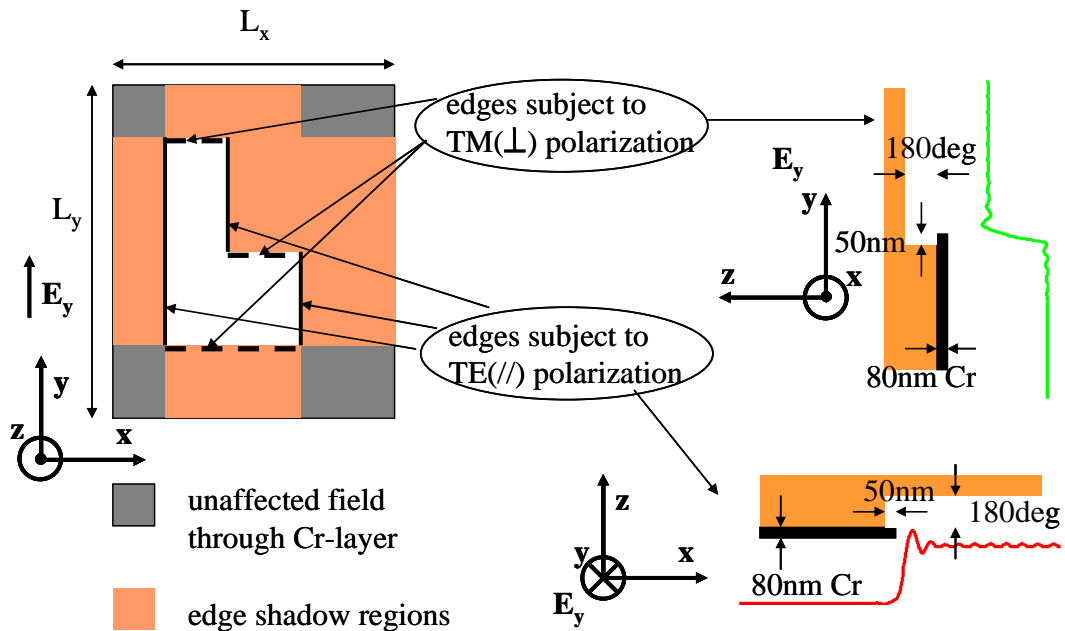
Figure 2.8. Shows the decomposition of an arbitrary domain into its edges.
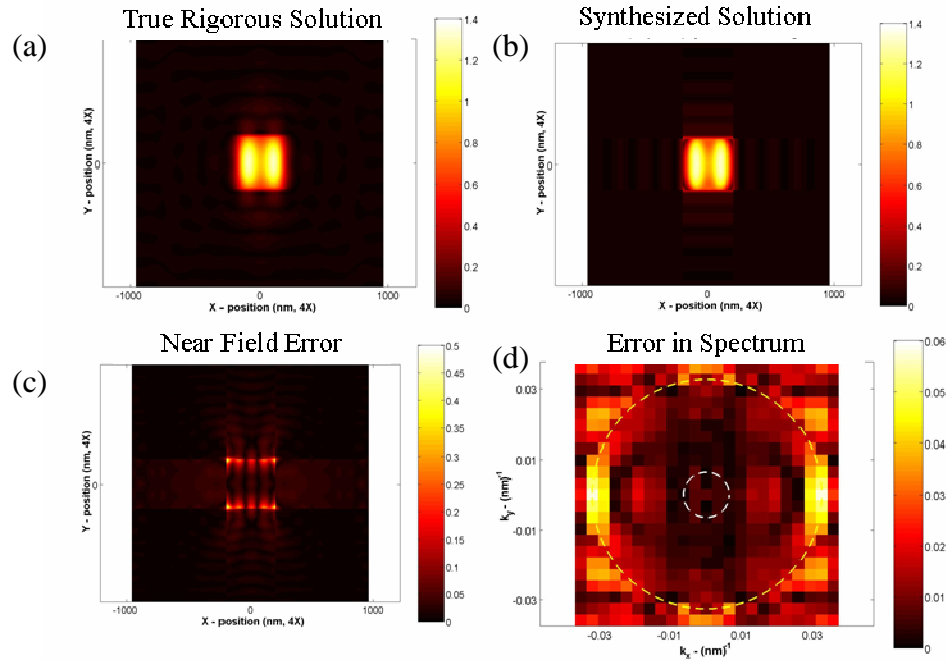
Figure 2.9. (a) The rigorous FDTD solution for TE fields passing through a 400x400nm contact. (b) The synthesized fields (edge-DDM) of the same contact. (c) The amplitude of the complex near field error between the rigrous and synthesized solutions. (d) The FFT of the near field error.

exposed to different polarizations. Certain regions on the mask will be unaffected by the 2D edge diffractions and are assigned values from rigorous 2D simulations of a closed chrome mask (ie. chrome background transmission). The addition of the many diffractions will produce areas that have overlapping, multiple clear field transmissions and/or chrome background transmissions. Appropriate subtractions of these background fields (both chrome transmission and open transmission) are then used to bring the final fields to their appropriate values (one clear field or one chrome transmission), resulting in a synthesized, approximate near electric field distribution for the original mask structure.

The accuracy of the synthesized fields is then compared with the truly rigorous simulation to determine the validity of the approximation by a simple subtraction of the two fields. While large errors (~ ½ of clear field value) may be seen locally within the corners of the structure (due to electromagnetic interactions from the two edges that are

not captured in the sum of its isolated edge diffractions), these large errors are mapped to high spatial frequencies that are scattered outside of the optical system. The resulting collected orders have very few errors compared to the fully rigorous solution. The normalized mean square error (NMSE) is used to quantify the magnitude of the errors in the collected Fourier components.

$$NMSE = \frac{\int |\,true - synth\,|^2}{\int |\,true\,|^2}$$

The 400nm x 400nm contact shown in Figure 2.9 demonstrates the process of obtaining and calculating the NMSE from a synthesized field solution. The corners of the contact show large errors in the electric fields (Figure 2.9c), which are mapped to the high spatial frequency components that scatter outside of the objective system (Figure 2.9d). The larger circle in Figure 2.9d represents the propagating orders ($\theta < 90°$), while inside the small circle indicates the orders collected by the imaging system. Edge-DDM effectively matches the Through the Lens (TTL) spectrum of the mask scattering, allowing it to be extremely accurate when compared to rigorous scattering calculations.

3   Extensions to Domain Decomposition Methods

The Domain Decomposition method (also referred to as edge-DDM) has proven to be a very useful tool for obtaining the mask diffraction spectrum from advanced photomasks. The speed and flexibility of the method has allowed Adam [64] to integrate rigorous mask scattering information into OPC methods, greatly improving the accuracy of corrections. Certainly, however, the approximation of independent scattering from each edge within the simulated domain will begin to break down as electromagnetic cross-talk from adjacent and connecting edges grows when feature sizes shrink. This Chapter will explore the domain of applicability for edge-DDM in greater depth, providing physical analysis for when the approximation begins to break down. Extensions to edge-DDM are also discussed, including a defect projector method that simultaneously projects the fields of an isolated defect along with a feature to obtain printability assessment of phase defects. Finally, it is shown that the high frequency errors in the edge-DDM approximation can be mitigated by including rigorous corner information when synthesizing the near fields.

3.1 Domain of Applicability for Edge-DDM

Simple 2D spaces were used to more fully define the region where edge-DDM begins to break down. The smallest feature dimension that can be accurately modeled will depend on the types of edges present in the layout. For example, a PSM has a well known strong dependence on edge side wall shape and is thus more challenging. It is therefore worthwhile to understand how these different edges affect the synthesis of the electric fields, as well as the feature CD.

Rigorous FDTD simulations were compared to edge-DDM synthesis of the fields for 2D spaces of different phases and different amounts of under etch, resulting in a systematic matrix of features. The basic geometry can be seen in Figure 3.1. The CD of the spaces was varied for each edge case, with values of 400nm, 300nm, 200nm, 150nm, 100nm, and 80nm. The domain size was 400 x 1 x 122 nodes with a grid size of 5nm. Figure 3.2 shows the NMSE plotted against the CD of the space in terms of lambda. The four graphs represent (a) a 0nm under etch of phase wells at 0°, 90°,180°,270°, and 360°, and (b) a 180° phase well with 0nm, 25nm, 50nm, 75nm, and 100nm under etch.

From Figure 3.2a and 3.2b, it is obvious that larger errors are seen at deeper phase
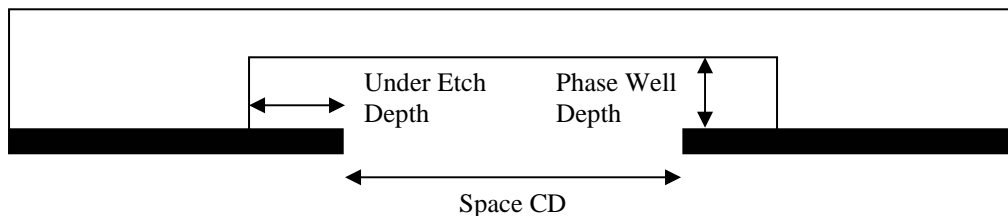
Figure 3.1. Phase well geometry.
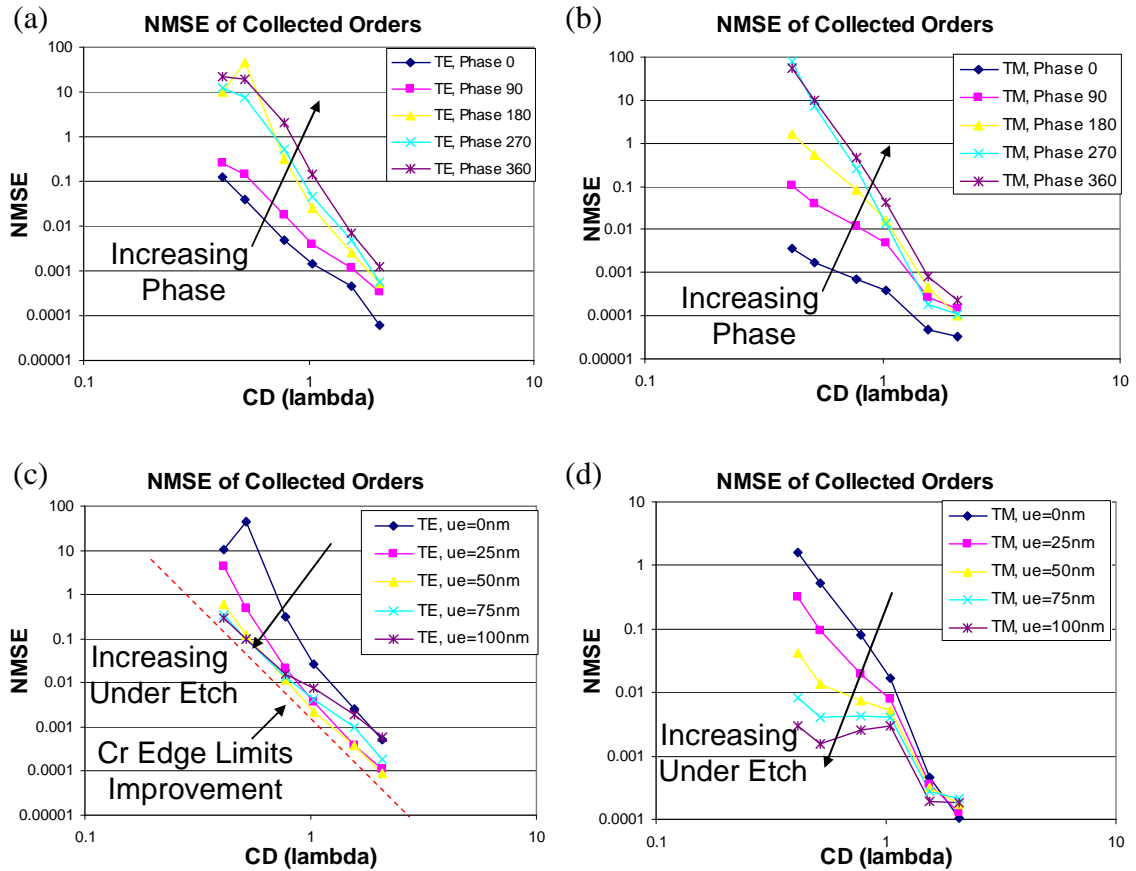
Figure 3.2. Shows the NMSE for both the TE and TM polarizations through CD (in λ)
(a) TE polarization with various phase well depths. (b) TM polarization with various phase well depths.
(c) TE polarization with various under etch depths. (d) TM polarization with various under etch depths.

wells for both polarizations. This increase in error is due to longer glass edges that can

scatter light and interact with the opposite edge. As a phase well becomes deeper, more

glass edge is created and this enables more interaction with surrounding edges. Larger

under etches reduce the errors made by the edge-DDM approximation. As can be seen in

Figure 3.2c and 3.2d, larger under etches push the glass walls farther apart so they do not

interact with surrounding edges until smaller CDs. The TE polarization is limited on its

improvement because as the glass edges are pushed farther away (from under etch), the

chrome edges still remain and become the dominant factor in determining edge-to-edge

interactions. The boundary conditions on the TE polarization (tangential E) require

31
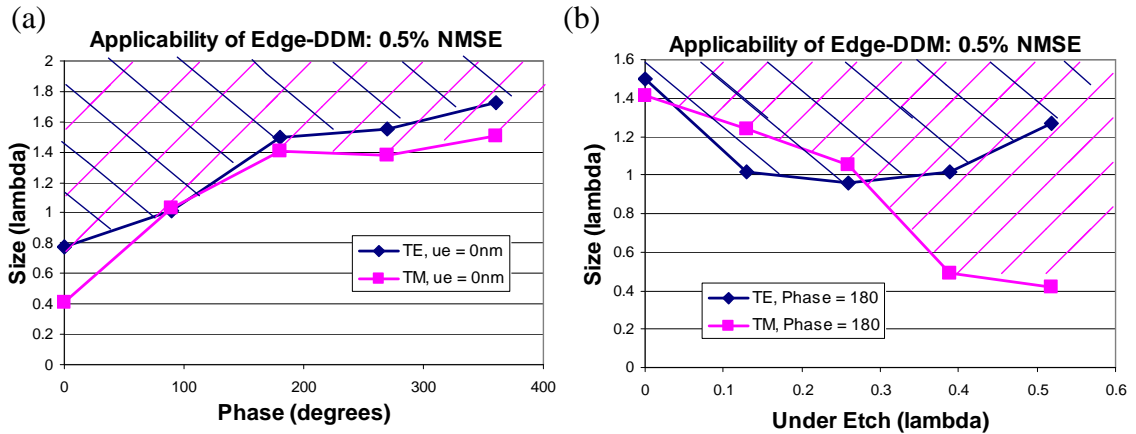
Figure 3.3. The curves represent contours of 0.5% NMSE in the fourier coefficients. (a) Smallest acceptable feature size for arbitrary phase well with no under etch. (b) Smallest acceptable feature size for arbitrary underetch for a 180° phase well.

continuity at the chrome edges, and thus constrain the fields in the gap by allowing the chrome edges to radiate and interact with each other. The TM polarization, however, has different boundary conditions at the chrome interface, allowing it (the perpendicular E field) to be discontinuous by the surface charge generated at the chrome interface. This means that the TM polarization will not be disturbed by, or scatter light towards, another chrome edge close to it, allowing the edges to act fairly independently, as assumed in edge-DDM. The resulting errors on the TM polarization are quite low, even at very small (as low as $.4\lambda$) dimensions.

The CDs (in λ) of the open space at the point where the NMSE crosses above a specified threshold are seen in Figure 3.3, as a function of phase (in degrees) and under etch depth (in λ). A NMSE of 0.5% has been chosen for the curves. The areas above the curves represent CDs that can be accurately modeled to the specified tolerance. These plots enable the generation of general rules of thumb on the applicability of edge-DDM for a specified domain. For an arbitrary layout, simply categorize the types of edges present in the layout, and find the smallest CD for each edge. These plots will give good

guidance as to how small of features can be accurately simulated for the given layout. Similarly, plots of all combinations of phases and under etches may be generated for all types of edges. A quick and easy reference for when edge-DDM is applicable, without the hassle of looking at charts, is to use the 2λ rule. Every situation that has been tested has given extraordinarily good results (NMSE$_{COLLECTED}$< 0.5%) when the CD spaces are $\geq 2\lambda$, regardless of edge type present in the layout.

From Figure 3.3, it also appears that in most cases the TE polarization will limit the smallest feature size that can be simulated accurately by edge-DDM. It is therefore possible to develop a simple heuristic that models the boundary interactions on the TE polarization once a specific CD has passed. This heuristic fix might increase the domain of applicability for edge-DDM to equal that of the TM polarization, resulting in $1 - 1.5\lambda$ minimum dimension for various applications.

3.2 Fast Defect Printability Assessment Using the Defect Projector

The challenge in assessing the impact of defects is that there is a multitude of ways in which they may appear. Defects come in various sizes, types, and phases, and may occur in any location in any feature on the layout. One rigorous simulation is necessary per instance of the defect, which can quickly become impossible to study since each simulation can take many hours to perform. A quick AND accurate way to simulate phase defects would enable much more detailed studies and allow phase defects to be more easily characterized. One way to obtain both the accuracy of the rigorous
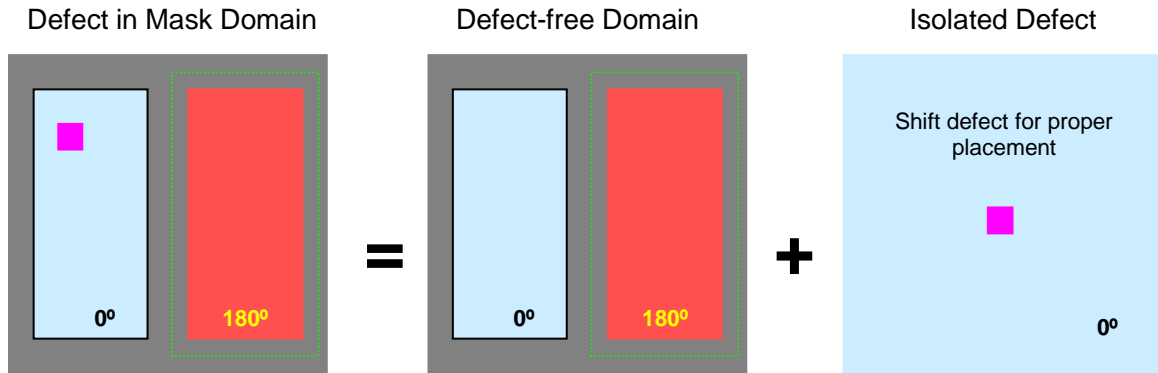
Figure 3.4. A schematic of the defector projector method. The defective mask can be thought of as a sum of the defect-free mask structure and the isolated defect (minus the appropriate background).

simulation, and a very large speed up in simulation time, is to use the concept of a defect projector.

Figure 3.4 demonstrates the concept of a defect projector. The full mask structure, including the defect, can be thought of as the simple sum of the defect-free structure plus the isolated defect, minus the appropriate background. These two sets of fields can be viewed as being projected simultaneously together to the wafer plane. A full characterization of each structure individually should lead to a full characterization of their combined structure, assuming minimal interactions between the two. In this sense, the defect projector is a perturbational method that assumes the fields from the defect are a small perturbation of the fields from the defect-free structure. The fields from the defect-free structure can be rigorously simulated if desired, but edge-DDM would be perfectly acceptable to synthesize these fields and have negligible errors in the accuracy. The isolated defect will be rigorously simulated and stored in the same library as the rigorous edge diffractions used for edge-DDM.

The power of this method is demonstrated in Figure 3.5, which shows an alternating phase shift mask structure with 18 positions marked for the placement of a

34
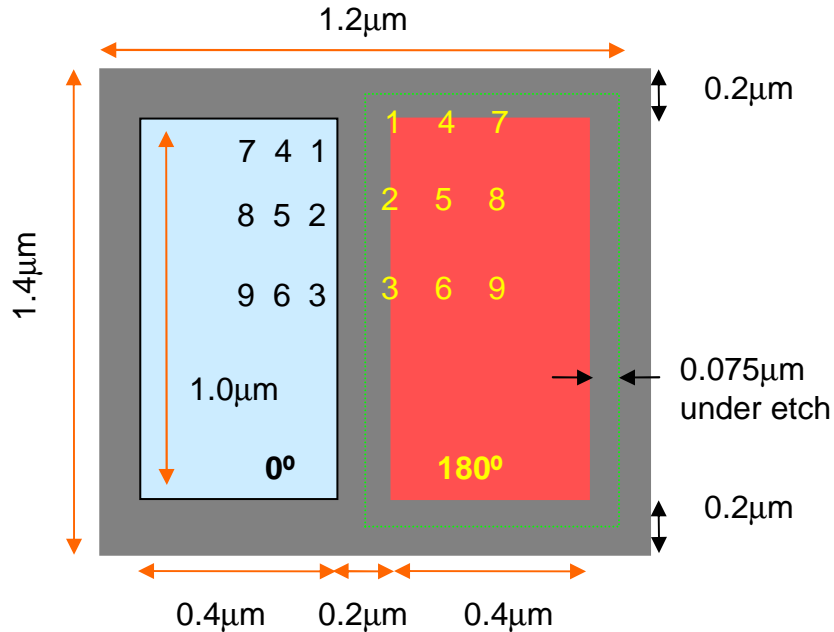
Figure 3.5. A schematic of an alternating phase shifting mask used to test the defect projector method. The numbers 1-9 represent 9 defect locations for a 180° phase pit (in the 0° region) and a 180° phase bump (in the 180° region). All dimensions at 4X.

0.12µm, 180° phase pit and a 0.12µm, 180° phase bump. Using conventional simulation methods, 36 rigorous simulations would have to be performed (one set of 18 for each polarization), with each simulation taking several hours each. Alternatively, the defect-free structure may be synthesized with edge-DDM and combined with the rigorously simulated isolated defects from a presimulated database to obtain the fields from ALL 36 simulations in a matter of seconds.

The 9 defect positions were rigorously simulated for both polarizations and for both types of phase defects (void and post), resulting in 36 rigorous simulations that took 7 - 15 hours each to run on a 699Mhz processor (each took differing amounts of time to converge). The aerial images for these rigorous simulations were then compared to the defect projector method which "simulated" all the fields within a few seconds. For those phase posts overlapping the under etch region, a simple geometrical blocking was used
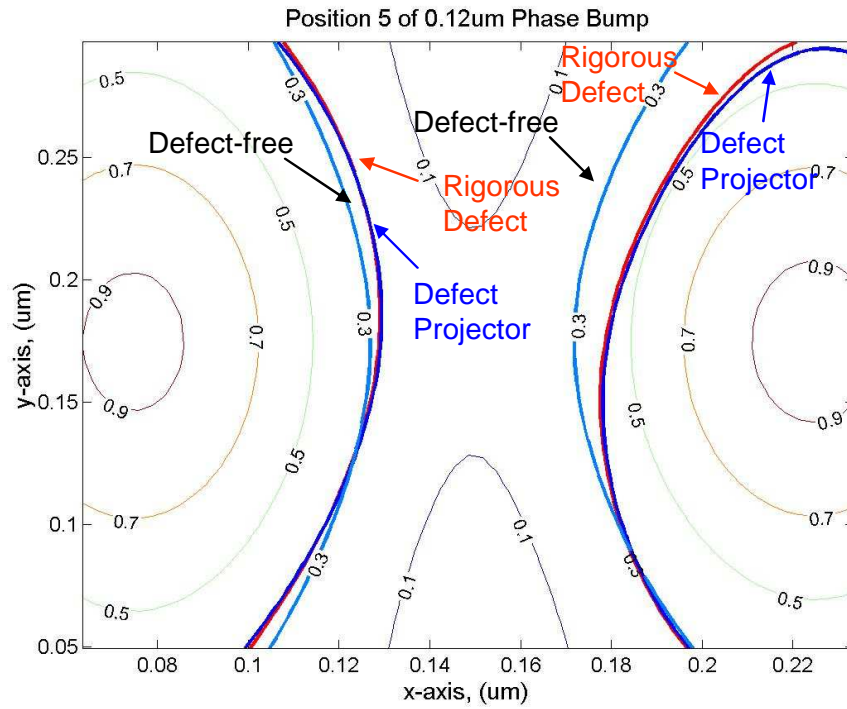
Figure 3.6. The zoomed aerial image contours of the gate CD from Figure 3.4 for defect location #5 of the 180 phase bump. All contours for the defect-free structure are given, in addition to the 0.3 contour of both the rigorous defect and the defect projector.
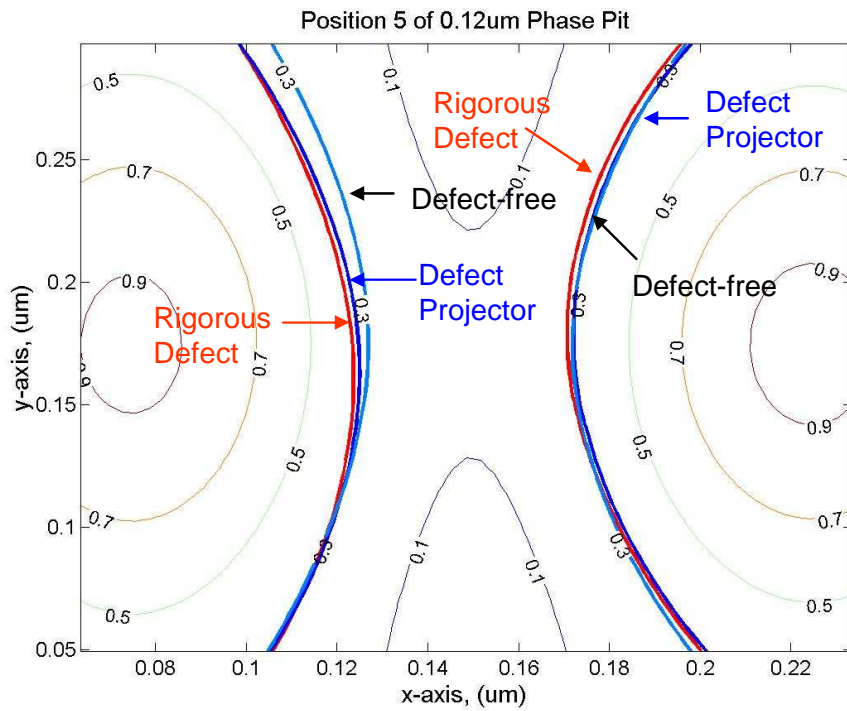
Figure 3.7. The zoomed aerial image contours of the gate CD from Figure 3.4 for defect location #5 of the 180 phase pit. All contours for the defect-free structure are given, in addition to the 0.3 contour of both the rigorous defect and the defect projector.

that set the defect's fields to zero in the region over the chrome area. The aerial image

contour at 0.3 intensity for the #5 defect position of the 180° phase bump is shown in

Figure 3.6. The CD of the line was predicted to within 3% for all simulations (error of

4nm in worst case), and the change in CD was predicted to within 30%. The test structure

from Figure 3.5, however, produces a very low NILS value due to its small scale relative

to the 193nm wavelength. The dimensions of the test structure were purposefully kept

small to lessen the 3D simulation requirements. Even with this low NILS value, the

defect projector was able to predict CD change to within 30%, and can be expected to

perform even better at higher NILS values. The CD values were also calculated for the

worst part of the line CD, near the base where the line met the outer lying structure.

Figure 3.7 shows the aerial image contour at 0.3 intensity for the #5 defect position of the

180° phase void. The Figure clearly shows the defect projector method is worst near the

base of the CD, but is much better for other portions of the line CD. The worst case

numbers, however, should give an upper bound on the error magnitude to be expected

from the method. The results from both types of defects are very promising, even for

those located close to the chrome where edge interactions are not captured. While the

defect projector did not predict the exact CD change of the rigorous simulations, it

nonetheless gives a very good idea of how the defect will perturb the line width. Given a

specific tolerance for the change in CD (such as 10%), all defects that change the line

width by 3% under the specified tolerance (such as 7%) may be thrown out as non-

critical. Those defect locations remaining could then be simulated rigorously to

understand their exact change in the CD.

3.3 Edge-DDM for Inspection

Since defects scatter light in a broad spectrum, inspection systems utilize 1X optical systems to enable higher NAs to collect more of the scattered light. The additional light collected by the inspection system allows the defect to be more clearly distinguished within the image. Appropriate measures to correct the defect can be taken once its location is known. Using larger σ's allows more oblique plane waves to strike the mask, which in turn allows more of the broadly scattered light from defects to enter the collection optic.

The NMSE of the 2D spaces shown in Figure 3.2 were recalculated for a 1X optical system at the same NA. For plane waves normally incident on the photomask, the diffracted orders have not changed, except that now more of the diffracted orders are being collected by our optical imaging system. The NMSE of the much larger collection radius is still within acceptable limits. Figure 3.8 shows the NMSEs of the collected orders for a 1X system imaging the 2D space at NA = 0.8, for various phases and under etches. The errors have not grown appreciably from the printing case, and are shown to still maintain good accuracy despite the larger collection optic. A subtle note, however, is that the wavelength used was 193nm and normalized by this amount. Inspection systems typically operate at higher wavelengths than those used during printing, and therefore a 180° phase well within a given layout will not correspond to 180° at the higher wavelengths. This change should be kept in mind when deciding the accuracy of edge-DDM for inspection compared to printing.

Obliquely incident waves were also used to simulate the same 2D structures. The edge-DDM becomes slightly more complicated than in the normal incidence case. The edge diffraction libraries must include the same edge types as before, except simulated at the oblique incidence desired and inspection wavelength. At oblique incidence, the addition of the two edge diffractions now must be modulated by a phase change. Since the incoming wave now has a lateral variation component given by k_x, the shifting of an edge from the edge diffraction library must also be accompanied by a change in phase appropriate to the amount of the edge shift based on the k_x value. Once the two edges have been added, the subtraction of the background field must be done with a plane wave
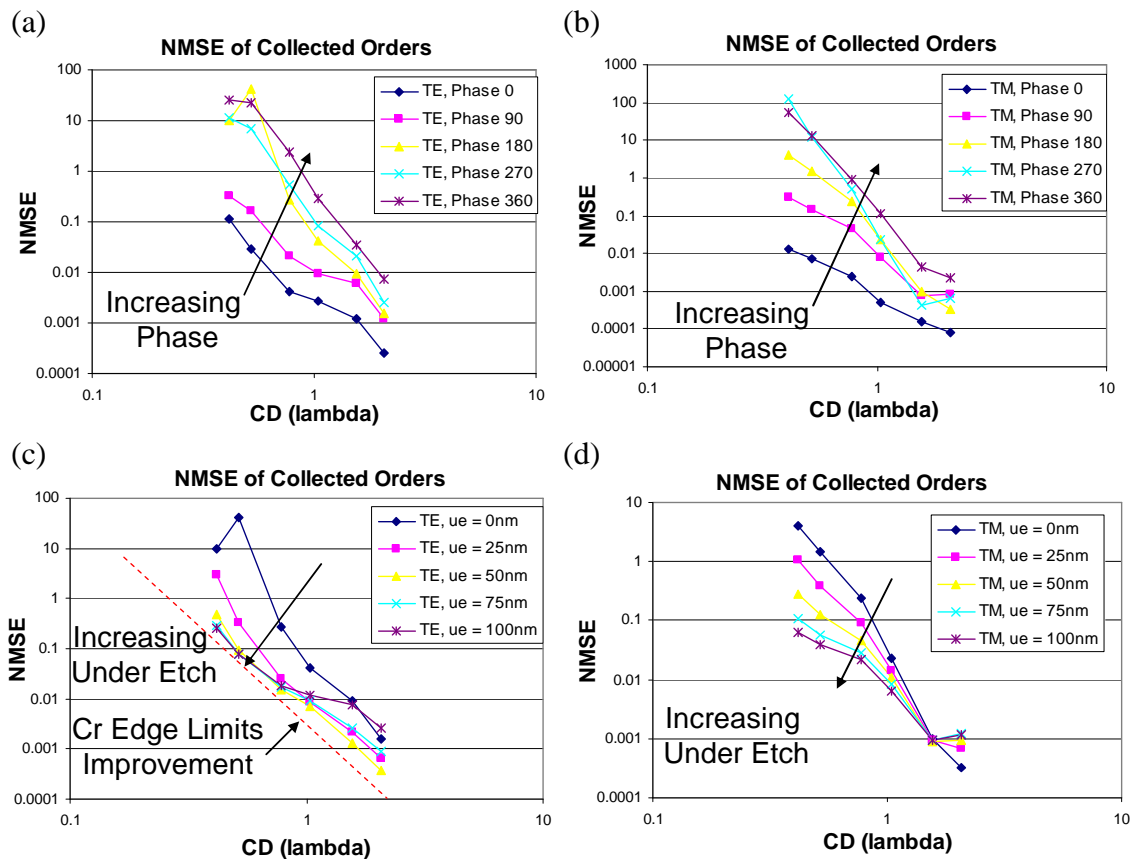
Figure 3.8. Shows the NMSE for a 1X inspection system (NA =0.8) for a normally incident plane wave. (a) TE polarization with various phase well depths. (b) TM polarization with various phase well depths. (c) TE polarization with various under etch depths. (d) TM polarization with various under etch depths.

at the same oblique incidence so that the phase matches the k_x wiggle across the

simulated domain. Additionally, for the comparison of the rigorous solution and the edge-

synthesized solution, another phase shift must be applied to remove the simulator's bias

on what phase is initiated at the start of the simulation domain.

Results from the edge synthesis for a 22.7º incident plane wave give mixed

results. While the edge-DDM results are only slightly worse compared to the results at

normal incidence, the errors are still contained within the high frequencies. Since edge-

DDM will always produce high spatial frequency errors, and since inspection systems

will always collect some of the high frequency components, edge-DDM applied to

inspection is limited in its accuracy. If, however, the high frequency terms could be

corrected in some manner, DDM might become a viable simulation tool for inspection.

3.3.1 Corner DDM

Referring to Figure 2.9c, most of the error in the edge-DDM approximation

occurs within the corners of the structure. It is most likely these corner errors that account

for a significant portion of the error obtained when using edge-DDM for inspection

simulations. A logical extension of the edge-DDM method is to simply use a corner-

DDM method, whereby large 3D corners are simulated and stored in the library. These

corners than then be used to synthesize the near field exactly akin to edge-DDM.

Obviously, more simulation time will be required to build the presimulated library,

however, the corner simulations will eliminate the largest source of error when applying

edge-DDM to inspection simulations. Corner effects can be seamlessly integrated into an

existing edge-DDM library by simply creating a Corner Error Function (CEF). A CEF is

Mask Corner: Corner Error Function (CEF)
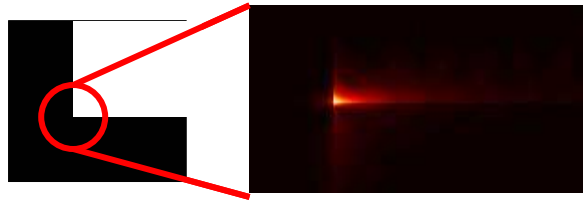
Figure 3.9. Near field view of a CEF to augment edge-DDM.

created by taking the simulated 3D corner and subtracting off the edge synthesized fields
from edge-DDM. The resulting field is the CEF and can be stored in the library:

$$CEF = E_{corner} - E_{edge-DDM}$$

The CEF, shown in Figure 3.9, simply becomes the original simulated corner when added
to an edge synthesized field, and is therefore a perturbational field that "fills in" the
missing corner information. Whenever corner information is needed, the CEF can be
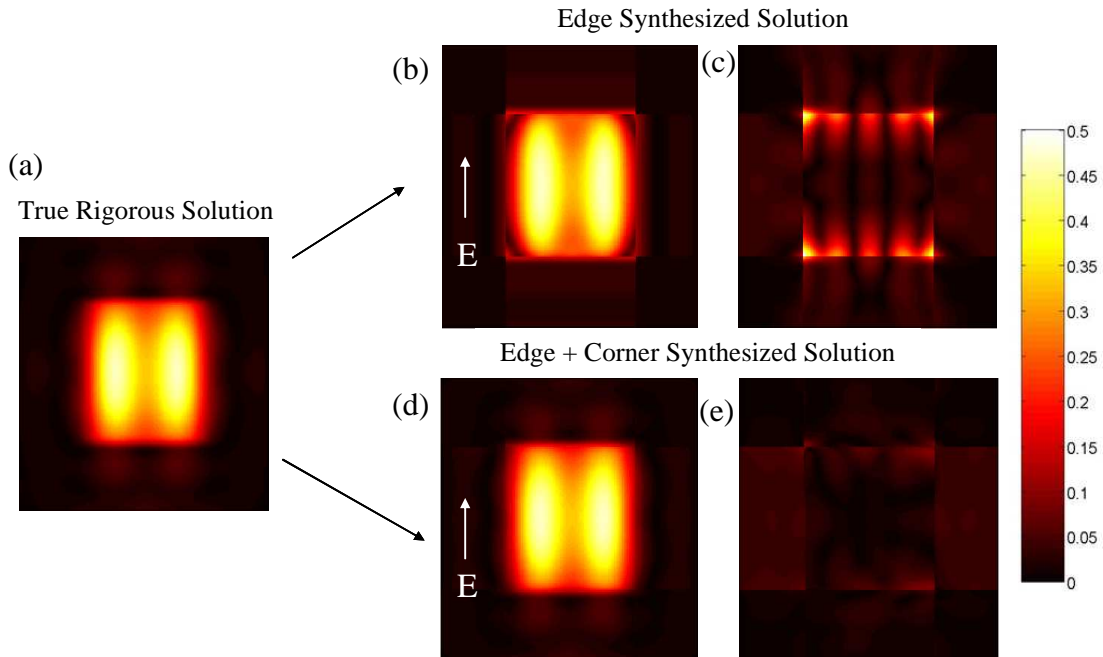
Figure 3.10. (a) True rigorous solution. (b) Edge-DDM solution. (c) Edge-DDM error compared to
rigorous simulation. (d) Corner-DDM solution. (e) Corner-DDM error compared to rigorous solution.

	NMSEs		
NA = 0.8 , σ = 0.7	Edges	Edges+CEF	Decrease
Projection NA (4X)	1.38E-4	1.36E-4	1.3%
Inspection NA (1X)	9.88E-4	5.99E-4	40%
Propagating Orders	0.0048	0.0026	46%
Inspection NA + σ	0.0139	0.0054	61%

Table 3.1. Shows the NMSE for edge-DDM and corner-DDM for various optical systems along with the corresponding percentage decrease in error from using corner-DDM.

called and inserted into the structure at the appropriate place. In this manner, an existing edge-DDM library can be augmented with corner information.

Figure 3.10 shows the synthesized fields from both edge-DDM and corner-DDM compared to the rigorous simulation for the same 400nm x 400nm contact as used to describe the accuracy of DDM in chapter 2. The errors in the diffracted spectrum are shown in Figure 3.11. The high frequency errors have been greatly reduced by using the CEF. In fact, the addition of the CEF has reduced the NMSE by 62%, for all orders involved with inspection simulations at $\sigma = 0.7$. Table 3.1 shows the reduction in NMSE for various systems when corner-DDM is applied instead of edge-DDM. The results show significant decreases in errors for the case of inspection. The total NMSE for the inspection case is about 0.5%, implying that corner-DDM would provide a good description of the scattered fields for die to database inspection.

Another interesting observation can be made by comparing the two error fields in Figure 3.11. The largest source of error in the diffracted spectrum comes from plane waves that are located on the very edge of the propagating waves boundary, specifically those waves propagating around 90º in the x-direction. The scattering in the x-direction comes from features in the object that are oriented in the y-direction and are exposed to the TE polarization. The bright spots in the error fields can then be attributed to highly
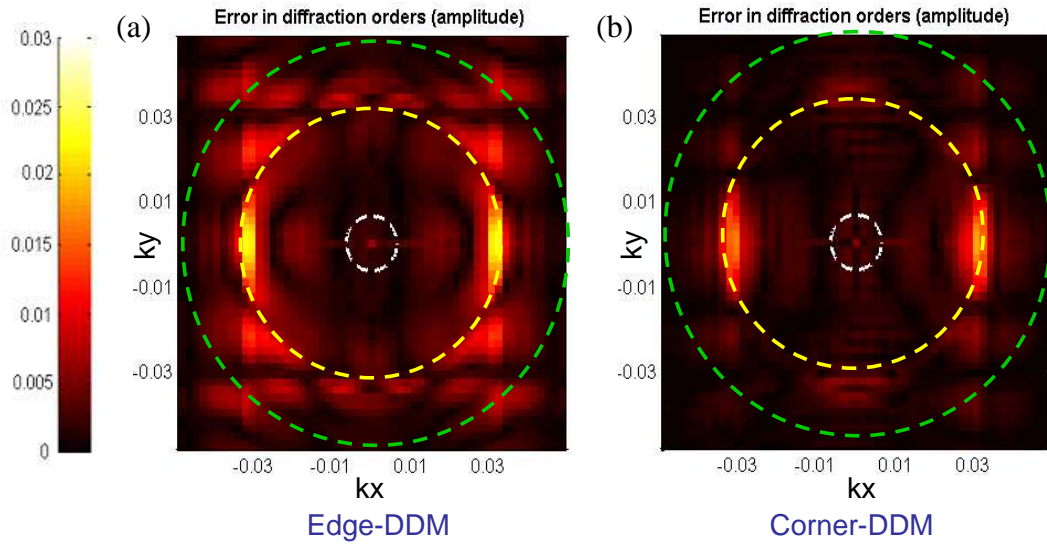
Figure 3.11. Three circles are placed on each plot. The small circle is NA = 0.8 for exposure tool, the medium circle is the propagating wave boundary, and inside the large circle represents all waves collected by an inspection tool with σ = 0.7 and NA = 0.8. (a) FFT of errors from Edge-DDM. (b) FFT of errors from Corner-DDM.

scattered TE waves. As was mentioned in section 3.1 of this chapter, the TE waves were found to limit the application of edge-DDM since their boundary conditions led to more scattering, and thus, greater edge to edge interactions. One final piece of information can be gathered by looking at the peak error ($E_{error} \sim 0.06$) in the diffracted spectrum of the same square contact in Chapter 2, and comparing it to the peak error ($E_{error} \sim 0.03$) in Figure 3.11 for the edge synthesized fields of the same contact. The peak error dropped by about a factor of 2, in the location of these highly scattered TE waves. The only change between the simulations is that the contact in Figure 3.11 was simulated with a larger domain, and was thus, more isolated than the contact in Chapter 2. Since the contact is physically the same contact for both simulations, the decrease in error can be associated with the greater isolation of the contact. This fact implies that a large portion of the measured error stems from the inability of the rigorous 3D simulation to isolate the

simulated structure as well as edge or corner-DDM, because of the periodic boundary conditions of most EMF solvers. The true NMSE values are likely to be significantly lower (better) than those observed here, if an isolated structure is desired.

3.4 Conclusions

The edge-DDM approximation was shown to be valid to at least 0.5% in NMSE for feature dimensions greater than 2λ when used to simulate printing. The "rigorous" simulation of large areas of a chip layout may therefore be performed very quickly with edge-DDM, without the computational expense of actually rigorously simulating the domain. The 2λ rule is valid for all types of edges present in an arbitrary layout, providing a good rule of thumb for edge-DDM applicability. The limits of edge-DDM are in fact lower than the 2λ rule would suggest, but pushing this limit to a smaller value will depend specifically on the types of edges present in a layout. Additionally, the TE polarization will limit the minimum dimension applicable for edge-DDM, but a heuristic fix might be applied that properly models the boundary interactions at small CDs to shrink the minimum dimension to $1 - 1.5\ \lambda$.

The defect projector method for assessing defect printability was introduced and shown to accurately predict the CD change of structures containing defects to within 30% of truly rigorous simulations (worst case), but is expected to work much better at higher NILS and line locations farther from the base. The defect projector can therefore be used as a method to rapidly sift non-critical defects from a host of possible locations, and allow truly rigorous simulations to be focused on only the critical defects.

The implementation of edge-DDM for inspection is complicated by the fact that high frequencies will always enter the imaging system at 1X and edge-DDM will always produce errors in the high frequency terms. The high frequency errors can be corrected by implementing a Corner Error Function (CEF) into the edge-DDM library, allowing all orders collected by an inspection system to have a total NMSE of 0.5% when simulated with corner-DDM. A DDM solution is therefore a likely candidate for building a database "on the fly" for die-to-database inspection. Finally, a significant portion of the calculated error in the NMSE was shown to stem from highly oblique TE waves that are a result of the inability of rigorous simulations to isolate the structure of interest. The NMSE estimates are therefore conservative in nature, and are likely significantly lower when synthesizing the fields of isolated structures.

4 Phase Defects

4.1 Real Defects

This Chapter explores simple physical models based on effective areas that can be used to help understand the observed differences from simple geometry based models. This difference from geometrical shape was observed by Adam, et al. [7] when he showed that phase defects do not behave electromagnetically as their physical phase height indicates, as expected from using an ideal mask model with scalar diffraction theory. A method for extracting the three algebraic model defect parameters (its area A, its amplitude M, and its phase φ_{defect}) from the focal behavior of isolated defects is demonstrated for ideal thin mask defects. This method is then applied to rigorously simulated defects to obtain model parameters for an electromagnetically equivalent thin mask defect.

4.1.1 Effective Brightness

The increased brightness (amplitude squared) of post defects and the corresponding decrease in brightness of void defects [7] can be understood through the refraction of light back into the glass, the same effect responsible for the intensity imbalance in phase shifting masks[65] . For a perfect, rectangular, full height post defect, the refraction of light into the post increases the brightness seen directly under the defect.

46

The increased brightness can be simply modeled through increasing the effective area of the defect by allowing light from a certain distance Δd away from each phase edge to be included in the defect. The resulting increased electric field and intensity can be modeled by:

$$E_{True\_post} = [\frac{A+dA}{A}]E_{Splat\_post}$$

$$I_{True\_post} = [\frac{A+dA}{A}]^2 I_{Splat\_post}$$

This simple model is plotted on top of Adam's data (at $\lambda = 248$nm) in Figure 4.1a for a Δd of 45nm, implying that the radius of influence surrounding a 180-degree phase edge is about 0.18 λ.

The decreased brightness of void defects may be modeled similarly. The electric field inside of the void is depleted some distance Δd away from the phase edges, resulting in a decreased area. The decreased electric field can be viewed as uniformly distributed across the void, such that its brightness can be modeled by:

$$E_{True\_void} = [\frac{A-dA}{A}]E_{Splat\_void}$$

$$I_{True\_void} = [\frac{A-dA}{A}]^2 I_{Splat\_post}$$

The model is plotted on top of Adam's data in Figure 4.1b for a Δd of 90nm. The larger Δd for the void is surprising and physically may be due to the reduced ability of the fields to respond to an edge in the air with n=1 or to the fact that internal reflection reduces the fraction of the captured energy released from the top of the defect.
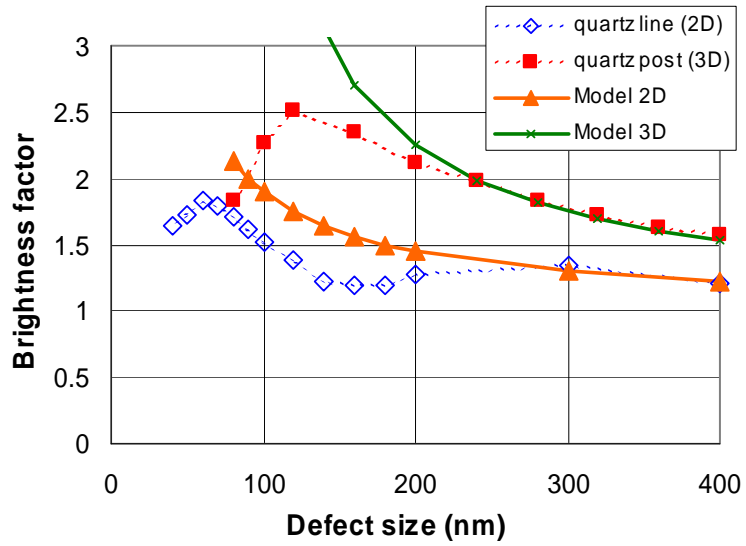
(a)
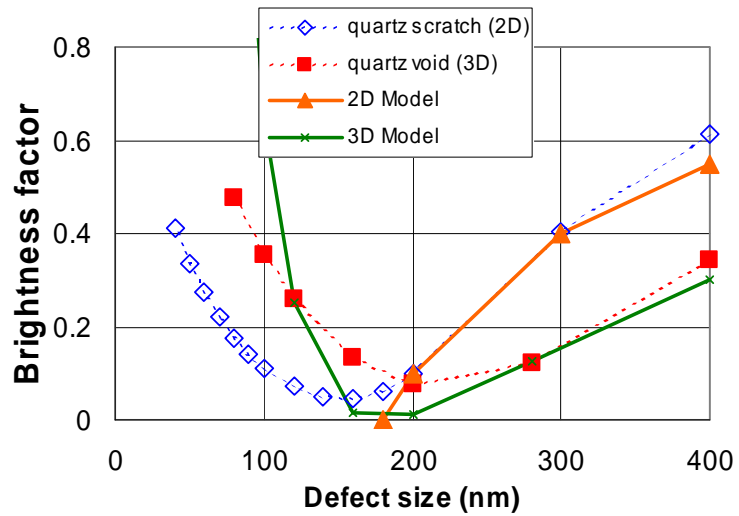
(b)

Figure 4.1. Simple area model for the near field brightness changes below "real" 180 degree defects, based on effective area changes due to refracted light a distance Δd away. (a) Post defect for $\Delta d=45$nm at $\lambda=193$nm. (b) Void defect of $\Delta d=90$nm at $\lambda=193$nm.

4.1.2 Effective Phase

Similar arguments based on the effective areas of defects can be applied to their phase as well. For post defects, the electric field absorbed from the surrounding air has an average propagation distance that shifts its phase relative to the vertically propagating light originally contained within the post. The refracted waves serve to dilute the phase of the original, vertical propagation of light. This effect can be modeled by:

$$\varphi_{True\_post} = [\frac{A}{A + dA}]\varphi_{Splat\_post}$$

Agreement with Adam's data can be seen in Figure 4.2a for both 2D and 3D posts with Δd = 45nm. This Δd value for effective phase is consistent with the value derived from the simple model for a post's brightness, providing validation that the simple area models are physically appropriate.

The extension to void defects is more difficult because light is much less likely to have vertical propagation within the void. Models based on effective areas can be used to successfully predict the void defect's phase; however they are more complicated with less physical intuition. Figure 4.2b shows fits of two such models to Adam's data for Δd = 90nm, given by:

$$2D : \varphi_{True\_void} = -[\frac{A - dA}{A}]\varphi_{Splat\_void} + 90$$

$$3D : \varphi_{True\_void} = \left([\frac{A - dA}{A}]\varphi_{Splat\_void} + 150\right)[\frac{A - dA}{A}] + 150$$

$$For : \varphi_{Splat\_void} = 180^0$$
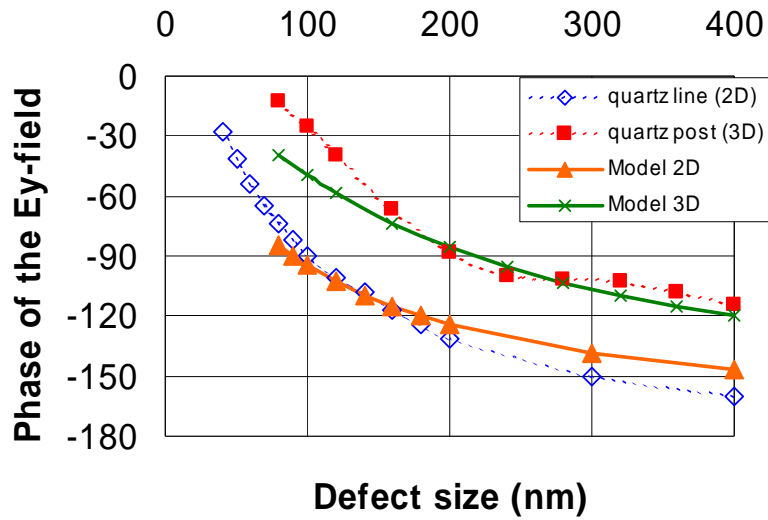
(a)
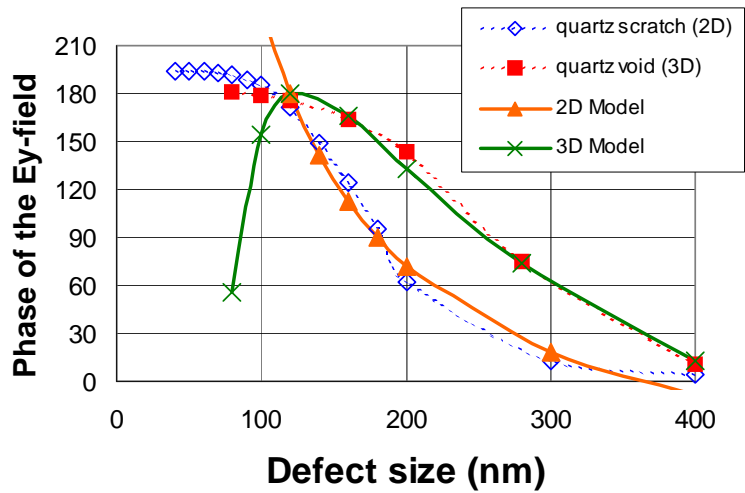
(b)

Figure 4.2. Simple area model for near field phase changes below "real" 180 degree defects, based on diluted vertical propagation within the defect from refracted light a distance Δd away. (a) Post defect for Δd=45nm at λ=193nm. (b) Void defect of Δd=90nm at λ=193nm.

4.2 Focus Behavior of Isolated Defect

An isolated defect in a clear field will produce a noticeable dip in the clear field that will vary with focus. This effect can be seen for an M=1, d=0.18λ/NA (1X), 120° phase defect for the images plotted in Figure 4.3. Notice the dip in the clear field is larger for an out of focus value. In focus, the magnitude of the dip in the clear field can be interpreted by the algebraic models as twice the electric field signal of an opaque defect multiplied by a constant defined by two of the model parameters (M and φ_{defect}), where E_f = 1 (clear field) and with $\mu_{eff} = 1$:

$$\Delta I = 2E_{opaque\_defect}[1 - M \cos(\varphi_{defect})] \qquad \text{(See top half of Equation 2.3)}$$

Dividing this signal by 2, gives the resulting modified electric field defined by:

.   Equation 4.1: $E_{mod} = E_{opaque\_defect}[1 - M \cos(\varphi_{defect})]$

120 Degree Phase Defect (.18L/NA x .18L/NA)
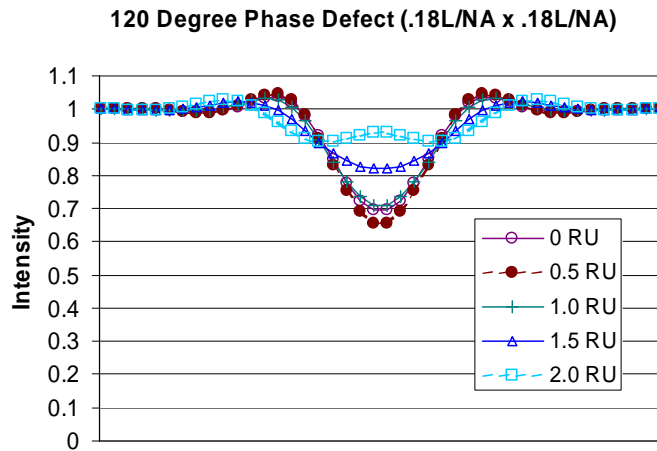
Figure 4.3. Images of dips in the clear field from an isolated, ideal (M=1), 120 degree defect of size d=.18μm, for various defocus values. Notice the dip intensity is larger for some out of focus values near 0.5 RU.
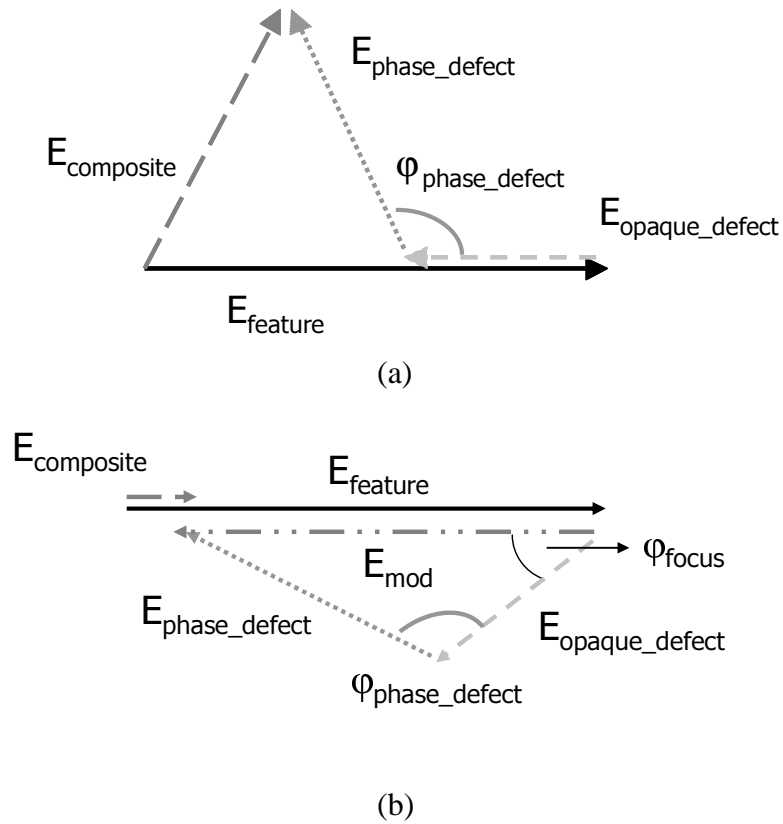
Figure 4.4. (a) Vector addition representation of algebraic model for phase defects. An opaque defect's E-field is first subtracted from the features E-field, the phase defect reinjects the E-field at a phase changed angle, resulting in the composite E-field. (b) The defect arm composed of both the opaque and phase defect vectors remains rigid through defocus. The arm rotates about the tip of the feature E-field, resulting in the maximum modified E-field when the tip of the defect arm lies on top of the feature E-field as shown.

The effect of defocus can be uncovered by the vector relationship shown in Figure 4.4a. The opaque defect vector and the phase defect vector are locked together at the defect's phase angle (φ_{defect}), creating an elbow on the combined defect arm. This arm rotates about the tip of the clear field vector (E_f) as defocus is applied. Notice that the maximum modified electric field (or largest dip in the clear field) occurs when the tip of the defect arm is rotated onto the clear field vector (E_f), shown by the dashed lines in Figure 4.4b. Notice also that the amount of rotation needed to create the maximum modified electric field will depend on the length of the phase defect vector relative to the opaque defect vector (ie, the parameter M). For M=1, the rotation angle of the defocus will only be ½ of

the value needed to produce a 180° phase change since this rotation affects both the opaque defect vector and phase defect vector. Thus, the defocus introduces another angle φ_{focus}, given by the angle of rotation for the defect arm that combines with the phase of the defect to give an intensity dip and modified electric field through focus, defined by:

Equation 4.2:
$$\Delta I = 2E_{mod}$$
$$E_{mod} = E_{opaque\_defect}[\cos(\varphi_{focus}) - M\cos(\varphi_{defect} + \varphi_{focus})]$$

The parameter φ_{focus} is just the additional phase variation from the two rays caused by moving through focus. The relative phase of the defect signal and the clear field signal with focus is due to wave propagation effects. For small phase defects ($\sim.2\ \lambda/NA$), the scattered light uniformly fills the pupil because of its broad spectral characteristics and because the pupil acts as a low pass filter. This light can be lumped into an average off-axis ray that propagates with an average phase through some portion of the pupil, as seen in Figure 4.5. Both the phase of the defect and the additional phase change from defocus, work in conjunction to produce a peak signal (minimum intensity) when a net phase
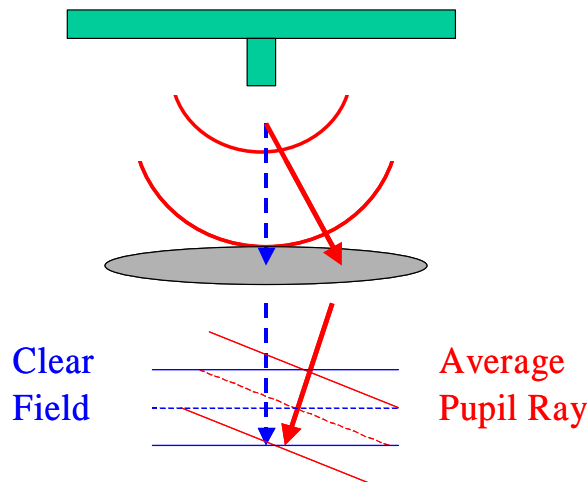
Figure 4.5. Phase defects scatter light everywhere in the pupil, and can be lumped into an average pupil ray that is phase delayed or advanced relative to the on axis clear field ray below the pupil. The phase fronts beneath the pupil show how defocus can increase or decrease the phase difference between the on axis clear field ray and the average pupil ray from the defect.

53

change occurs of 180° relative to the clear field. The interaction of the two rays is responsible for the peak signal shift through focus for different types of phase defects. For an ideal 180° phase defect, the peak of the signal occurs at 0 Rayleigh Units (RU) defocus, where a Rayleigh Unit is defined as:

Equation 4.3: $$1RU = \frac{\lambda}{2NA^2}$$

For defects with lower phases, larger defocus values must be used to add an appropriate phase change to the average ray to produce the 180° phase change. Thus, the peak signal occurs at the defocus value that changes the phase of the defect's average pupil ray to 180°.

4.3 Parameter Extraction from Image Behavior through Focus

Ideal, isolated phase defects may be imaged through focus from [-2,2] Rayleigh Units (RU) and the values of the dips can be used to extract the modified electric field values, defined by Equation 4.2. The modified electric fields can then be plotted through focus, as shown in Figure 4.6a. Note that the field can become negative at large values of defocus due to image reversal. Taking the largest modified electric field seen through focus and its two nearest neighbors, a parabola can be fit to the data. This parabola allows the true peak modified electric field to be estimated, and it's associated defocus value. If this process is done for various defect phases, the phase of each defect can be plotted vs. the defocus value for the peak signal location for each defect, as seen in Figure 4.6b. The

(a)

Phase= -134.67*Defocus + 180.68
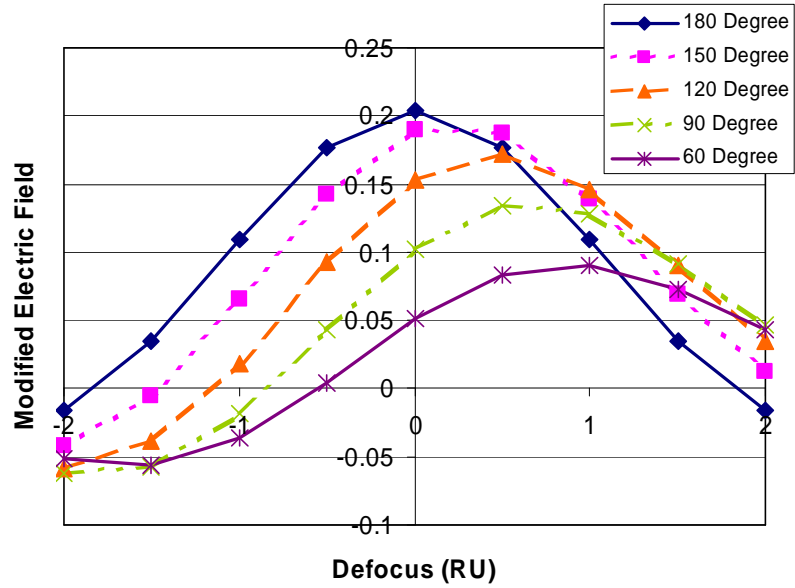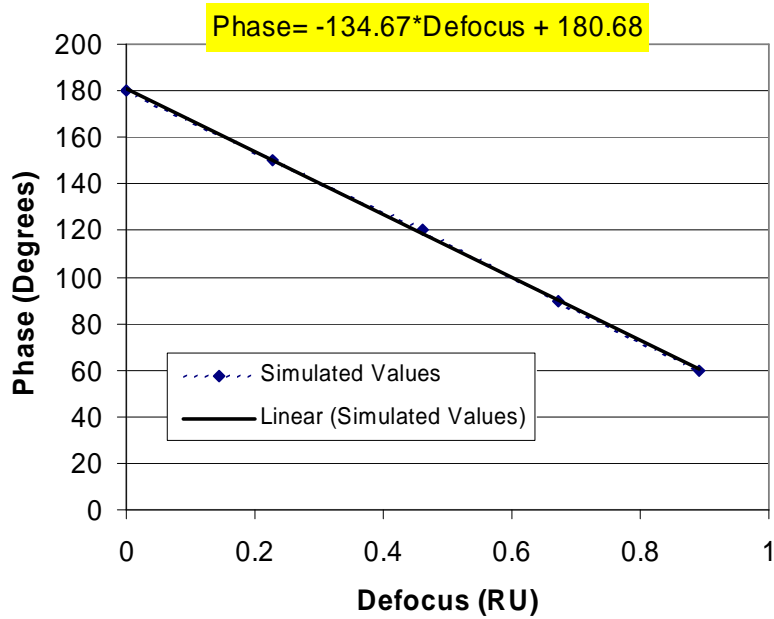
(b)

Figure 4.6. (a) Modified electric fields of images centered below the geometrical shadow of the phase defects, for various ideal (SPLAT) phase defects. The peak field is located out of focus for non 180 degree defects. (b) The phase of ideal (SPLAT) defects is plotted vs. estimated locations in defocus for the peak fields. The linear relationship allows defect phase identification when M=1.

relationship is linear, and a line can be fit to the data to produce:

Equation 4.4: $\qquad Defect\_Phase = -134.67\, Peak\_Defocus + 180.68$

Since this linear relationship was derived from ideal phase defects, M=1, it can only be used to predict the phase of M=1 defects. Alternate relationships may be derived from different M values, but are not necessary, as will be shown later. Now that the relationship is known, an unknown isolated defect's phase (assuming M=1) can be determined by simply imaging the defect through focus, fitting a parabola around the peak to obtain the defocus value where the peak occurs, and using the result to calculate the defect phase based on the known linear relationship.

For these ideal defects, M=1 is known, φ_{defect} has been extracted from the defect's focus behavior, and the defocus in RU has been related to the φ_{focus} angle via Equation 4.4. The last parameter that needs to be extracted is the defect's area (A). This last parameter can be extracted from the modified electric field at 0 defocus, which is given by Equation 4.1, since E_{opaque_defect} is proportional to its area (see Equation 2.1). Equation 4.1 can be rearranged to give:

Equation 4.5: $\qquad A = \dfrac{E_{mod}}{k[1 - M\cos(\varphi_{defect})]}$

Where k = 2.98 from [26] when σ = 0.3, and E_{mod}, M=1 and φ_{defect} are known.

4.4 Rigorous Defect's Parameter Extraction

The linear relationship established in the previous section works very well for predicting the phase of ideal (thin mask) defects. A natural question arises: Does this

process work with "real" defects? A nominally 180° phase post and 180° phase void were simulated rigorously with the electromagnetic solver TEMPEST [8] to ascertain their printability. The phase defects were isolated in a clear field glass mask, and illuminated at normal incidence with 193 nm wavelength light. Both defects were 180nm x 180nm in size (4X), corresponding to a size of .187 λ/NA (1X) for NA=0.8. The central intensity dips of the aerial image were monitored through [-2,2] RU of defocus and the modified electric fields are plotted in Figure 4.7 (solid lines).

The post and void peak signals are on opposite sides of defocus, implying that an unknown defect type may be classified based upon which defocus side the peak signal is located. Posts have maximum signals occurring farther from the pupil, while voids have maximum signals occurring closer to the pupil. For posts, the average pupil ray is delayed relative to the clear field, and so moving further from the pupil will allow the clear field to cycle even faster than the average pupil ray until the phase delay widens to 180° and the peak signal is reached. For voids, the average pupil ray is advanced relative to the clear field, and so moving closer to the pupil will allow the clear field to reverse cycle faster than the average pupil ray until the phase advance reaches 180° and the peak signal is reached. Figure 4.6 can be used to demonstrate this effect by adding the phase fronts to the plane waves and looking at the phase change along the pupil axis.

Fitting parabolas to the peaks of the data in Figure 4.7, defocus values of -0.497 RU and 0.444 RU are obtained as the location of the peak signal for the post and void, respectively. Using the linear relationship in Equation 4.4, the effective phases for the post and void are -113° and 121°, respectively. Despite the large deviation from their physical phase heights of 180°, the deviations are expected for these "real" defects, as
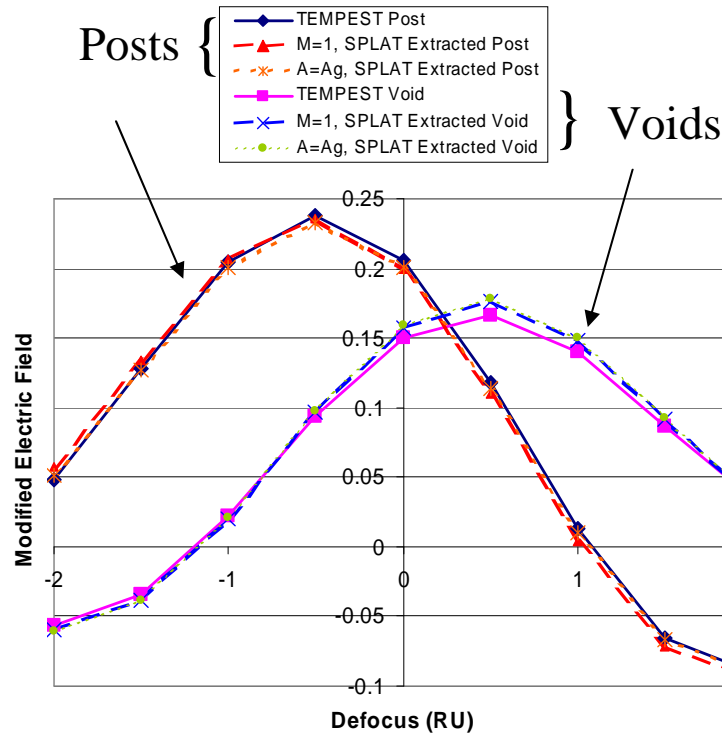
Figure 4.7. Modified electric fields of images centered below the geometrical shadow of the phase defect. Rigorous simulations from TEMPEST of a post and void are plotted along with the SPLAT simulations for the assumed M=1 extracted parameters, and assumed A=Ag extracted parameters.

discussed in previously, however, the extracted effective phases do not agree with the near field average phases seen by Adam, despite scaling the defect sizes appropriately from their 193nm values to 248 nm values. This inconsistency can be explained by understanding that the linear relationship in Equation 4.4, which implicitly assumes M=1, is NOT the case for "real" defects due to their increased effective brightness. Why then, has it been assumed M=1? The assumption of M=1 makes the parameter extraction easier. Again looking at Figure 4.4a and 4.4b, the only physically real parameter that must be rigidly enforced is the length of the combination of the two defect vectors. It is this combined vector that rotates through defocus. Regardless of what two defect vectors form the combined vector, as long as its length is the same, it will behave in exactly the

same manner. This implies that a defect is not unique in its behavior, and while "real"

defects have M values greater or less than 1, equivalent defects with ideal transmissions

(M=1) and different areas (A) and phases (φ_{defect}) can be found that behave in exactly the

same way through focus. In this manner, an equivalent defect may be found that mimics

the behavior of the "real" defect, despite being a physically wrong description of the near

field electromagnetics. Alternatively, A=A_g (geometrical defect area) may be assumed

and the values of M and φ_{defect} can be adjusted to obtain the same vector, however,

parameter extraction is much more difficult in this case, and requires knowledge of the

defect size beforehand.

The second parameter (A) can be extracted as demonstrated in the previous

section using Equation 4.5. Plugging in the known values of E_{mod}, k, M=1, and φ_{defect}, the

area is found to be A=0.223μm and A=0.18μm for the post and void, respectively. Using

the extracted parameters of A and φ_{defect}, combined with an assumed M=1, ideal SPLAT

defects were run to show how well the parameters match the TEMPEST data. The dashed

lines in Figure 4.7 represent ideal defects simulated with SPLAT using the extracted

parameters from the TEMPEST data. Also plotted in Figure 7 (dotted lines) are ideal

SPLAT defects with an assumed A=A_g (same geometrical defect size), and M= 1.7, 1.05

(post, void), with φ_{defect} = -130°, 123° (post, void). Notice that all curves are nearly

identical in their behavior, showing that defects are not unique in their behavior.

4.5 Conclusions

Simple physical models based on effective areas have been shown to provide a fairly accurate description of a "real" defect's brightness and phase for both post and void defects. Posts were shown to electromagnetically behave about $.18\lambda$ larger on a side than their physical dimensions indicate, while voids were shown to behave about 0.36λ smaller on a side. Void defect behaviors were more difficult to capture with simple area models, possibly because the light is much less likely to have vertical propagation within the void.

Algebraic thin-mask models for the printability of phase defects have been extended to the case of post and void phase defects that electromagnetically behave differently than their physical height. Their average magnitude (M) and phase (φ_{defect}) in addition to their defect area (A) is shown to be adequate for predicting the intensity dip for isolated defects and by implication likely all that is necessary for modeling line width change. By assuming M=1, the other two parameters (φ_{defect} and A) may be successfully extracted from inspection data or rigorous simulations. Post and void defects can be differentiated based upon where their peak signal occurs through focus, further from the pupil for posts and closer to the pupil for voids. When the two parameters φ_{defect} and A of a "real" defect are known, the defect's behavior through focus from rigorous simulations can be mimicked quite accurately with SPLAT simulations using the two extracted parameters. The algebraic model thus serves as a multidirectional link between geometries, electromagnetic scattering analyses, lithographic performance, and (by extension) inspection.

5 New Method for Simulating EUV Buried Defects

This Chapter will systematically examine the process of scattering from EUV mask blanks. The challenge of simulating such scattering is the generation of new waves propagating inside the multilayer which stem from three physical effects: forward scattering, backward scattering, and specular reflections. Specific problem characteristics of EUVL are identified that yield new approximations for each of the three physical effects which can be leveraged together to over come the challenges of simulating EUV mask blanks. These characteristics will allow the development of a new method for calculating the reflection from EUV mask blanks. The new method is based on a series of approximations which evolved from physical insight of the scattering process and its accuracy has been verified.

The EUV scattering problem can be decomposed into three stages: a push inward, a reflection from a non-planar surface, and a push outward. In particular, suitable approximations need to be examined in the push inward to deliver the electromagnetic energy into the multilayer. Then the second stage can be performed by calculating the reflection from each individual surface. The final stage, the outward push, will propagate the reflected electromagnetic energy out of the multilayer, resulting in the finalized reflected field. Both a geometrical optics approach (ray tracing) and a Fourier optics approach (spectrum) are proposed to solve the individual stages of the scattering

problem. The multilayer itself will be broken into individual layers where the scattering is evaluated in a manner that anticipates resonant effects from being within the mirror layers. A final methodology is proposed for calculating the reflected fields, generating a hybrid method that combines geometrical and Fourier optics.

5.1 EUV Simulation Challenges

The greatest challenge for simulating EUV multilayers is the generation of new waves within the resonant structure. The incident wave entering the multilayer will begin to transmit and reflect at every layer in the structure, creating new daughter waves that will again re-interact with the multilayer and create further daughter waves. There are three physical mechanisms by which new waves are created inside the multilayer: forward scatter, backward scatter, and specular reflections.

Forward scatter is the generation of non-specular, forward propagating waves which stem from the diffraction that occurs from transmitting through an interface. Backward scatter is the generation of non-specular, backward propagating waves which stem from the diffraction that occurs from reflecting at an interface. These effects can be understood from Figure 5.1, where a single plane wave is incident on an interface, and a
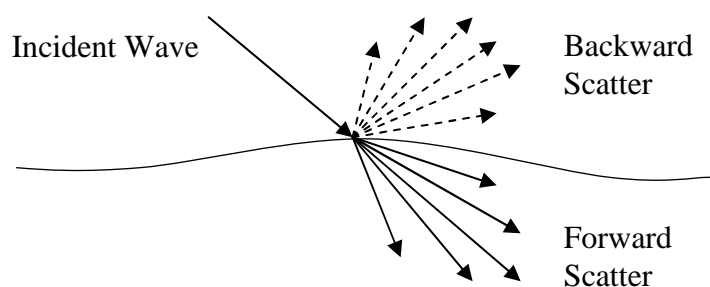
Figure 5.1. Visual depiction of backward and forward scattering at a single layer interface.
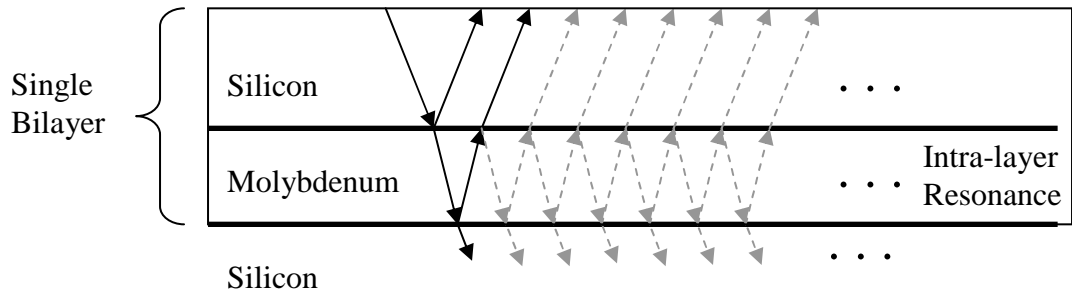
Figure 5.2. Wave picture of specular reflection and transmission from a single bilayer showing the intra-bilayer resonance.

large number of waves leave the interface in the forward direction and backward direction. Each one of these newly generated waves will also need to be tracked through the structure to properly compute the reflection from the multilayer.

Specular reflections are similar to backward scatter except only the specular direction is reflected. Inside of a multilayer, a wave can specularly reflect from every interface an infinite number of times, creating many new waves to track. These reflections are responsible for the resonance of the multilayer structure, and can be better understood by categorizing the specular reflections as either intra-bilayer or inter-bilayer resonance. Figure 5.2 shows an example of reflecting from a single bilayer, and the intra-bilayer specular reflections can be immediately understood to stem from reflections within the same bilayer. Figure 5.3 shows an example of reflecting from a single bilayer
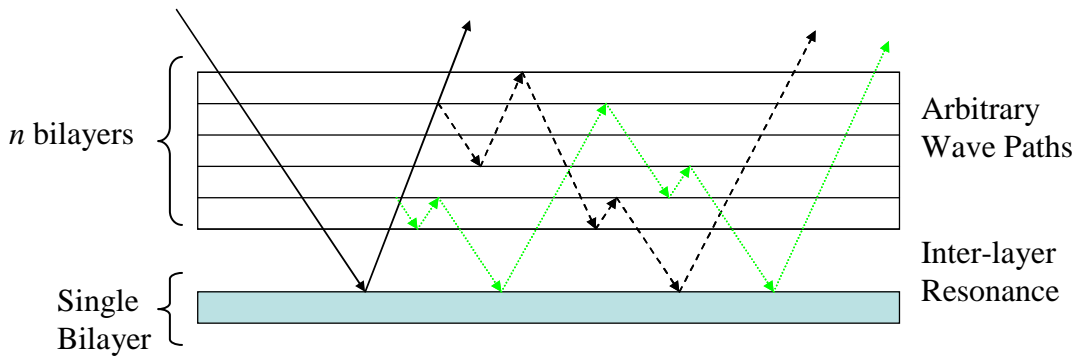
Figure 5.3. Depiction of inter-bilayer resonance as any arbitrary path a wave can make between the initial reflection off the single bilayer and exiting the structure at the top.

with n bilayers stacked on top of it. The Figure shows two arbitrary wave paths that capture the effects of inter-bilayer resonance which stems from interactions between bilayers in the multilayer. Both types of specular reflections will need to be computed to accurately predict the reflectivity of a multilayer stack.

When building a fast simulation method that explicitly tracks waves that bounce and diffract inside a resonant structure, it is essential to find ways to limit the generation of new waves inside the structure. Diffraction can produce R new waves per incident wave upon reflection (back scatter) and T new waves per incident wave upon transmission (forward scatter). Calculating just the primary reflection from a single layer with N layers on top of it would require summing:

$$r_{one\_layer} = \sum_{r=1}^{T^{2N}R} E_r$$

Here, a total of $T^{2N}R$ plane waves are generated outside of the mask blank due to reflection from a single layer with N layers stacked on top of it. One can easily see that the bulk of these plane waves are actually generated by the forward diffraction T from propagating a wave down to the layer under observation (T^N) and back up through the mask blank (T^N). It is therefore useful to understand the forward diffraction and see what approximations can be made to minimize its effects. Many, many more waves are generated if one considers multiple back scatter events that bounce around the multilayer. Each reflection would result in an additional R waves that could bounce an infinite number of times, created R new waves with every bounce. Explicitly calculating only those waves that bounce k times or less would require summing at least:

Equation 5.1:
$$r_{one\_layer} = \sum_{r=1}^{N^{(j-1)}T^{2(k(N-2)+2)}R^k} E_r$$

64

Here the number of waves has grown to $N^{(j-1)}T^{2(k(N-2)+2)}R^k$ where k is the number of applications of back scatter and j is the number of specular bounces (generally $k=j$). It will therefore be necessary to cap the number of back scatter events (k) as well as the number of bounces from specular reflections (j).

The creation of new waves within the multilayer from either diffractive effects or multiple specular reflections will ultimately limit the ability of a new method to achieve both accuracy and speed in its calculation. However, even from single back scatter event ($k=1$) that neglects multiple specular reflections inside the multilayer ($j=1$), the creation of new waves from diffractive effects will be staggering. Using Equation 5.1 (with $j=1$, $k=1$), if each individual layer produced 10 new orders upon reflection (R=10) and 10 new orders upon transmission (T=10), the final layer in a 40 bilayer stack (N=79) would have to add the effects of 10^{159} waves to compute the reflection from its surface!

Clearly, approximations that limit the generation of new waves will be needed since any method that tracks resonant energy movement around the structure is doomed to be too slow because of the large numbers of multiply scattered waves from daughters of daughters, etc.; however, the effect of every one of these generations of rays must be accounted for if a method is to produce a correct final reflection. Simplifying assumptions that limit the forward scattering, backward scattering, and specular reflections will need to be introduced to allow the accurate computation of the reflection with only a finite number of waves.

5.2 Problem Characteristics

There are 3 specific problem characteristics of buried defects inside of EUVL multilayers that will enable approximations to be made that limit the generation of new waves inside the multilayer, and thus give guidance towards the development of a fast and accurate method for simulation. First, the refractive indices for molybdenum and silicon are both very close to that of air (n=1). This "optical homogeneity" implies that existing electromagnetic waves propagating inside the multilayer will continue to travel in that same general direction without much deviation. The optical homogeneity dictates that the specular reflection coefficient magnitude of each individual layer is about $|\rho| \sim$ 0.04, which implies that multiple reflections inside of the multilayer will be very small unless they coherently combine over several layer pairs. As such, the forward and backward scattering inside the multilayer may be able to be simplified or decoupled.

Secondly, the layers within the mask blank have the property of "optical smoothness". Unlike DUV transmissive masks, there are no vertical boundaries or corners to provide high angle scattering or to introduce additional coupling between the electric and magnetic fields. Thus, the lateral components in the diffracted spectrum are generated gradually. As such, the reflection analysis from each individual layer can be approximated very well via a thin mask transmission function, exactly akin to the SSA approach. Even more importantly, the smoothness also makes both surfaces of a given material region very nearly parallel to each other, and thus the non-specular forward scattering is extremely low ($|E| \sim 0.0004$) in the forward diffracted spectrum. The optical

smoothness also implies that high frequency techniques, like geometrical optics, might be used to aid fast simulations.

Thirdly, the analysis of reflection from a multilayer is aided by the EUVL optical system itself, which has a small numerical aperture (NA) of about NA = 0.3 and a 4X demagnification. This limited angular collection implies that only a small angular cone of reflected waves will enter into the optical system, and that only the Through The Lens (TTL) spectrum of a reflection will need to be calculated accurately. For a proposed EUVL system at 4X with $\sigma = 0.3$ and NA = 0.3, only diffracted waves propagating within a small angle of about $|\theta| \leq 5.6$ degrees need to be accurately calculated. These three problem characteristics will help guide decisions on the development of a fast and accurate methodology for simulating buried defects.

5.3 Key Approximations

When developing a new methodology for simulating EUV buried defects, the three physical mechanisms mentioned in Section 5.1 (forward scatter, backward scatter, and specular reflections) can be restricted by introducing three key approximations that are derived from the three problem characteristics of Section 5.2 (optical homogeneity, optical smoothness, and limited angular collection of the EUV scattering problem). Each approximation will address one physical mechanism and will place limits on the number of waves that can be generated inside the multilayer, allowing a finite set of waves to predict the full reflection. The three key approximations are listed below, along with their effects on Equation 5.1 for limiting the number of waves needed to be computed:

1) The forward scatter of the incident plane wave is negligible (T=1)

2) The specular reflections from intra- and inter-bilayer resonance can be anticipated with analytic approximations and need not be explicitly tracked in the multilayer. (Specular reflections summed analytically, j=1)

3) Multiple back scatter events between defective layers is negligible (k=1)

In making studies of the multilayer structure, it was found to be advantageous to understand the multilayer structure in terms of scattering from a complete bilayer instead of from individual layer interfaces. For a transmitted wave, each perturbed layer interface acts as a lensing agent which creates forward scatter; however, the second interface of the bilayer acts as a de-lensing agent which efficiently undoes the effects of the first layer interface. The net forward scattering effect of transmitting through a full bilayer is thus much smaller than simply transmitting through a single layer interface. This physical behavior will prove crucial to building a fast and accurate method for simulation since it allows a tremendous simplification of the forward diffractive scattering that occurs inside of the multilayer. Neglecting forward scattering is extremely important to the new method and is the first key approximation that will be more rigorously justified in Section 5.5.

This physical behavior of a full bilayer provides an efficient way to limit the generation of new waves inside the multilayer while at the same time providing for the effects of the coherent addition of scattering contributions. This can be implemented by breaking the infinite set of waves into two categories (primary waves and resonant

waves), allowing a Primary Wave Approximation (PWA) to be invoked which permits only primary waves to be tracked through the multilayer stack. Primary waves are waves that have been reflected only 1 time or less, while resonant waves are multiply bounced waves (MBWs) that stem from multiple specular reflections within the multilayer. Their multiple reflections must be added to obtain accurate reflection calculations and are critical to capturing the resonance of the bilayer. The resonant waves come from two sources: intra-bilayer and inter-bilayer. Intra-bilayer resonance stems from the two surfaces of the same molybdenum layer (Figure 5.2), while inter-layer resonance stems from the interaction of multiple molybdenum layers (Figure 5.3). Under the assumption of parallel planar surfaces for each layer or stack, both types of resonance effects can be analytically summed and corrected within the program. This summation will be shown in detail in Sections 5.7 and 5.8 and allows the second key approximation to be implemented within the code. In this manner, the resonance is anticipated and corrected by analytic sums of defect-free mirrors. The PWA also allows the third key approximation to be efficiently implemented since it neglects multiple back scatter events. The reflection coefficient of a first order back scatter event from an individual layer is about $|\rho| \sim 0.005$, and so multiple back scatter events will quickly die out. More detailed justifications for ignoring multiple back scatter events will be shown in Section 5.7.

The three key approximations dramatically reduce the number of waves that need to be explicitly tracked within the multilayer. Specifically, one can easily show for a single layer with N layers on top, that their application allows the nightmarish scenario from Equation 5.1, where $N^{(j-1)}T^{2(k(N-2)+2)}R^k$ waves needed to be summed, to be reduced to

only R wave reflections from the last layer. Since there are then 80 layers in the full stack (40 bilayers), the final number of reflected waves that need to be tracked for the full multilayer would be a very manageable 80R waves.

5.4 Methodology Roadmap

Before a detailed justification for the three key approximations is demonstrated, the general approach for how the new simulation methodology deals with a resonant multilayer structure will be outlined. The strategy for the push inward (stage 1) will be to take an electromagnetic wave incident on the multilayer and discretize the wave front into a set of rays that can be traced into the structure. Each ray will be tracked as it propagates through the structure and deposits its energy on each interface, creating new reflections. These newly generated reflected rays will be left at their original locations and will be used to calculate the reflection from a non-planar surface (stage 2). Figure 5.4
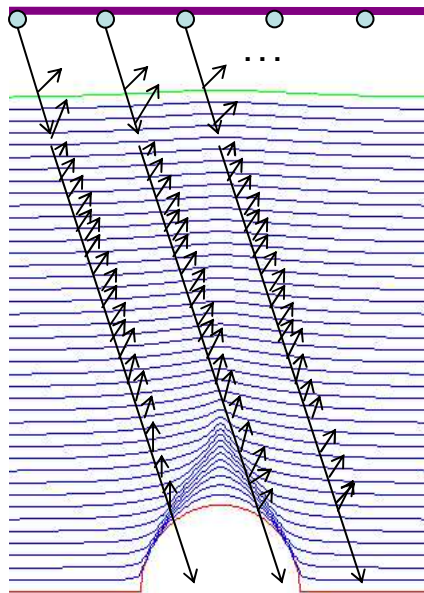
Figure 5.4. Schematic of the generation of reflected rays during the inward push using ray tracing.

shows a representative picture of how the incident rays will move into the structure, generating reflections at each interface. The first key approximation allows a single ray to be traced downward into the stack without generating additional forward propagating rays at new angles. The push inward will transmit the incident energy into the multilayer and both intra-bilayer resonance as well as inter-bilayer resonance will have to be corrected based on the incident angle for all the traced rays. These corrections can be applied by multiplying the traced rays by the analytic sums discussed from the second key approximation. The PWA generates one reflection for every layer interface for every ray.

For the reflection from a non-planar surface, all the ray reflections at a single interface can be linked together to form the spatial electric field strung across the interface. These rays must be moved back to a regular x and y grid to undo the subtle effects of lateral spreading and wiggling upon transmission into the multilayer. This movement is facilitated by a linear interpolation at regular grid points for the electric field value between rays. After the reordering, the rays are still sitting at the layer interface which contains vertical displacements from the non-planar nature of the interface. These rays must then be flattened onto a single plane by doubling the phase differential between rays in the middle and those on the end to account for the round-trip propagation. This flattening is similar to the flattening performed by the SSA. Thus, the reflection from the non-planar surface is automatically calculated by the ray tracing, once the rays are reordered and flattened.

Ray tracing cannot effectively propagate the reflected fields out of the multilayer since the rays begin to cross paths, creating shadow boundaries and ray caustics, as

described later in Section 5.8.3. However, a spectrum approach can now be used for the third stage, the outward push, where the reflected fields at each interface are propagated out of the multilayer. The flattened reflected fields can be Fourier transformed to break the electric fields into a set of newly propagating plane waves of many different angles. The reflections from the molybdenum to silicon interfaces are propagated up one layer so they sit outside of their source bilayer and have the intra-bilayer ACR applied to ensure the source bilayer resonance is counted. The PWA also allows the multilayer structure to be compacted into an ideal multilayer structure which is no longer defective. This compaction stems from the third key approximation where the back scatter from each layer cannot create another back scatter event. So, the reflected waves can only interact specularly with the multilayer, allowing the structure to be compacted. These waves can then be propagated out of the multilayer during the push outward. However, these reflected waves are sitting inside of a resonator and its resonance will have to be corrected in an angular dependent manner to limit the number of specular reflections. A dual mirror structure will be introduced which only requires a single inter-bilayer resonance correction to be applied during the push outward for all the plane waves

Problem Segment	Approach Used
Push Inward	Ray Tracing or Spectrum
Reflection from Non-Planar Surface	Spectrum
Push Outward	Spectrum

Table 5.1. Summary of final approaches used for each problem segment of EUV scattering.

created inside the multilayer. Once outside the multilayer, the spectrums of each layer are added together and inverse Fourier transformed to obtain the total reflected field.

Thus, a hybrid method is proposed for performing fast calculations of reflection from an EUV mask blank, which combines both geometrical and Fourier optics. The final proposed method can be summarized in Table 5.1 and a flow chart can be seen in Figure 5.5. While in principle, the spectrum approach could be used for all segments of the scattering problem, ray tracing is proposed to handle the propagation of energy into the multilayer. The tracing of the individual rays will save some of the small phase information obtained from actually tracing the rays through the defective structure, while the spectrum approach would deposit the energy based on a defect free structure. Chapter

Push Inward

```
                    ┌─────────────┐          ┌──────────────────┐
   ┌───────────┐    │ Ray Trace   │────────▶ │ Correct Intra- and Inter-│
   │Input File │───▶│ Primary Waves│         │ Bilayer Resonance │
   └───────────┘    └─────────────┘          └──────────────────┘
```

Reflection from non-planar Surface

```
   ┌──────────┐    ┌───────────────┐    ┌──────────────┐
   │ Fourier  │◀───│ Flatten Fields │◀───│ Reorder Rays │
   │Transform │    │ at each Layer  │    │ to Structured│
   │ Fields   │    └───────────────┘    │ X and Y Grid │
   └──────────┘                          └──────────────┘
```

```
   ┌────────────────┐    ┌──────────┐    ┌──────────┐
   │Propagate Plane │    │  Add     │    │ Inverse  │
   │Waves Correcting│───▶│ Spectrums│───▶│ Fourier  │
   │for Inter-Bilayer│   └──────────┘    │ Transform│
   │Resonance       │                    └──────────┘
   └────────────────┘
```

Push Outward

(Near Fields)
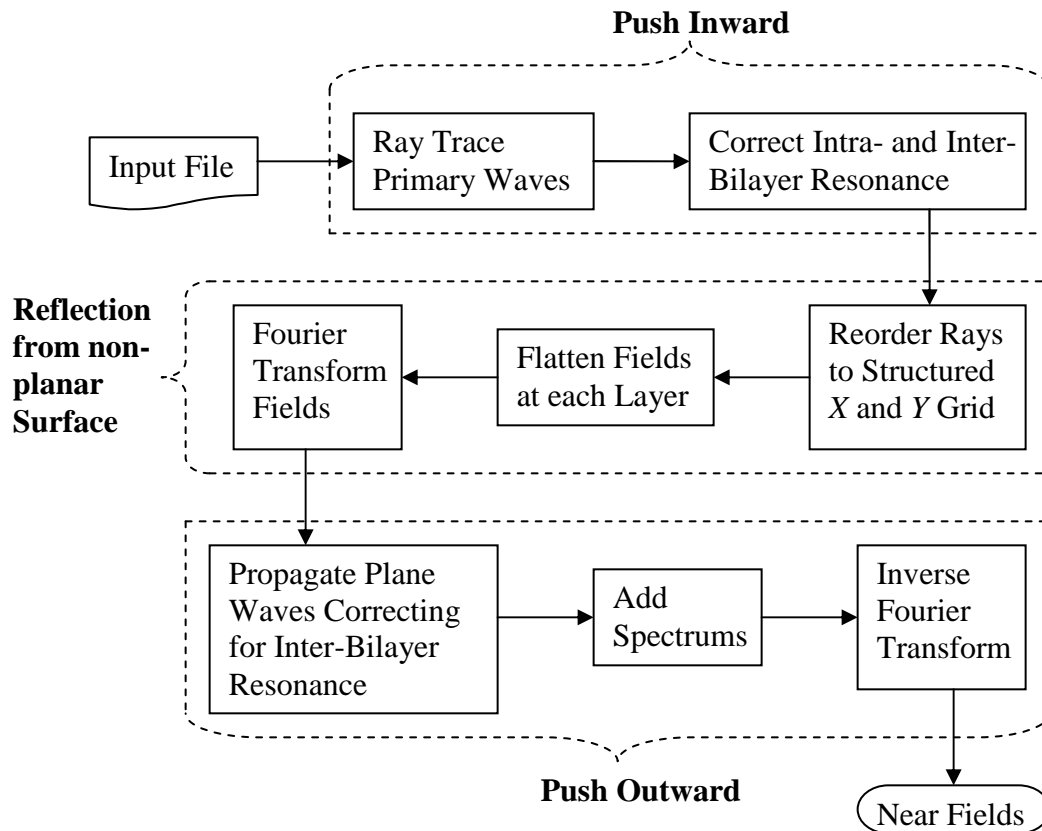
Figure 5.5. Flow chart of the new simulation methodology.

6

will show that each method can be used fairly generally, however, for certain buried

defect geometries it will be more beneficial to use one over the other. The final method is

a three stage process:

For each layer 1:N,

1) Ray trace the incident energy into the multilayer stack, correcting for resonant

   transmissions using an analytic model

2) Calculate the reflection from the nth layer and flatten the source by doubling the

   phase differential (exactly akin to the SSA method)

3) Propagate the spectrum out of the compacted multilayer using a dual mirror

   structure to correct for a single inter-bilayer resonance (FFT, propagate, IFFT)

Finally, each layer reflection can then be added together to produce a total reflection for

the entire multilayer stack.

5.5 Justification for Neglecting Forward Diffraction

From the analysis in Section 5.1, an impossible number of waves would need to

be calculated to properly compute the reflection from an EUV mask blank. Of the three

key assumptions, neglecting the forward diffraction is the most critical factor in reducing

the number of waves that need to be computed. This one effect will scale the number of

waves needed to be tracked for a single layer by $T^{2(k(N-2)+2)}$. The following analysis will

show that the forward diffraction can be neglected (T=1) because of the nature of the

bilayer as a unit.

For an incident plane wave, diffraction will begin to occur when the wave front experiences inhomogeneous local phase distortions from the defective layers. Essentially, portions of the incident wave front will be sped up, or slowed down relative to other sections of the wave front. The magnitude and frequency of these distortions will directly impact the amount of diffraction observed. The optical homogeneity and optical smoothness of EUV mask blanks dictate that the change in the forward scattered fields and angular spreading will be small, since the magnitude and frequency of these phase distortions will be low.

The optical smoothness of each bilayer prevents any individual section of the wave front from becoming sharply different from the fields surrounding it, and therefore the phase of the forward scattered field will vary smoothly and over long sections of the wave front. So the frequency of these phase distortions will be very low, resulting in low forward diffraction. The optical homogeneity of EUV mask blanks ensures the magnitude of any phase distortions will also be small. A phase distortion's magnitude is driven by the difference in the refractive indices seen at an interface, and the optical homogeneity of EUV masks guarantees that any section of the wave front will never see a large change in refractive index. Therefore, since both the magnitude and frequency of any potential phase distortions are expected to be small, the forward diffraction of an incident wave will also be small.

Despite each individual layer having a small forward diffraction, the small forward diffraction will be amplified as it propagates down through the 20λ thick mask blank and encounters about 80 other interfaces along the way. An extremely important addition to the above analysis is the effect of the bilayer as unit, which will make the

75

(a) Back Scatter:

	0th	$N \neq 0$
Top	0.04	0.0025
Bottom	0.04	0.0025
Top + Bottom	0.073	0.005

(b) Forward Scatter:

	0th	$N \neq 0$
Top	1.03	0.003
Bottom	0.96	0.003
Top + Bottom	0.98	0.0004

(c)

Individual Back Scattering Adds

Single Bilayer

Top

Bottom

Individual Forward Scattering Subtracts
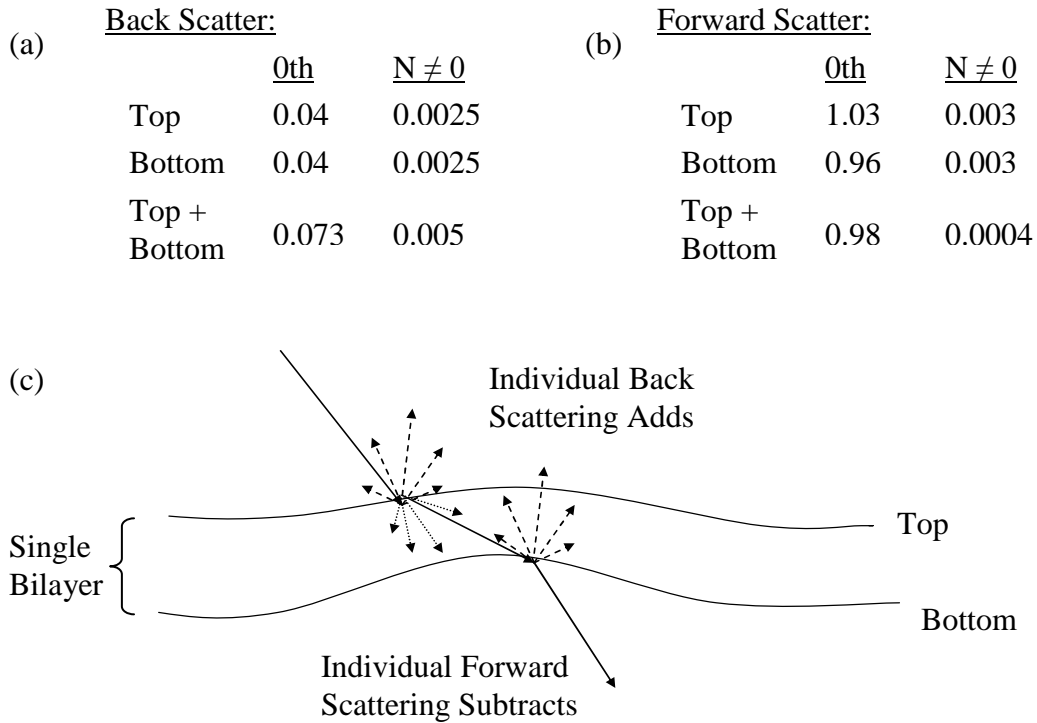
Figure 5.6. Data for a defective bilayer that has a 3nm high, 30nm FWHM Gaussian shape. The refractive indices are n_{si}= 0. 999942-j*0.00182099 and n_{mo}=0 .922769-j*0.00621555, with λ=13.4nm. (a) Approximate back scatter values for the 0th and off axis diffracted orders from both individual layers, as well as their combined effect. (b) Approximate forward scatter values for the 0th and off axis diffracted orders from both individual layers, as well as their combined effect. (c) Schematic diagram of the individual scattering events and how their combinations add in the back scatter, but subtract in the forward scatter.

forward diffraction minimal, and hence negligible. The first layer of the bilayer acts as a lensing agent to create a small forward diffraction effect on the transmitted wave, however, the second interface in the bilayer acts a de-lensing agent which undoes nearly all of the small effect from the first interface. Since the second interface acts as a correction to the small error made from the first interface, the total transmission through the full bilayer will have negligible forward diffraction. This effect is numerically shown and schematically drawn in Figure 5.6. The numerical results come from the FDTD simulation of a 3nm high, 30nm FWHM Gaussian shaped bilayer which is typical of an upper layer from a printable defect coated with the smoothing process. Notice that the

back scattering and forward scattering events are about the same order of magnitude

(0.003) when taken individually from a single layer. However, when combined into a full

bilayer, the back scattering events add together to produce a larger back scattering event,

while the forward scattering events largely cancel and are a full order of magnitude

smaller.

An error bound for this approximation can be estimated using the data in Figure

5.6. The associated error from a single bilayer is $|e| \sim 0.0004$, but this error has to reflect

from the multilayer and transmit through the multilayer depending on the depth at which

it was generated. Adding the error $|e|$ for the full multilayer would lead to a sum:

$$| e_{forward\_diffraction} | \sim 0.0004 E_{inc} [r_{39}t_1 + t_1 r_{38} t_2 + t_2 r_{37} t_3 + ...] = 0.0004 E_{inc} \sum_{m=1}^{39} t_{m-1} r_{40-m} t_m$$

Here t_m and r_m mean the transmission or reflection through m bilayers. Explicitly

calculating this sum results in a value of about 10, showing that a first order estimate of

the total error associated with neglecting forward diffraction is $|e_{forward\_diffraction}| \sim 0.004$,

which is quite small.

Minimal forward scattering can further be shown by the data from the FDTD

simulation for the 3nm high, 30nm wide Gaussian bilayer. The forward scattering was

compared to the backward scattering from reflections, and their angular spectrums can be

shown in Figure 5.7a on a log scale. The backward scattering (reflection) is already

small, since the first diffracted order is less than 7% the magnitude of the specular order,

and a full 95% of the energy is contained within an angular cone of $\pm 5.2°$. It is also

obvious that that the forward scattered field is significantly smaller than the backward

scattered field, by as much as 10X for small angles. In fact, 99.9997% of the energy in

the forward scattered direction is at the same incident angle, confirming that minimal
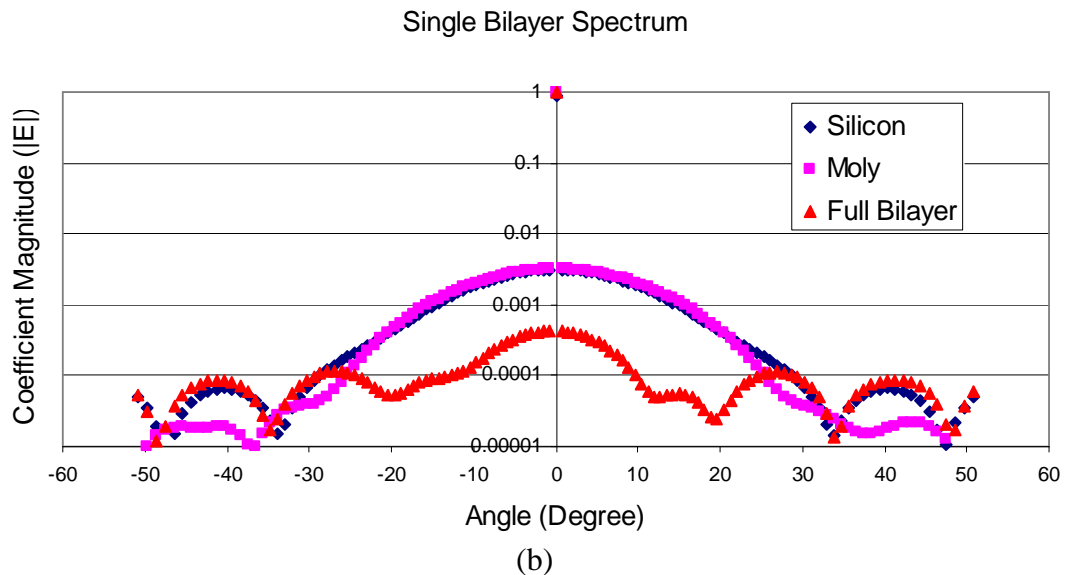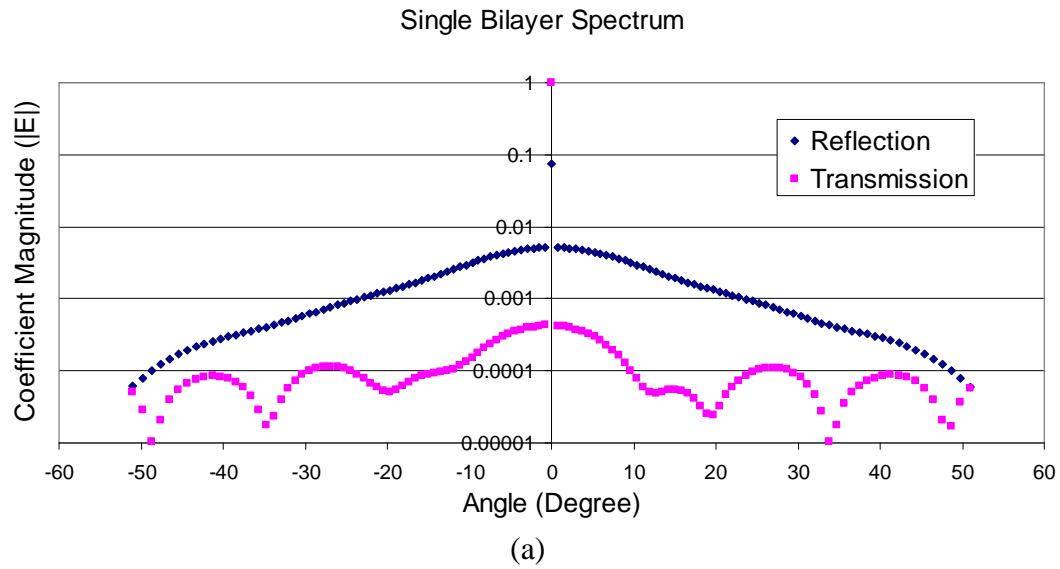
Figure 5.7. (a) The magnitude of the reflected and transmitted spectrum from a single bilayer. For small angles, the transmitted angular spread is at least 10X smaller than the reflected angular spread. (b) The transmitted spectrums for both individual layers of the bilayer as well as the total transmitted spectrum from the full bilayer.

forward diffraction is a good approximation. Figure 5.7b plots the spectrum of the forward diffracted field from each individual layer in the bilayer, as well as the spectrum of the forward diffracted field from the full bilayer. It can be readily seen that each layer taken individually has significantly higher forward diffraction than the full bilayer. The combined effect of the two layers reduces the forward scattered field by about 10X.

To further push the limits of this approximation, a full bilayer with a 2D Gaussian shape that was 30nm high with a FWHM of 30nm was simulated with FDTD and compared again to a single layer interface of the bilayer. The shape of this bilayer represents those bilayers that are very close to the substrate defect and buried deep within the multilayer. The shape of this bilayer is severely distorted, having a peak height deviation that is almost 11 times the thickness of the molybdenum bilayer. Figure 5.8a shows plots of the full bilayer's forward scattering relative to the forward scattering from just the top surface of the bilayer. The total magnitude of the forward scatter is increased by almost 10X from the smaller bilayers, which is expected from the more defective shape of the bilayers. It is also evident that the full bilayer again dramatically reduces the forward scattering compared to a single interface by over 10X! This clearly demonstrates that as the bilayer becomes more distorted, the full bilayer still helps to limit the forward scattering of a bilayer, but the magnitude of the error from this approximation is increased. However, these layers are buried deep within the multilayer close to the buried defect and their impact will be significantly limited from the decay produced from the propagation inward and outward of the stack.

As a final examination, a full 3D bilayer structure was tested with a Gaussian shape that was 3nm high and a FWHM of 30nm in both x and y directions. This layer would represent a typical bilayer in the upper half of a defective 3D stack. Figure 5.8b shows the transmitted spectrums of the full bilayer as well as a single layer interface of the bilayer for the largest magnitude cut line in the diffracted spectrum. Again, the simulations confirm that the full bilayer will reduce the total forward scatter produced from the distorted shape. The amount of reduction is smaller than that observed in 2D,

however, the magnitude of the largest error is roughly consistent at |E|~0.0003. This

shows that forward scatter can be neglected even for 3D defects.
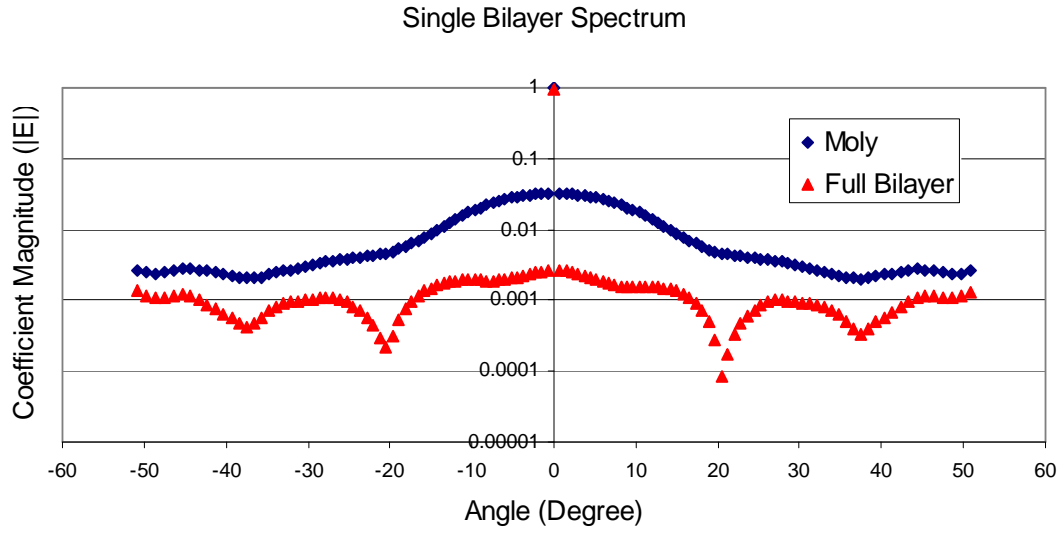
(a)
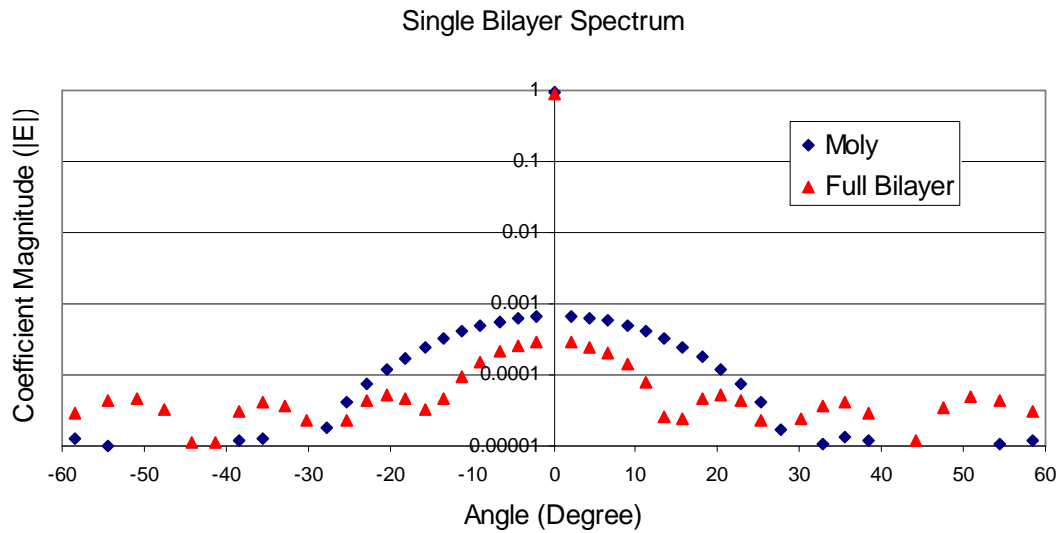
(b)

Figure 5.8. The transmitted spectrums for an individual layer of the bilayer as well as the total transmitted spectrum from the full bilayer for a bilayer with (a) 2D Gaussian shape that is 30nm high with a FWHM of 30nm. (b) 3D Gaussian shape that is 3nm high with a FWHM of 30nm in both x and y directions. The full bilayer still acts to limit the forward scatter even both of these regimes.

5.6 Justification for Neglecting Multiple Back Scatter Events

The optical homogeneity also allows a new method to neglect the effects of multiple back scatter events. A multiple back scattered wave is defined in this analysis as a plane wave whose k-vector has changed in the non-specular direction more than once when interacting with non-planar surfaces inside the multilayer. Essentially, the incident wave (k_0) can produce scattered waves (k_1) when interacting with a non-planar surface, but these scattered waves cannot again re-scatter from another non-planar surface to create a new wave (k_2) in the non-specular direction. Thus, a multiply bounced wave that contributes to resonance is not considered a re-scattered wave since it is a specular reflection. Neglecting re-scattering is an approximation that makes the new method a perturbational approach, where only the first order effects are calculated. This approximation limits each layer to a single back scatter event (R applied once, $k=1$) and prevents a growing set of waves from multiple back scatters.

A re-scattered wave's impact will be greatly influenced by its magnitude. A re-scattered wave that has bounced n times will scale as ρ^n, and since $|\rho| \sim 0.005$ for a single bilayer (see Figure 5.6a), the re-scattered waves will quickly die out in magnitude. However, the resonant nature of the multilayer dictates that there will be many of these re-scattered waves and one might question how the effects of all of these waves can be ignored. The answer comes from understanding bilayer interactions. It can be assumed that re-scattered waves will be largest when they re-scatter close the original scattering bilayer, since long propagations expose the wave to decay from the complex refractive index of the multilayer. Bilayers near the original scattering bilayer will have a similar

shape since the defect shape evolves rather than producing sharp layer differences. So

when the incident wave hits a non-planar bilayer, the surface height differences generate

a phase perturbation in the field which causes it to diffract. When this newly scattered

upward propagating field encounters a second non-planar bilayer, the second surface

height actually appears to be the inverse of the surface from which it first scattered.

Therefore, the second bilayer will very nearly undo the effects of the first surface upon

reflection, just as we saw in section 5.5 for transmitted waves. So, re-scattered wave

magnitudes from both near and far surfaces are constrained either by the inverse nature of

close bilayers or by the long propagation requirements for far bilayers. The

approximation that re-scattered waves can be ignored thus seems reasonably valid

because the optical homogeneity dictates that these re-scattered waves will be very small

and unable to resonate with the multilayer.

A first order estimate for the error from this approximation can be made by some

simple arguments. A re-scattered wave must scatter at least twice, resulting in

$|e| \sim (0.005)^2 = 25E{-}6$. This error estimate must further be multiplied by appropriate

reflections and transmissions, depending on the depth where the back scatter occurred.

This leads to a sum:

$$| e_{re-scatter} | \sim (0.005)^2 E_{inc}[t_1 r_{39} t_1 + t_2 r_{38} t_2 + ...] = (0.005)^2 E_{inc} \sum_{m=1}^{39} t_m r_{40-m} t_m$$

Again, t_m and r_m mean the transmission or reflection through m bilayers. Explicitly

calculating the sum results in a number of about 10, showing that a first order estimate of

the total error associated with neglecting re-scatter events is $|e_{re\text{-}scatter}| \sim .00025$, which is

quite small.

To test the validity of this approximation, the same Gaussian shaped bilayer in Section 5.5 was simulated as individual layers. The individual reflections can be added together with the analytic resonance included to obtain an approximate reflection calculation that excludes the effects of re-scattering. This approximate reflection can be subtracted from the full TEMPEST simulation to get an estimate of the magnitudes of any re-scattered waves present in the final solution. Figure 5.9 shows the errors in the reflected spectrums of the two calculations. Clearly, the error associated with neglecting re-scattering is very small (error $< 10^{-4}$), and these effects will only get smaller on a relative basis when resonance begins to start guiding the reflection behavior for structures with more than 7 bilayers.
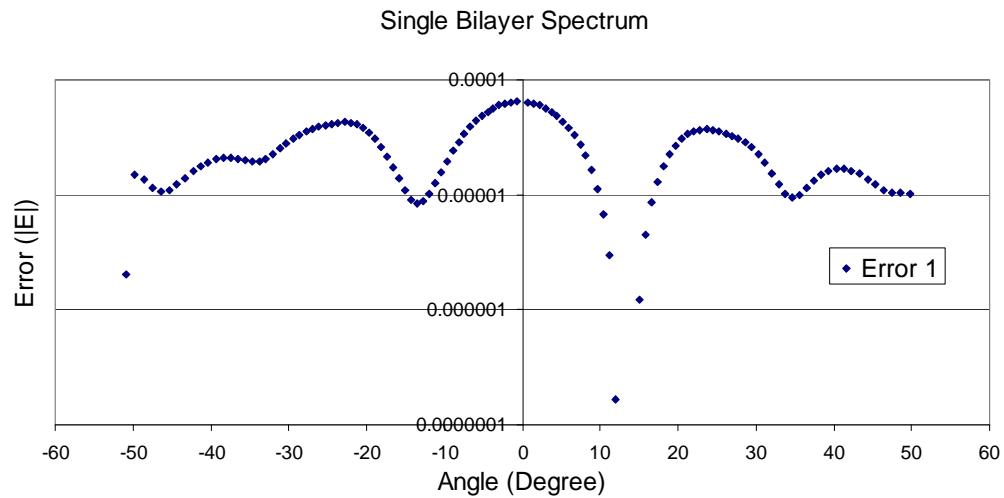
Figure 5.9. Upper bound on the error made by neglecting re-scattering. The error is less that 10^{-4} in electric field.

5.7 Anticipating Resonance

Analytic methods can be incorporated to model resonance within a fast simulation methodology. The following sections will provide analysis of a single bilayer and a multiple bilayer structure to show that resonance can be systematically understood for each bilayer in the multilayer and its effects summed analytically. The single bilayer analysis will provide information on modeling intra-bilayer resonance while the multiple bilayer analysis will show how to model inter-bilayer resonance. These analytic resonance terms can be calculated *a priori* and stored for later use. In this manner, the expected resonance of the multilayer can be anticipated, allowing a simulation methodology to eliminate any MBWs. Thus, a Primary Wave Approximation (PWA) is invoked, which will limit the creation of new waves to only those primary reflected or transmitted waves that spawn from the initial incident wave. A new methodology will then only need to track the primary waves during the calculation, and can apply the analytic correction factor to the primary waves as they propagate through the multilayer stack.

5.7.1 A Single Bilayer: Intra-Bilayer Resonance

A single bilayer forms the building block of the full multilayer stack. A better understanding of how this individual piece behaves will help elucidate effects that must
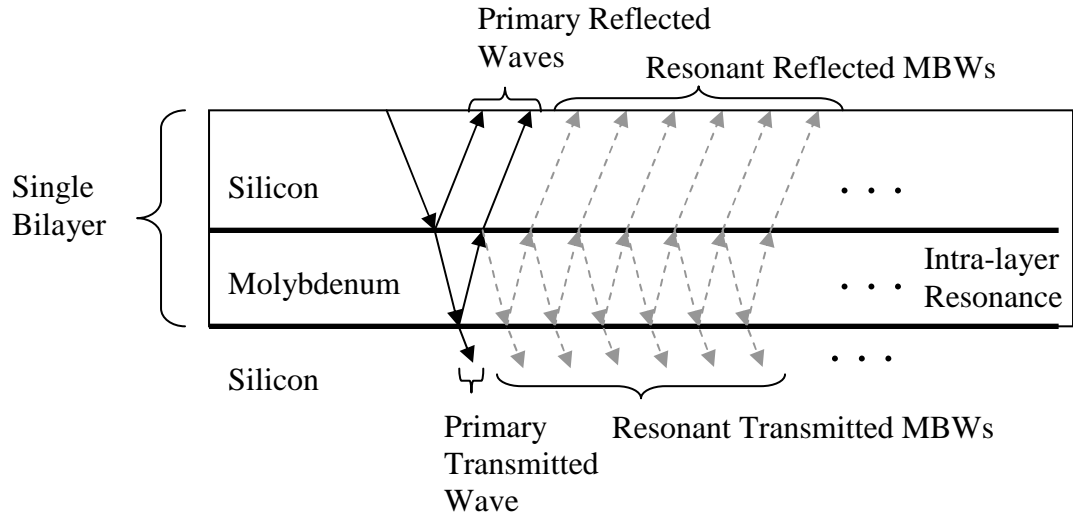
Figure 5.10. Wave picture of reflection from a single bilayer structure. The two primary reflected waves, the primary transmitted wave, the infinite number of resonant reflected MBWs, and the infinite number of resonant transmitted MBWs are labeled.

be properly modeled in a defective multilayer stack. Figure 5.10 shows a single bilayer with a silicon thickness of 4.14nm and a molybdenum thickness of 2.76nm, for a total thickness of 6.9nm. Propagating an electromagnetic wave in an arbitrary direction can be accomplished by multiplying by $S(\vec{x})$:

Equation 5.2: $S(\vec{x}) = e^{j\tilde{n}\vec{k}_0 \cdot \vec{x}}$

Here $\tilde{n}$ is the complex refractive index of the material, $\vec{k}_0$ is the free space wave vector,
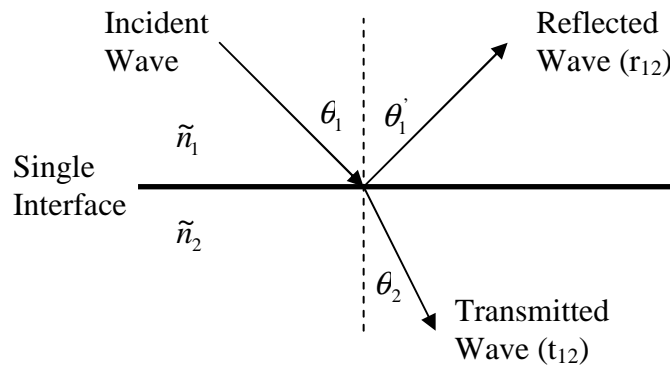
Figure 5.11. Reflection from a single interface is governed by the Fresnel equations, the law of reflection, and Snell's law.

and $\bar{x}$ is the distance propagated in the material. Reflections and transmissions from a single surface (see Figure 5.11) for a wave propagating from material 1 into material 2 can be calculated by solving the Fresnel equations, and the directionality of the reflected wave is given by the law of reflection, while the directionality of the transmitted wave is given by Snell's Law, shown below:

Equation 5.3: Snells Law: $n_1 \sin \theta_1 = n_2 \sin \theta_2$

Equation 5.4: Law of Reflection: $\theta_1' = -\theta_1$

Equation 5.5: Fresnel Equations:

TE Reflection: $r_{12} = \dfrac{\tilde{n}_1 \cos \theta_1 - \tilde{n}_2 \cos \theta_2}{\tilde{n}_1 \cos \theta_1 + \tilde{n}_2 \cos \theta_2}$; TE Transmission: $t_{12} = \dfrac{2\tilde{n}_1 \cos \theta_1}{\tilde{n}_1 \cos \theta_1 + \tilde{n}_2 \cos \theta_2}$

TM Reflection: $r_{12} = \dfrac{\tilde{n}_2 \cos \theta_1 - \tilde{n}_1 \cos \theta_2}{\tilde{n}_2 \cos \theta_1 + \tilde{n}_1 \cos \theta_2}$; TM Transmission: $t_{12} = \dfrac{2\tilde{n}_1 \cos \theta_1}{\tilde{n}_2 \cos \theta_1 + \tilde{n}_1 \cos \theta_2}$

Here $\tilde{n}$ represents the full complex refractive index of the material, while n represents the real part of the refractive index. Thus, the various reflections and transmissions on propagation of an electromagnetic wave, E_0, through the silicon and molybdenum layers can be calculated by Equations 5.2-5.5.

A common problem when propagating a wave into a multiple interface structure is the creation of new waves at each layer interface from multiple specular reflections. This is depicted in Figure 5.10 and results in quickly producing a geometrically growing set of waves which must be propagated simultaneously through the bilayer. For the single bilayer, there are two primary reflected waves and only a single primary transmitted wave, as shown in Figure 5.10. Figure 5.10 also clearly shows that the resonance for a single bilayer can be viewed as coming solely from the molybdenum layer (intra-layer

resonance), while resonance in the silicon layer can be handled by combining multiple bilayers (inter-layer resonance), as can be seen in the next section.

Primary waves are very easy to calculate since Equations 5.2-5.5 only need to be applied a few times, however, resonant rays require the application of Equations 5.2-5.5 a significant number of times. For clarity, each reflected and transmitted wave can be calculated by brute force using Equations 5.2-5.5 and summed to obtain the total reflection and transmission ($r_{1b,f}$, $t_{1b,f}$).

$$r_{1b,f} = S_s^2 \left[r_{12} + S_m^2 t_{12} r_{21} t_{21} + S_m^2 t_{12} r_{21} t_{21} (r_{21}^2 S_m^2) + S_m^2 t_{12} r_{21} t_{21} (r_{21}^2 S_m^2)^2 + S_m^2 t_{12} r_{21} t_{21} (r_{21}^2 S_m^2)^3 + ... \right]$$

$$t_{1b,f} = S_s \left[S_m t_{12} t_{21} + S_m t_{12} t_{21} (r_{21}^2 S_m^2) + S_m t_{12} t_{21} (r_{21}^2 S_m^2)^2 + S_m t_{12} t_{21} (r_{21}^2 S_m^2)^3 + ... \right]$$

Here $S_{s/m}$ is the operator from Equation 5.2 for a wave propagating at an arbitrary angle inside a silicon/molybdenum layer, and $r_{nb,f}$ means the reflection coefficient for n bilayers in the forward direction. Conversely, $r_{nb,b}$ would be the reflection coefficient for n bilayers in the backwards direction. These rather long equations can be simplified by pulling out common multiples:

$$r_{1b,f} = S_s^2 \left[r_{12} + S_m^2 t_{12} r_{21} t_{21} \left\{ 1 + (r_{21}^2 S_m^2) + (r_{21}^2 S_m^2)^2 + (r_{21}^2 S_m^2)^3 + ... \right\} \right]$$

$$t_{1b,f} = S_s S_m t_{12} t_{21} \left\{ 1 + (r_{21}^2 S_m^2) + (r_{21}^2 S_m^2)^2 + (r_{21}^2 S_m^2)^3 + ... \right\}$$

The above equations can be greatly simplified by adding the combination of multiply reflected waves inside the {…} brackets using the analytic sum from the well known infinite series:

Equation 5.6: $$\sum_{n=0}^{\infty} x^n = \frac{1}{1-x}$$

Thus, the full reflection and transmission coefficients for a wave propagating forward through a single bilayer are:

Equation 5.7:
$$r_{1b,f} = S_s^2 \left[r_{12} + \frac{S_m^2 t_{12} r_{21} t_{21}}{1 - r_{21}^2 S_m^2} \right]$$

Equation 5.8:
$$t_{1b,f} = \frac{S_s S_m t_{12} t_{21}}{1 - r_{21}^2 S_m^2}$$

The denominators of Equations 5.7-5.8 are easily recognizable as the analytic sum of the

infinite resonant reflected and transmitted waves within the molybdenum layer, since

they are identical in form to Equation 5.6. The remaining parts of the coefficients

represent information from the primary waves. Using Equation 5.6 simplifies the

reflection considerably by summing in closed form the effects of all the resonant waves.

The infinite sum can be stored as the analytic correction for resonance (ACR) of a single

bilayer.

Equation 5.9:
$$ACR_{1b,\theta} = \left[\frac{1}{1 - r_{21}^2 S_m^2} \right]$$

In this manner, the effect of the two primary reflected waves can be calculated

independently, and then the second primary reflected wave can be multiplied by the ACR

and added to the first primary wave to predict the full reflection coefficient for the

bilayer. Similarly, the primary transmitted wave can be multiplied by the ACR upon

passing through a single bilayer to predict the correct transmission coefficient. This

procedure can be written as:

Equation 5.10:
$$TRW_{1b,f}(\theta) = PRW_1 + PRW_2(ACR_{1b,\theta})$$

Equation 5.11:
$$TTW_{1b,f}(\theta) = PTW(ACR_{1b,\theta})$$

Here PRW stands for the primary reflected waves and PTW stands for the primary

transmitted wave, while TRW stands for total reflected wave and TTW stands for total

transmitted wave.

The reflection coefficient will be slightly different for a wave propagating backwards through bilayer, while the transmission coefficient will be the same. The backwards reflection coefficient can be found by setting S_s=1 (zero propagation distance in Silicon) on Equation 5.7:

Equation 5.12: $\qquad r_{1b,b} = \left[r_{12} + \dfrac{S_m^2 t_{12} r_{21} t_{21}}{1 - r_{21}^2 S_m^2} \right]$

Equation 5.13: $\qquad t_{1b,b} = t_{1b,f}$

5.7.2 Multilayer Structure: Inter-Bilayer Resonance

The above procedure derived the reflection and transmission coefficients for an arbitrary bilayer structure for both a forward and backward propagating wave. The calculation only relied on knowing the reflection and transmission coefficients of the two layers involved, and the rest could be calculated by propagating the waves throughout the geometrical structure. The process can be repeated to calculate the reflection and transmission coefficients of two bilayers stacked on top of each other. The distance between the bilayers would be zero (since the propagation through silicon and molybdenum was explicitly taken care of for the single bilayer case) and the reflection and transmission coefficients of the layers would simply utilize Equations 5.7, 5.8, 5.12, and 5.13. The resulting reflection and transmission coefficients are:

Equation 5.14: $\qquad r_{2b,f} = \left[r_{1b,f} + \dfrac{t_{1b,f} r_{1b,f} t_{1b,b}}{1 - r_{1b,f} r_{1b,b}} \right]$

Equation 5.15: $\qquad t_{2b,f} = \left[\dfrac{t_{1b,f}^2}{1 - r_{1b,f} r_{1b,b}} \right]$

This process can be repeated iteratively to solve for the reflection and transmission coefficients of any arbitrary multilayer structure by simply using the previous coefficients from a reduced bilayer structure. This process effectively reduces the problem to solving multiple two layer reflection calculations until the full multilayer is built up. In this manner, the reflection and transmission coefficients of an n bilayer structure would be:

Equation 5.16:
$$r_{nb,f} = \left[r_{(n-1)b,f} + \frac{t_{(n-1)b,f} r_{1b,f} t_{(n-1)b,b}}{1 - r_{1b,f} r_{(n-1)b,b}} \right]$$

Equation 5.17:
$$t_{nb,f} = \left[\frac{t_{(n-1)b,f} t_{1b,f}}{1 - r_{1b,f} r_{(n-1)b,b}} \right]$$

Again, the denominators of Equations 5.16-5.17 can be stored as the ACR for the appropriate bilayer:

Equation 5.18:
$$ACR_{nb,\theta} = \left[\frac{1}{1 - r_{1b,f} r_{(n-1)b,b}} \right]$$

In this manner, the ACR for every bilayer and every propagation angle can be calculated and stored for later use. These ACRs for multiple bilayers represent the inter-bilayer resonance depicted in Figure 5.3, where the ACR is the analytic sum of every possible wave path for re-reflection between the n bilayers above the single bilayer of interest. Once stored, only primary rays need to be tracked through the structure and the ACRs applied as needed. For instance, to calculate the transmission through n bilayers (where n > 2), only the primary transmitted wave needs to be tracked:

Equation 5.19:
$$TTW_{nb,f}(\theta) = PTW(ACR_{1b,\theta})^n \left[\prod_{k=2}^{k=n} ACR_{kb,\theta} \right]$$

Equation 5.19 applies the intra-bilayer resonance n times since it passes through n bilayers and it also applies the inter-bilayer resonance once for each bilayer set.
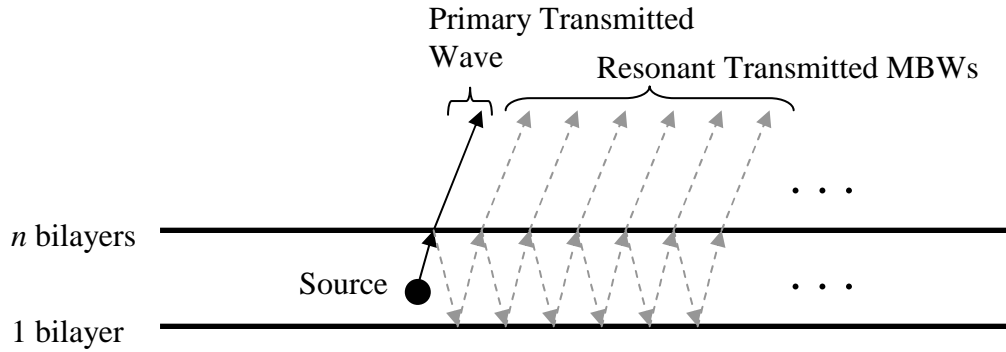
Figure 5.12. Wave picture of transmission from a source trapped between two mirrors, the upper mirror is made of *n* bilayers, while the lower mirror is just a single bilayer. One primary transmitted wave and an infinite number of resonant transmitted MBWs can be seen.

The same approach can be used to model an arbitrary dual mirror structure that will be useful during the push outward. Figure 5.12 demonstrates how an arbitrary plane wave in a spectrum behaves when it is trapped between two mirrors. Notice the similarities compared to Figure 5.10. The total transmission ($t_{nb,1b}$) of the reflected spectrum between an *n* bilayer upper mirror and a single bilayer lower mirror can be calculated algebraically by applying Equations 5.7-5.8 and 5.16-5.17 and following the same approach laid out in Section 5.7.3:

$$t_{nb,1b} = t_{nb,f} + t_{nb,f} r_{nb,f} r_{1b,b} + t_{nb,f} (r_{nb,f} r_{1b,b})^2 + t_{nb,f} (r_{nb,f} r_{1b,b})^3 + t_{nb,f} (r_{nb,f} r_{1b,b})^4 + \dots$$

Notice that the transmission and reflection coefficients for the upper mirror are assumed to be the forward direction, so that the silicon layer above the reflected primary waves is considered to be part of the bilayer above it. The lower mirror is then assumed to be a single bilayer in the backwards direction since it gave its silicon layer to the partial mirror above it. The equation above can be simplified by pulling out common multiples:

$$t_{nb,1b} = t_{nb,f} \left[1 + r_{nb,f} r_{1b,b} + (r_{nb,f} r_{1b,b})^2 + (r_{nb,f} r_{1b,b})^3 + (r_{nb,f} r_{1b,b})^4 + \dots \right]$$

And applying Equation 5.6 to obtain:

91

Equation 5.20:
$$t_{nb,1b} = \frac{t_{nb,f}}{1 - r_{nb,f} r_{1b,b}}$$

This equation is the transmission coefficient for a plane wave source sitting between two mirrors. The $t_{nb,f}$ is the transmission through the n bilayer mirror above it with all its resonance included, while the denominator is the ACR between the two partial mirrors:

Equation 5.21:
$$ACR_{nb,1b,\theta} = \left[\frac{1}{1 - r_{nb,f} r_{1b,b}} \right]$$

Equation 5.20 can now be recast into a primary wave interpretation by:

Equation 5.22:
$$TTW_{nb,1b}(\theta) = PTW_{nb,f} ACR_{nb,1b,\theta}$$

With Equation 5.22, an arbitrary plane wave can be propagated out of a dual mirror structure.

This iterative approach for calculating a reflection or transmission coefficient for a perfect multilayer structure is not the most efficient method. There are many methods which compute the coefficients in a much more direct manner. There are two reasons why the iterative approach is favorable for the EUV application. First, this approach allows the mathematics to be decomposed and easily interpreted in terms of the physical scattering inside the multilayer. The divisions between primary waves and resonant waves are easily distinguished, allowing their impact on the total reflection to be decoupled and handled separately. The analytic correction factor for each possible bilayer interaction can be pre-computed easily with this approach and stored for later use when analytic resonance corrections (ARCs) are needed in the code. The mathematical representation, while slightly less efficient, therefore supports the general strategy for solving the EUV scattering problem.

Secondly, the iterative approach allows an understanding of how each individual bilayer inside the multilayer contributes to the final reflection. Most analytic reflection calculations for stratified media use the equivalence of every layer to compress information, and thus an individual layer's contribution is lost in the final result. However, when extending such methods to the case when every layer has a different shape due to a defect perturbation, it is vitally important to understand the magnitude and phase contributions of each individual layer in the stack, and thus gain an understanding of the impact each layer makes relative to the total structure. The iterative approach allows this information to be captured so the individual layer contributions remain distinct.

5.8 Generalized Fast Simulation Methodology

This Section will briefly describe the ray tracing and the spectrum approaches. It will then explicitly describe the implementation of the general simulation methodology outlined in Section 5.4. The three key approximations described previously will be invoked to create a very fast method for simulation.

5.8.1 Geometrical Optics: Ray Tracing

Ray tracing can provide excellent results only when diffraction is minimal, since the wave front needs to be fairly uniform. This fact places severe limitations on the applicability of ray tracing to electromagnetic scattering problems, however, it could be successfully used for two of the three segments of the EUV scattering problem. Since the

forward diffraction is minimal, ray tracing can be used for delivering the electromagnetic energy into the multilayer. The reflection from a non-planar surface can also be handled in a straightforward manner with the Fresnel equations. On the other hand, since diffraction is expected from the reflected field, problems would be expected if ray tracing was used to propagate the reflected fields out of the multilayer without first transforming the diffracted fields into plane waves.

During ray tracing, a ray is propagated forward into the multilayer stack using local Fresnel reflections and transmissions, using the full complex refractive index of the multilayer stack. A ray can be interpreted as a local electric field value along the sampled wave front and it behaves identically to a plane wave. Thus, Equations 5.2-5.5 can fully describe a ray's behavior when interacting with the interfaces within the multilayer.

5.8.2 Fourier Optics: Spectrum Approach

Fourier optics is another logical method for propagating the reflected fields into or out of the multilayer stack, since the Fourier transform can decompose the electric field into a set plane waves which can be easily handled via the Fresnel equations. Fundamentally, this approach works because the upward waves, once generated, undergo minimal forward diffraction as shown in Section 5.5. As such, this spectrum approach can be expected to work very well for the push inward, the reflection from the non-planar interface, and the push outward of the EUV reflection problem, since the spectrum approach is very robust.

The spectrum approach uses the Fourier transform to decompose the complicated scattered field inside the multilayer into a simple set of plane waves. The plane waves can

then interact with the multilayer and diffraction is handled automatically by updating the phases of the plane wave spectrum as it propagates. In this manner, characterizing how plane waves interact with the multilayer will allow any complicated scattering to be analyzed. A plane wave will interact with a flat interface as described by the Equations 5.2-5.5. A plane wave impinging on a non-planar interface will have its reflected phase modified by twice the geometrical height variation of the surface, given by the modified phase equation:

Equation 5.23: $\qquad \varphi(x, y) = 2nk_0(z(x, y) - z_0) = \dfrac{4\pi n(z(x, y) - z_0)}{\lambda_0}$

Where $z(x,y)$ is the surface height, z_0 is the surface height of the defect free surface, k_0 is the free space wave number, n is the real part of the refractive index, and λ_0 is the free space wavelength. This doubling of the phase difference is entirely analogous to the SSA approach [5] to account for the down and up propagation of a reflected field. The transmitted field would have its phase modified by the same equation, except with no phase doubling and n replaced by Δn, where Δn is the difference in refractive index for the upper and lower medium.

The spectrum approach also suffers from multiply bounced waves creating a geometrically growing set of waves to compute, but the same PWA approach can eliminate the multiply bounced waves, and the analytic solutions for resonance can be applied to waves as they propagate through the multilayer. Thus, a finite set of waves can be used to accurately calculate the reflected fields.

5.8.3 Implementation of the Fast Simulation Methodology

Stage 1: The Push Inward:

To define the geometry, an input matrix of numbers is needed that represents the locations of the interfaces between the molybdenum and silicon inside the multilayer. Once this is input, the push inward (first stage) can begin and a sampled incident wave front can be used to trace the electromagnetic energy into the multilayer in the form of rays. For simplicity, evenly spaced rays are used, though in principle any number of better sampling patterns can be used, such as a Gaussian distribution, to provide better ray density near the defect and thus lessen the number of rays needed to be traced at the edges.

The PWA approach combined with the analytic anticipation of resonance is used to limit the creation of new rays to only the primary reflected and transmitted waves that spawn from the initial downward traced ray through the multilayer. The analytic correction factor for both intra and inter bilayer resonance must be applied to the downward traced rays as they propagate through the stack and is based on the number of bilayers traversed (as per Equation 5.19). The primary reflected rays that are created from ray tracing are left in their original positions to be propagated out of the multilayer by a later method.

The ray position history of the initial downward traced rays can be used to understand how energy moves through the multilayer stack. The actual position histories for one such defect are plotted in Figure 5.13 for a normally incident wave front. The horizontal lines are the interface locations between molybdenum and silicon layers, while the vertical lines represent the paths that actual traced rays took when propagating

96
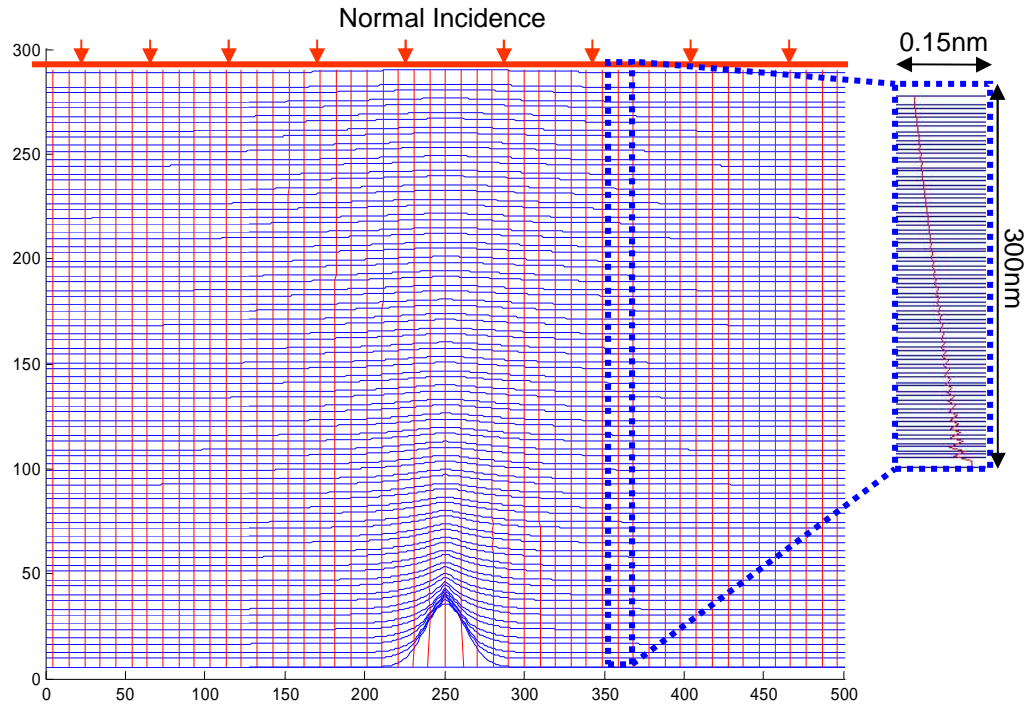
Figure 5.13. Position histories of rays traced into a sample defective multilayer. Zoomed image shows local detail of a ray traversal down through the stack.

downward through the multilayer. These paths are very straight, showing very minimal diffraction from the forward propagation, as expected from the optical homogeneity of the problem. A zoomed in picture of a representative ray path shows more local detail of how individual rays wiggle as they move. A shift of only 0.15nm over the course of 300nms of propagation is seen. Of interesting note, is that the ray will slightly bend away from the local normal and the defect, which is due to the multilayer refractive indices being less than 1.

The spectrum approach can also be used for the push inward instead of ray tracing, by simply applying the same principles. The entire wave can be propagated into an assumed defect-free structure since the forward diffraction is minimal. The intra- and inter-bilayer resonance can be applied based on Equation 5.19, depending on the depth of each bilayer the incident wave passes. Since the spectrum approach deposits energy

97

based on a perfect structure, some minor phase information may be lost compared to ray tracing where the local phase information of tracing through a defective structure can be captured. The differences between using the spectrum approach or ray tracing is very small in practice, but Chapter 6 will show that there can be larger differences when dealing with specific types of multilayer defects.

Stage 2: Reflection from a Non-Planar Surface:

The initial downward push into the multilayer will result in one newly spawned, reflected ray for every layer in the multilayer stack, as shown illustratively in Figure 5.4. The inward push is finished when the initial downward traced ray propagates fully through the multilayer stack, leaving the newly reflected rays sitting at their original spawned locations within the multilayer. Ray tracing has naturally calculated the second stage of the problem: the reflection from a non-planar surface, and now the reflected fields must be propagated out of the multilayer stack. The reflected rays, however, do not sit on a regular x and y grid due to the lateral movement and wiggling of the rays as they propagated through the non-planar multilayers. The rays must be moved back to a regular grid in order to efficiently handle the outward push. Linear interpolations between rays are used to obtain the field values on a regular grid. For 3D interpolations, triangular planes are used, as shown in Figure 5.14, to move the electric fields back to regular grids. Once the rays are reordered to a regular grid, the rays must now be flattened onto a single plane to prepare for the push outward. This flattening can be accomplished by doubling the phase differential between rays located near the defect and those located near the edges of the domain, to account for the round trip propagation of the reflected fields.
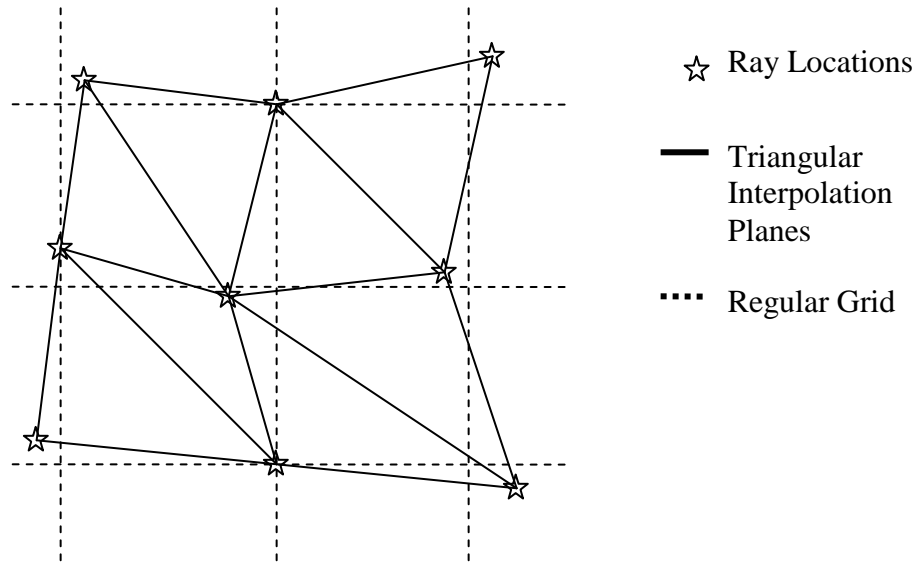
Figure 5.14. Schematic showing the ray locations and the interpolation planes. The regular grid is superposed over the rays, and the intersections of the dashed lines are where the electric field values are interpolated.

If the spectrum approach was used on the inward push, the reflection from each non-planar surface can be calculated using Equation 5.5 to obtain the initial magnitude and phase of the reflected wave, and the modified phase of the reflected wave can be adjusted by Equation 5.23. In this manner, the electric fields are already on a regular grid inside the multilayer and are flattened by Equation 5.23. At this point, the spectrum approach has calculated the reflected fields sitting inside the multilayer, just as the ray tracing approach would have done.

Stage 3: The Push Outward:

Initially, ray tracing was explored to move the rays back out of the multilayer, but significant errors were encountered. Each primary reflected ray was traced upwards through the stack and the resonant corrections applied based on Equation 5.19. These rays never created downward propagating rays since the PWA eliminated their generation. Once each ray was traced back out, the rays were again moved back to a

99

Ray Tracing at Normal Incidence
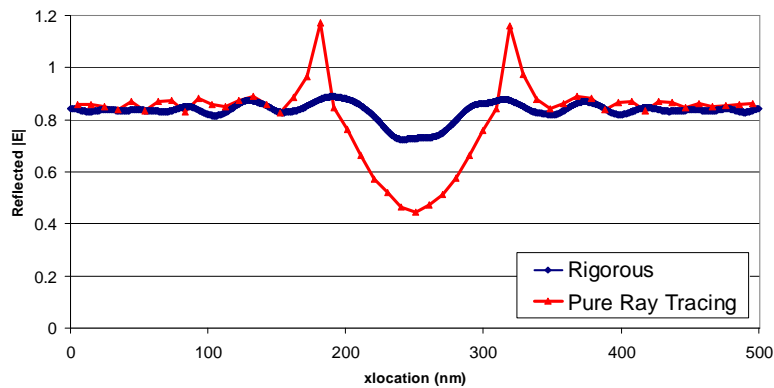
Figure 5.15. Failure of ray tracing to predict the correct diffraction pattern exiting the multilayer, as expected from the ray caustics and shadow boundaries.

regular grid and recombined to form a global reflection for each layer. These reflections could then be added together to produce the total reflection from the multilayer. The total calculated electric field reflection from this ray tracing approach is plotted along with an FDTD simulation for comparison in Figure 5.15. A major difference between the two simulation methods immediately stands out, namely the large discrepancy between the central portion, where the ray tracing reflection shows very large spikes and a huge central dip in the electric field.

The discrepancy in the central portion of the reflection is due to the angular nature of the outward propagated rays. The reflected rays inside the multilayer stack are generally scattered to small angles, but must propagate out a distance of as much as 20λ, resulting in rays that cross many neighbors' paths on the outward journey. These crossings give rise to shadow boundaries and ray caustics, which would normally force a lateral redirection of energy via diffraction. However, ray tracing is incapable of modeling these diffractive effects, showing the outward propagation can no longer be described as simple geometrical optics. Ray tracing has been augmented to include the

effects of diffraction via the Geometrical Theory of Diffraction (GTD) [66], however, the strength of GTD lies in its ability to predict far field results. For EUV mask blank scattering, the near fields are desired since all the machinery to calculate the far field image under partially coherent light already exists. Thus, the resulting diffraction during the outward propagation through the multilayer stack requires a new method for accurate calculations.

For the final stage of the calculation, the push outward, the reflected fields (whether calculated by ray tracing or the spectrum approach) can then be Fourier transformed into its plane wave spectrum. Each plane wave in the spectrum of every layer can be considered a primary wave that must be pushed back up through the stack. The resonant corrections (both intra-bilayer and inter-bilayer) previously applied on the push inward have allowed the correct field to be incident on the individual layers, but resonant corrections must be applied a second time to account for the propagation during the push outward. As such, Equation 5.9 is used to apply the intra-bilayer $ACR_{1b,\theta}$ to the reflections from the molybdenum to silicon interfaces, and these plane waves are propagated up one layer so that they sit above the full bilayer that generated them. This ensures that intra-bilayer resonance is applied to the source bilayer for each reflection. Again, re-scattering between defective layers is neglected because the re-scattering interaction magnitudes fall very rapidly due to a bilayer's reflective properties. Thus, moving the plane wave spectrum out of the multilayer can be made easier by transforming the upper layers into perfect unperturbed layers (re-scattering neglected) and these perfect bilayers can be further compacted into a single perfect partial mirror (a single surface with no distortions). A single bilayer below the source (essentially the
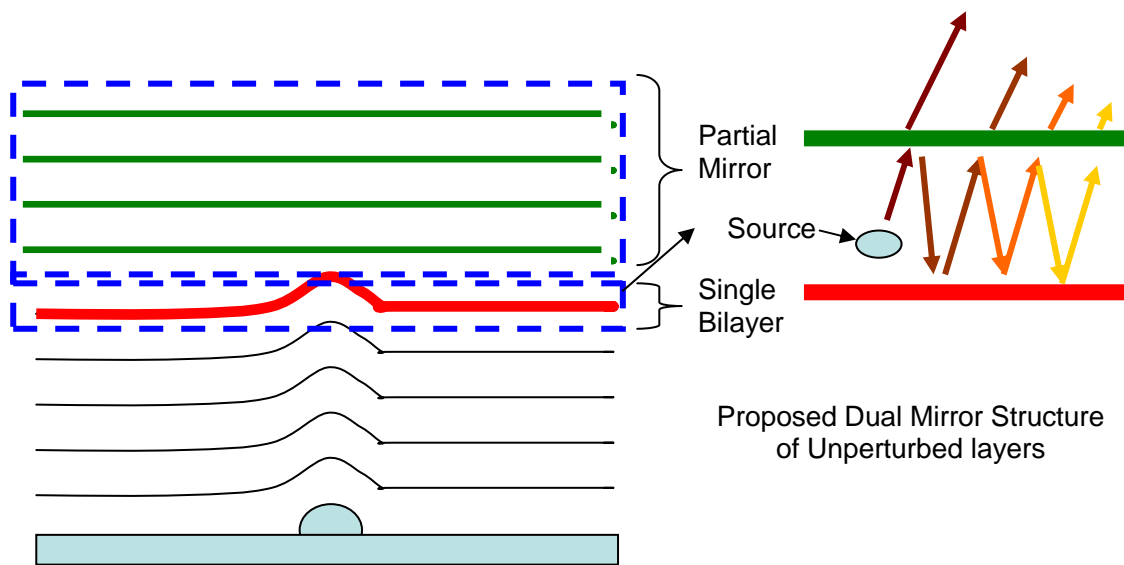
Figure 5.16. Proposed dual mirror structure for incorporating resonance into the outward propagation. The reflection from the layer of interest acts as a source radiating between two mirrors. All bilayers above the layer of interest are assumed to be ideal, unperturbed layers that can be flattened into a single partial mirror. The layer that generated the reflection will act as an ideal bilayer beneath the source. The source then radiates upward using an analytic model to account for resonance.

bilayer from which the reflection came) is also compacted into a perfect partial mirror. The plane wave spectrum from an arbitrary layer will therefore act as a source radiating upwards inside of a dual mirror structure. This proposed dual mirror structure can be seen in Figure 5.16, where the source now sits between two partial mirrors. The source is now allowed to radiate and the analytic solution for the transmission upwards can be calculated from Equation 5.22. In this manner, the spectrum can be propagated through the upper layers with resonance included on an angular dependent basis by only applying a single inter-bilayer correction. Once the entire spectrum has been propagated out of the multilayer, the spectrum can be added to every other layer's spectrum and inverse Fourier transformed, giving a final total reflection.

5.9 The Importance of Resonance

It should be intuitive that resonance is an important factor in modeling a Bragg

reflection structure, and this Chapter has argued that analytic resonance calculations must

be included to obtain accurate calculations. To prove this, however, the analytic

corrections within the code can be turned off to demonstrate what happens to the PWA

when resonance is ignored. Figure 5.17 shows the reflected field magnitude from a defect

free mirror for the new method when resonance is turned on and off for as a function of

the number of bilayers in the stack. When resonance is included, the method produces

results in good agreement with an analytic calculation for the reflection from the stack,

which levels off around |E| ~ 0.85. When resonance is turned off, the ray tracing method

produces a reflection magnitude that does not even conserve energy. The large

discrepancy in the background energy when resonance is turned off can
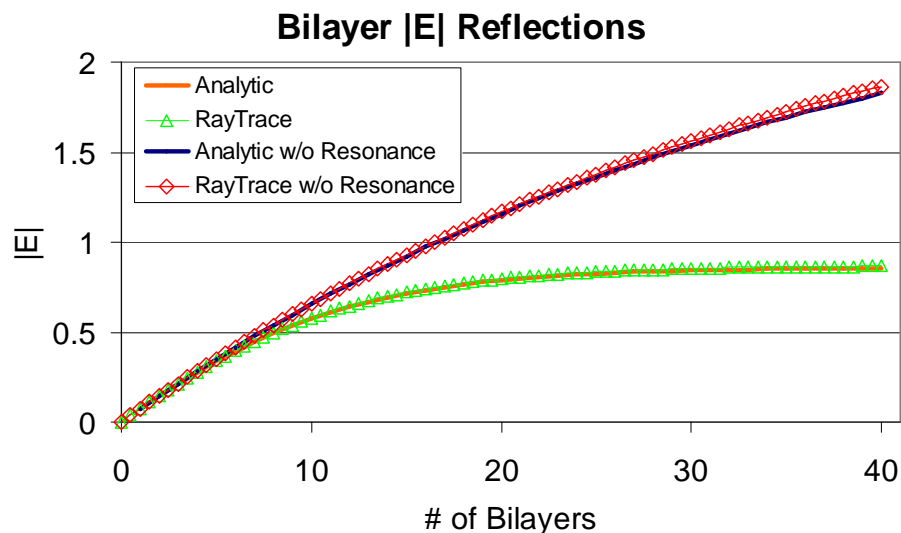
Figure 5.17. Reflection from a defect free multilayer of varying bilayer numbers. Both the hybrid
raytracing/spectrum and the full spectrum models are shown along with an analytic calculation with
and without resonance terms.

be shown to stem from the PWA. The same analytic model can be plotted once again, but with all resonance terms thrown out (essentially a PWA analytic approach), giving the dark line on the same plot. Notice that for less than about 7 bilayers, the reflection can be approximated quite well by the PWA, however, when the number of bilayers is larger than 7, the reflection coefficient of multiple layers grows large enough that the resonance terms can no longer be ignored. Notice, however, that both models predict the same as the analytic model without resonance. The nature of the PWA is that it captures only the first terms in an infinite series of waves which must all be added to get the correct result. The infinite series is actually an alternating series where the first terms are positive and alternate sign afterwards. This means that each layer's reflection will be over calculated, and this leads to the large over estimate of the reflection where energy is not conserved.

5.10 Conclusions

By reinvestigating the problem specific attributes of EUVL, a new methodology has been proposed for simulating buried defects inside of EUVL multilayer mask blanks. The optical homogeneity and smoothness of EUVL mask blanks, along with the small numerical aperture of EUVL systems have allowed three key approximations to be made. First, that the forward scatter from wave propagation inside the multilayer can be neglected. This approximation stems from the nature of the bilayer, where each interface largely cancels in the forward scattered direction, resulting in an order of magnitude reduction in the forward scatter compared to a single layer. Neglecting forward scatter is crucial to minimizing the number of waves propagating in the multilayer. Second, that

resonance can be anticipated and analytically corrected with closed form summations of resonance from parallel surfaces of a bilayer or multilayer. Both intra-layer and inter-layer resonance are analytically corrected for during the push inwards, while the dual mirror structure only requires a single inter-bilayer resonance correction to be applied on the push outwards. Finally, any re-scattering event that stems from multiple back scatter events will be sufficiently small that it can be ignored. This approximation limits each layer to a single back scatter event, so that scattering events never produce more scattering events.

The general scattering problem from EUV mask blanks was decomposed into 3 stages, and both geometrical optics and Fourier optics were leveraged to solve the individual segments of the reflection calculation. The newly proposed method can be viewed as a generalization of the SSA method to incorporate the entire multilayer stack by using a dual mirror structure to approximate the resonance conditions. Analytic models for resonance are seeded throughout the calculation and a primary wave approximation (PWA) is used to prevent tracking the multitude of newly spawned waves that are generated inside a resonant cavity. The perturbational approach created here will allow more thorough, quantitative studies on EUV buried defect printability to be accomplished on desktop computers.

6   Accuracy and Speed of Ray Tracing Methodology

This Chapter will systematically assess the accuracy and speed of the new ray tracing methodology for simulating EUV buried defects. A detailed investigation of an example defect will be shown, comparing the near fields, images, and spectrums of the buried defect to those predicted by FDTD and SSA. Both the dip in the image and the corresponding spectrums will be analyzed and compared. A scattered spectrum analysis will provide insights into the physical scattering process of buried defects, showing that the spectrums of the individual layers within the multilayer have a large impact on the total reflected spectrum. A speed analysis of the new method along with trade offs on speed and accuracy will also be demonstrated. Finally, a thorough investigation of the accuracy of FDTD is presented to better understand the differences between FDTD and the new method. It will be shown that FDTD can suffer from temporary convergence lulls as well as numerical dispersion problems when simulating resonant structures. These problems can cause significant errors to be made, and calls into question the belief that FDTD is a gold standard for simulating EUV buried defects.

The "dip strength" is a common metric for defect analysis which measures the strength of the intensity dip and normalizes it to the background. Mathematically, the dip strength is defined as:

Equation 6.1: $DipStrength = (I_{background} - I_{min\,imum})/I_{background}$

This metric will allow the new method's applicability to be assessed for a host of differing 2D and 3D geometries. More specifically, the defect's shape and size will be considered. When referring to a defect's shape and size, these properties are measured for the defect as originally on the substrate, and do not account for any change produced by the multilayer growth.

Before moving into the results of the above studies, it is useful to describe the simulation parameters. All substrate defects were simulated with the smoothing process developed by Mirkarimi [41] and modeled by Stearns [42]. The multilayer consists of 40 bilayers, with molybdenum below silicon in the bilayer. The bilayers were 6.9nm in depth with 60% silicon (4.14nm) and 40% molybdenum (2.76nm) with a 2.5nm ruthenium capping layer on top. A 13.4nm wavelength was used for all simulations. The refractive indices used were $n_{si} = 0.999942 - j*0.00182099$, $n_{mo} = 0.922769 - j*0.00621555$, $n_{ru} = 0.888839982 - j*0.0160783362$ which were obtained from [67]. All FDTD simulations were performed using UC Berkeley's TEMPEST software, and all aerial image calculations were performed with Panoramic Technologies aerial image software. All aerial image calculations were performed using a numerical aperture (NA) of 0.3 and a partial coherence factor (σ) of 0.3. These parameters were used for all simulations in this Chapter unless otherwise noted.

6.1 Detailed Accuracy Results

The methodology proposed in Chapter 5 has produced excellent results when compared to FDTD simulations. The computed magnitudes and phases of the near fields
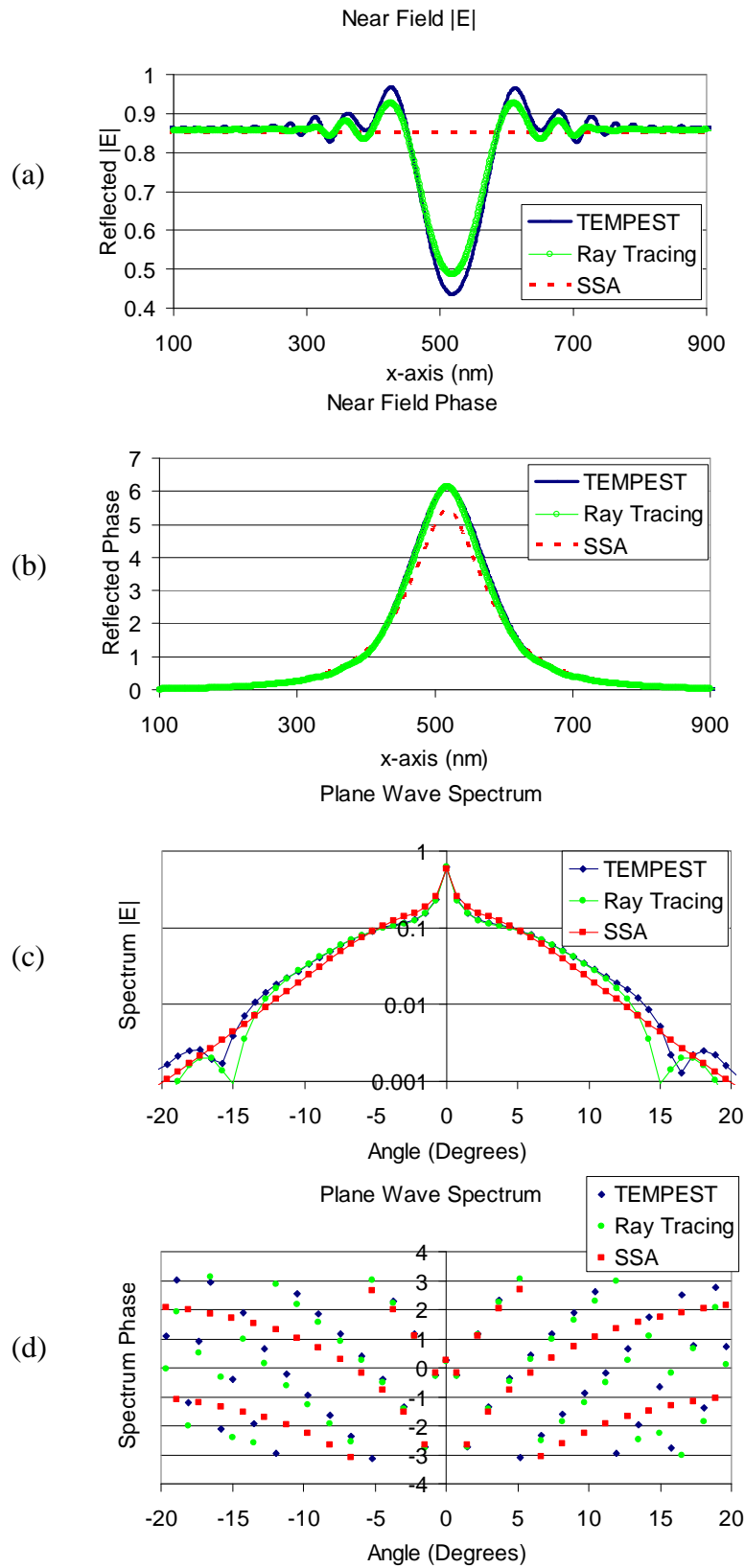
Figure 6.1. Reflection from a 60x60nm Gaussian defect for various methods. (a) The near field magnitude, (b) the near field phase, (c) the spectrum magnitude, (d) the spectrum phase.

for FDTD, SSA, and the new methodology are shown in Figure 6.1a and 6.1b for a 60x60nm Gaussian defect (60nm high, 60nm FWHM) coated with the smoothing process. The SSA underestimates the impact of the phase and also assumes there is no magnitude disruption in the near field. The newly proposed methodology accurately predicts the phase and closely estimates the magnitude perturbations in the near field. A better understanding of how each method compares to FDTD, is to Fourier transform the fields into their plane wave spectrums. The spectrums of each method can be seen in Figure 6.1c and 6.1d. The SSA method is clearly off in the phases of the reflected spectrum, but does a decent job at computing the magnitudes of the plane waves. The newly proposed method does a good job of matching the phases of the plane waves, and closely matches the magnitudes of the plane waves out to about 10º. Recall, however, that EUVL systems use small NAs and only a small cone of reflected light will actually enter the collection optic. For a realistic system at 4X, NA=0.3, and partial coherence $\sigma = 1$, some energy from all plane waves between 8.63º will be collected. This means that our method does an excellent job of matching the TTL spectrum of the FDTD simulation.

Since the TTL spectrum is excellently matched, propagation of the spectrum through an aerial image simulator should produce excellent results as well. The images through focus of a 60x60nm Gaussian defect coated with the smoothing process are shown in Figure 6.2. Notice that the newly proposed method nearly identically overlays the images from the FDTD simulator. Thus, excellent agreement at all focal values are achieved.
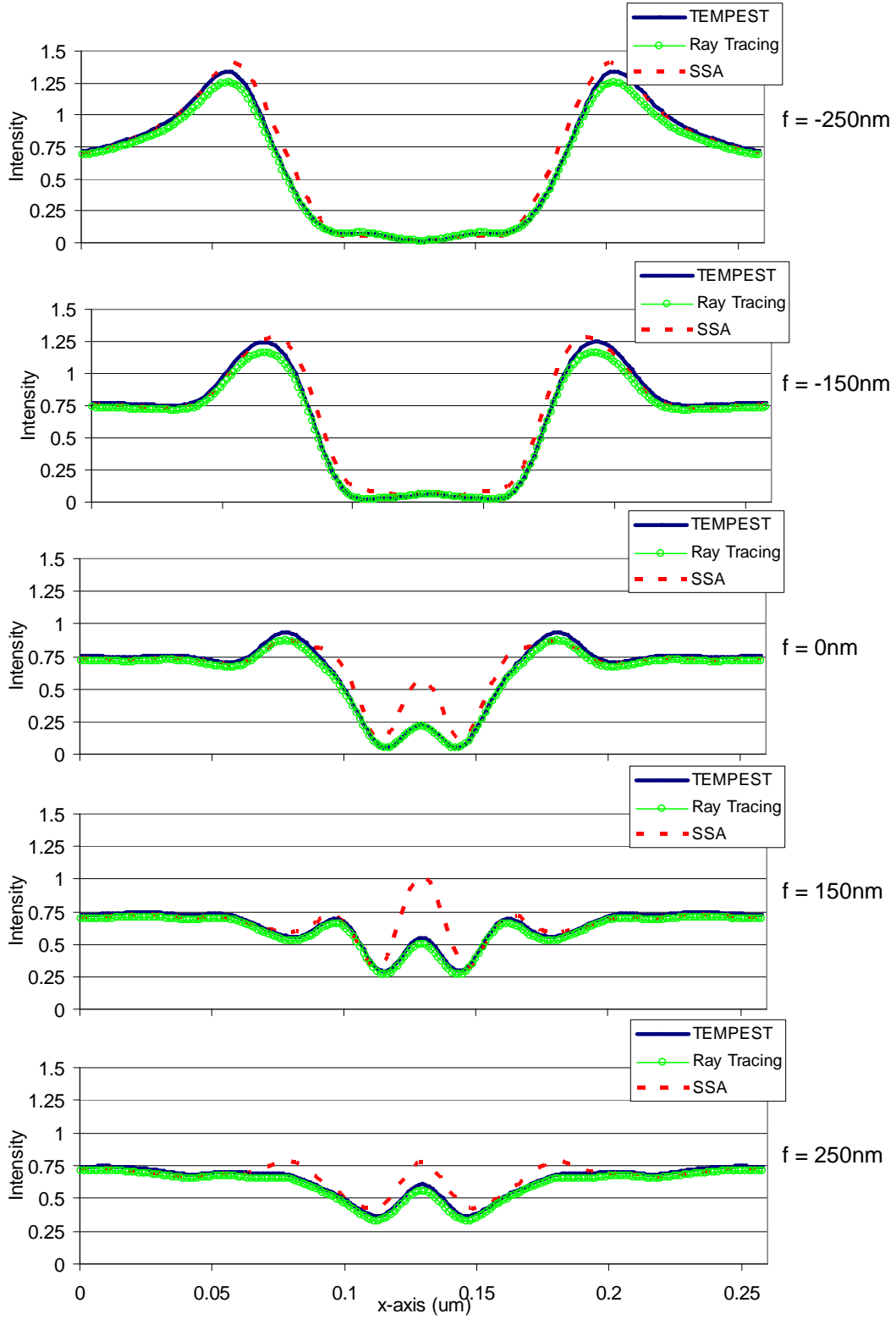
Figure 6.2. The through focus aerial images of a 60x60nm Gaussian defect, for σ=0.3 and NA=0.3.

6.2 Accuracy of 2D Line Defect Simulations

A thorough investigation of defect shape would be very challenging since defects can exist in any arbitrary shape, however, a good understanding of a each methods' accuracy across variations in shape can be handled by investigating two extreme shapes: a box defect and a Gaussian defect. The box defect represents defect shapes that are most topographically challenging and could pose the greatest challenge to the fast simulators in their efforts to achieve results as accurate as TEMPEST. The steep sidewalls and corners could potentially generate scattering that is more difficult to capture within a fast simulator. The Gaussian defect represents defect shapes that are least topographically challenging since the defect is already smooth, and the scattering behavior is expected to be easier to capture in a fast simulator. Real world defects would typically fall somewhere between these two extremes; however, a simulation method that is accurate at both extremes, can be expected to behave accurately for any defect falling between the two extremes.

The defect size is an easier consideration and can be uniquely identified with two numbers, a width and a height. Box defects will be identified by the obvious width and height characterizations of a box, and will be designated as "width x height". For example, a 20nm wide and 20nm high defect will be designated as 20x20. Gaussian defects will be formulated in the same structure if we take their Full Width Half Max (FWHM) to characterize the defect's width, and the peak height to characterize the defect's height. In this manner, a Gaussian defect with a 20nm FWHM and a 20nm peak height will be designated as 20x20. When varying defect size, all defects in this study

111

will have equal widths and heights, so a 70x70nm defect can be referred to as simply a 70nm defect.

Figure 6.3a shows the in focus image dip strengths of 2D line box defects for the three methods. It can be easily seen that the ray-tracing method gives very good agreement with the TEMPEST results for all defect sizes, while the SSA method gives mixed results. At small and large defect sizes, the SSA method correctly predicts the image dip strength, but underestimates the image dip strength in the transition region for mid-sized defects. A simple and common threshold model for the defect's resist printability can now be applied, where the defect becomes printable when the image minimum dips to 0.3 (30%) of the clear field, or equivalently, the defect dip strength is 0.7 (70%) of the clear field. Applying this metric for printability, 2D line box defects become printable in focus when their size becomes greater than about 60x60nms. Thus, any 2D line box defect can be tolerated under this 60nm limit. While this Chapter does not specifically investigate defect printability in the presence of features, it has been shown that sub-printable defects in the clear field can become printable in the presence of features [68]. This fact makes the accurate calculation of image dip strength extremely important in the transition region, and provides extra incentive to have a fast and accurate simulation tool across all defect sizes.

The through focus behavior of the 2D line box defects are shown in Figure 6.3b and 6.3c for two focus settings of ±150nm, corresponding to ±2 Rayleigh Units (RU). The ray-tracing method once again shows very good agreement with the TEMPEST results across all defect sizes, and even the SSA method produces good results at these focal regions. These graphs show that 2D line box defects imaged at -150nm focus (-

2D Line Box Defect Printability

Figure 6.3. (a) Plot of the image dip strengths at best focus. (b) Plot of the image dip strengths at -150nm focus. (c) Plot of the image dip strengths at +150nm focus. (d) Plot of the image dip strengths for a 60x60nm box defect through focus.

2RU) become printable for defects greater than about 30nms. Thus, the defect tolerance is cut in half when tight focus controls cannot be implemented. The data also confirms that these buried defects are behaving as phase defects, since they print worse in one direction of focus than the other (notice none of the defects print at +150nm defocus), an effect shown by Watanabe[24]. It should be noted that the SSA cannot in general be assumed to give correct predictions of image dip strength at all regions of focus, as might be implied from the two focal positions (±150nms) above. Figure 6.3d shows the predicted image dip strengths through focus for a 60x60nm box defect for all three methods. As can now be clearly seen, between ±150nms, the SSA method can show significant deviations from TEMPEST, while the ray-tracing method gives very good accuracy across all focal settings.

The same analysis can be done for Gaussian defects and the same conclusions are achieved. Figure 6.4a, 6.4b, and 6.4c show the image dip strengths of 2D line Gaussian defects at the same focal positions studied above. Once again, very good agreement with TEMPEST can be seen for the ray-tracing method for all defect sizes. The SSA method, again has difficulties predicting accurate image dip strengths in the transition region between printability at focus, but gives good results at the two out of focus settings. The graphs show that 2D line Gaussian defects can be tolerated for those less than 45nm when in focus, while this tolerance drops almost in half to 25nms if tight focus controls cannot be implemented.

A surprising conclusion from the above results is that Gaussian defects print worse than box defects. In fact, some Gaussian defects can have up to twice the impact of a similar sized box defect! Figure 6.5 shows the image dip strengths of Gaussian and box
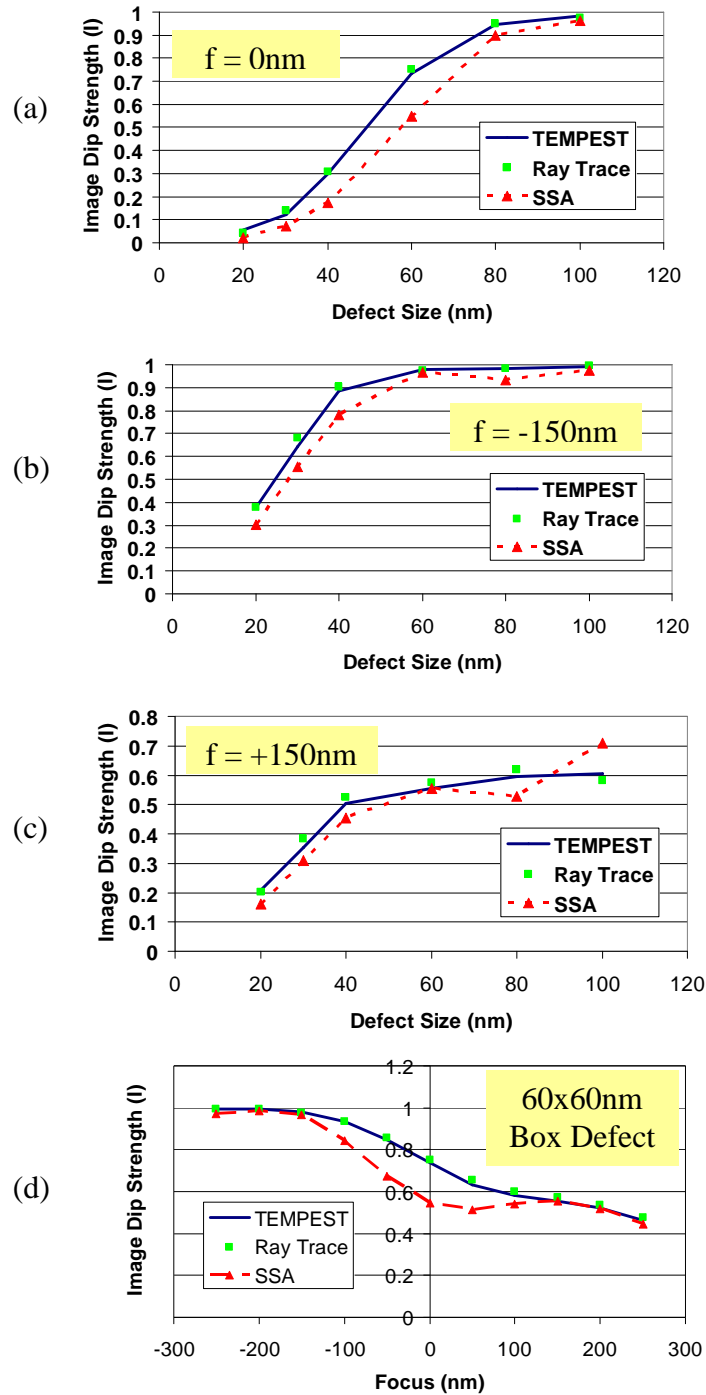
2D Line Gaussian Defect Printability
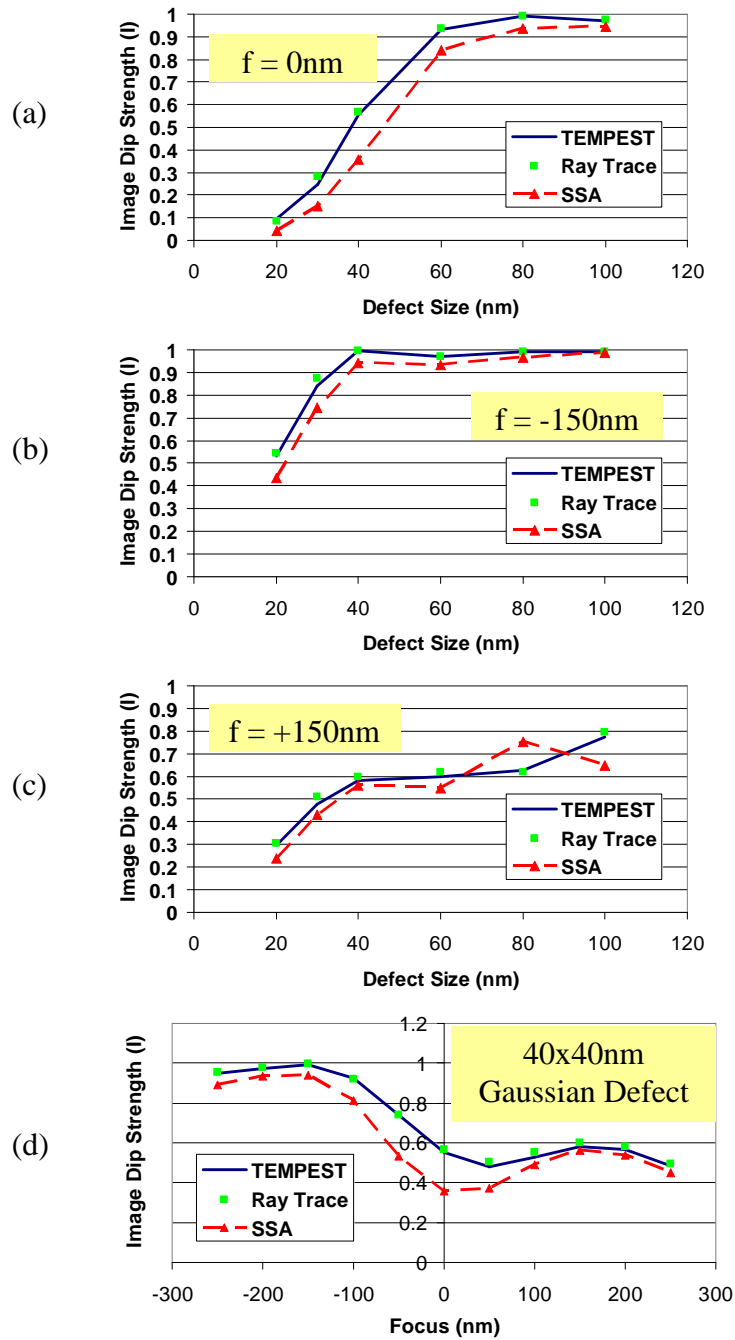
Figure 6.4. (a) Plot of the image dip strengths at best focus. (b) Plot of the image dip strengths at -150nm focus. (c) Plot of the image dip strengths at +150nm focus. (d) Plot of the image dip strengths for a 40x40nm box defect through focus.

Defect Printability
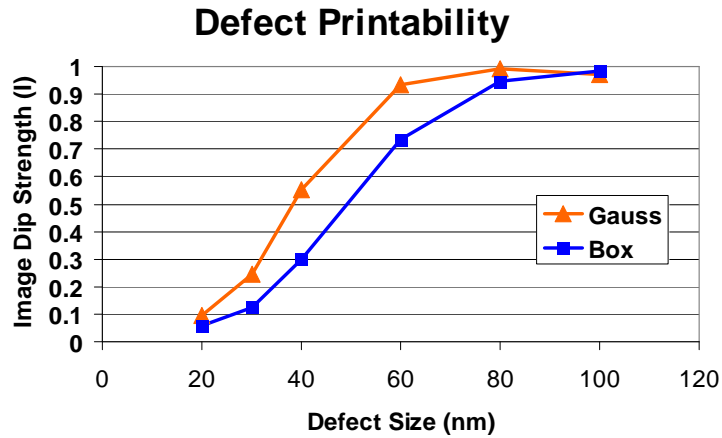
Figure 6.5. Plot of image dip strengths for 2D line Gaussian and Box defects. Gaussian defects can print almost 2X worse than box defects in a worst case.

defects for their respective sizes. Prior to this study, it was assumed that box defects would have a greater impact than Gaussian defects because their topography would allow greater angular scattering from steep sidewalls and corners, relative to the smooth Gaussian shape. The reason for this discrepancy cannot be explained by a volume argument, since Gaussian defects only have about 6% more volume than a similar sized box defect. The discrepancy can be understood by investigating the smoothing process for multilayer deposition. The smoothing process is very effective at smoothing away defects due to its angular dependent etch that efficiently smoothes away very steep surfaces, and hence, the box defect is dramatically smoothed. When the smoothing process is applied to a Gaussian defect, the tails of the Gaussian shape have a very gradual slope and are left in tact by the angular dependent etch. These two tails form a low lying base that the angular dependent etch cannot efficiently smooth away, serving to entrench the Gaussian defect. This entrenchment allows the Gaussian defect to have a greater physical presence in the higher layers, generating worse scattering than the box

116
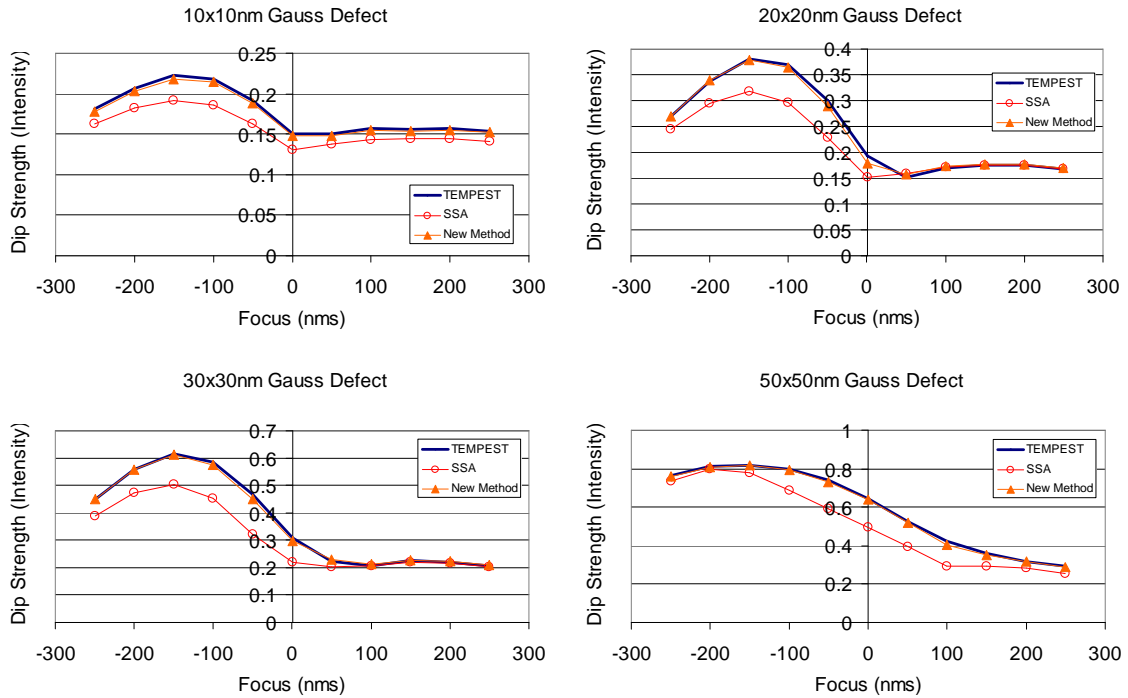
Figure 6.6. Dip strengths through focus for a 10x10nm , 20x20nm , 30x30nm , and 50x50nm Gaussian defect. The dark line is the TEMPEST results, the triangles are the new method results, and the circles are the SSA method results. Notice the new method nearly overlays the TEMPEST results.

defects. With this knowledge, substrate defects should be made as compact as possible prior to deposition, so that the advantages of the smoothing process can be maximized.

To better show the focal behavior of defects simulated with the new method, the dip strengths for through focus images of 10x10nm, 20x20nm, 30x30nm, and 50x50nm Gaussian defects are shown in Figure 6.6. Notice that for every sized defect, the newly proposed methodology nearly overlays the FDTD results. The SSA method does remarkably well at predicting the impact of a defect, and gives a good indication of the defect behavior, but is not sufficiently accurate to facilitate quantitative studies in this regime. In these curves, familiar behavior is shown that phase defects will print worse in one out of focus direction vs. the other [24,69]. These images indicate that results as accurate as FDTD simulations are achievable for smoothed defects.

6.3 Accuracy of 3D Defect Simulations

The ray-tracing method has been shown to be accurate across all defect sizes tested, as well as the two shape extremes for the 2D line defects in this study. The same study can now be rerun using 3D defects, providing useful defect tolerances for understanding defect printability in real EUV mask blanks. The 3D results show all the same trends as the 2D results, and in an effort to avoid redundancy, will not be explained as thoroughly as the 2D section.

The in focus image dip strengths of 3D box defects are shown in Figure 6.7a. Once again, we see that the SSA method is under predicting the image dip strength compared to the ray-tracing method. It is important to note that only two TEMPEST simulations were run to verify the accuracy of the 3D ray-tracing and SSA calculations, due to the incredible complexity of simulating such structures with FDTD. A single TEMPEST point in Figure 6.7 took 46.5 hours to simulate on 8 processors at 500MHz, and used 7.6 Gbs of shared memory. The two TEMPEST points do agree with the ray tracing calculation, and from extrapolation from the 2D results, we can infer that the ray-tracing method is producing results that agree well with general 3D FDTD results. Figure 6.7b and 6.7c shows the image dip strengths of the 3D box defects at ±150nms (±2 RU). Figure 6.7d shows the through focus dip strengths from a 90nm box defect. The 3D results are similar to the 2D results for box defects. The simple threshold model for defect printability shows that 3D box defects do not print if smaller than about 90nms, whereas this tolerance drops to about 50nms if tight focus controls cannot be implemented.
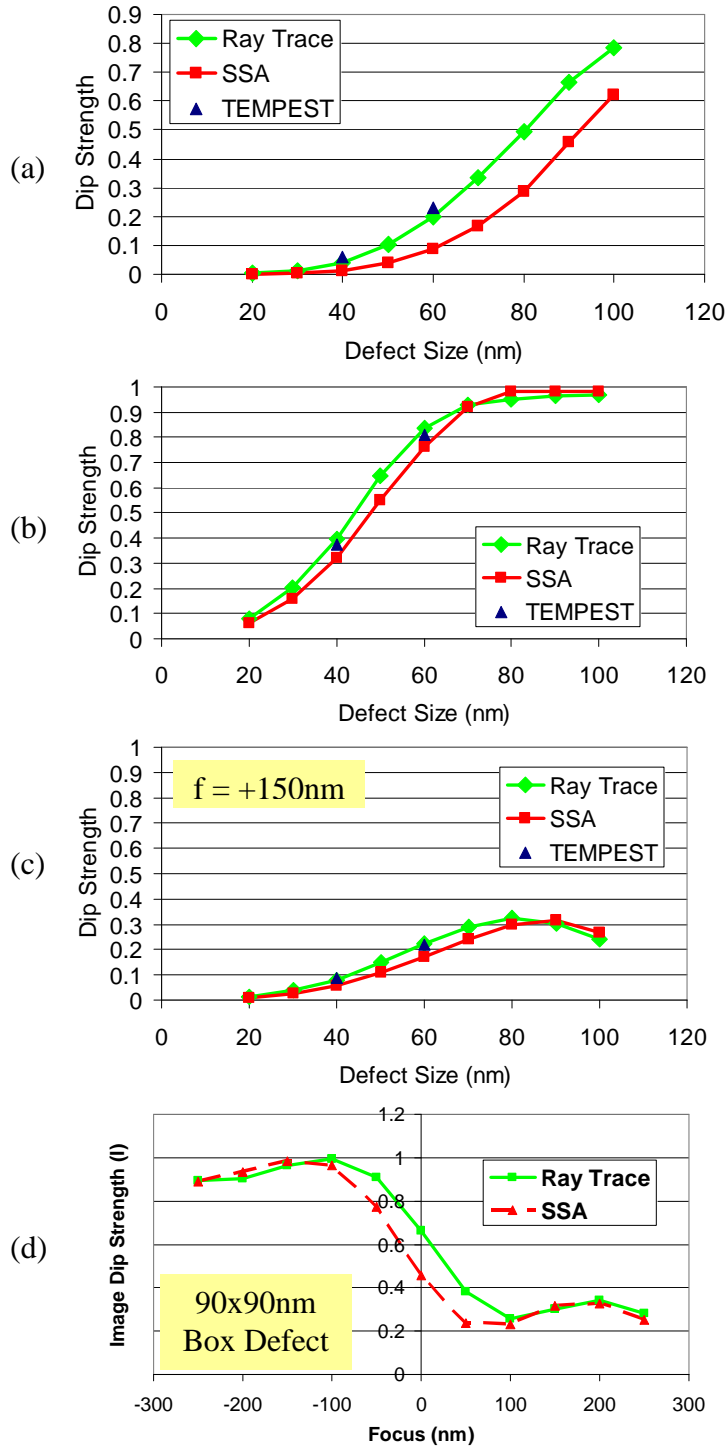
Figure 6.7. (a) Plot of the image dip strengths at best focus. (b) Plot of the image dip strengths at -150nm focus. (c) Plot of the image dip strengths at +150nm focus. (d) Plot of the image dip strengths for a 90x90nm box defect through focus.

3D Gaussian Defect Printability
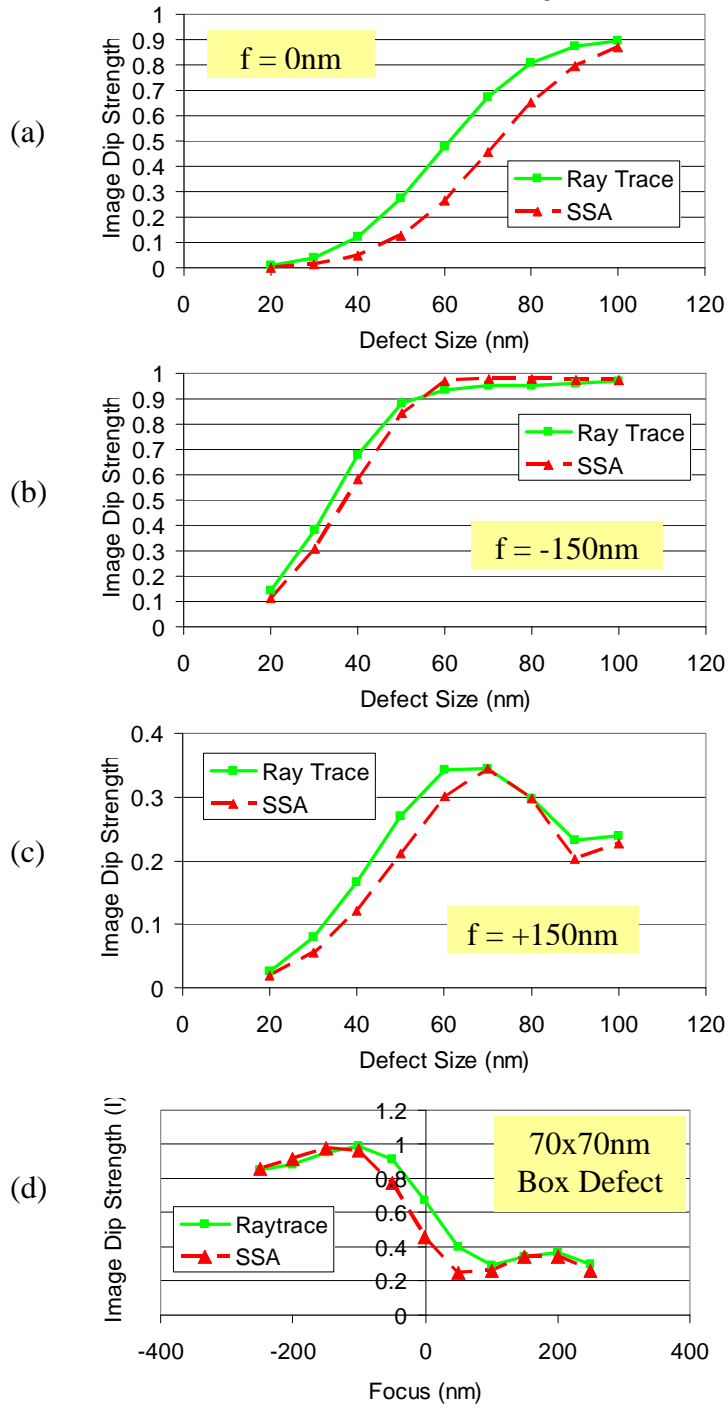
Figure 6.8. (a) Plot of the image dip strengths at best focus. (b) Plot of the image dip strengths at -150nm focus. (c) Plot of the image dip strengths at +150nm focus. (d) Plot of the image dip strengths for a 90x90nm box defect through focus.

Defect Type	2D			3D		
	f = -2RU	f = 0	f = 2RU	f = -2RU	f = 0	f = 2RU
Box	<30nm	<60nm	<100+nm	<50nm	<90nm	<100+nm
Gaussian	<25nm	<45nm	<90nm	<40nm	<70nm	<100+nm

Table 6.1. Shows defect tolerances for 2D and 3D buried defects for Gaussian and box defects.

Figure 6.8a shows the in focus image dip strengths of 3D Gaussian defects, while Figure 6.8b and 6.8c shows the image dip strengths for 3D Gaussian defects at ±150nms (±2 RU). Similar analysis to that above shows that 3D Gaussian defects become printable when they are greater than about 70nms, while this tolerance drops to 40nms if tight focus controls cannot be implemented. Table 6.1 shows the complete size tolerances for 2D and 3D buried defects when imaged in the clear field. Negative focus values are colored red for poor imaging conditions, in focus values are colored yellow for decent imaging conditions, and positive focus values are colored green for good imaging conditions.

Similar to the 2D results, Figure 6.9 shows that 3D Gaussian defects have a
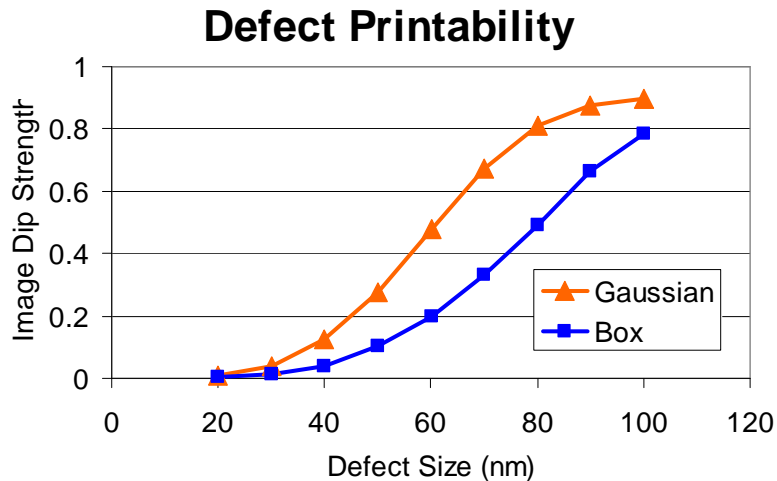
Figure 6.9. Shows 3D Gaussian defects print worse than 3D box defects.

greater imaging impact than 3D box defects. Some 3D Gaussian defects can be as much as 2.5X worse than similarly sized box defects. A careful study of Figure 6.9 and Figure 6.5 shows that 3D Gaussians differ from 3D boxes more so than 2D line Gaussians differ from 2D line box defects. This can once again be explained by the entrenchment of the Gaussian defect by the Gaussian tails. In 3D, however, this entrenchment is facilitated on all sides of the Gaussian defect, enabling the 3D Gaussians to differ even more from 3D box defects than their 2D counterparts.

6.4 Analysis of Multilayer Scattering

The end of the previous section demonstrated that subtleties in the deposition process used to coat substrate defects can greatly impact the printability of these defects. This section is therefore interested in understanding how the reflected spectrum is impacted by the spectral composition of the multilayer itself. A simple analysis of the

Figure 6.10. (a) The first layer is the Gaussian or box defect, whose Fourier transform is either a Gaussian or sinc function. (b) The top layer of the multilayer resembles an exponentially decaying function on both sides, whose Fourier transform plotted on a log scale looks like a triangular decaying structure.

multilayer stack provides some interesting insight. The Fourier transform of the two

substrate defect shapes provides us with either a sinc (for a box defect) or Gaussian (for a

Gaussian defect) function, as shown in Figure 6.10a. The top layer of the multilayer

stack is shown in Figure 6.10b, and resembles the function:

$$g(x) = \exp[-|x-a|]$$

whose Fourier transform, plotted on a log scale, resembles a decaying triangular function.

Since the total reflection from the multilayer is a combination of reflections from the

individual layers within the multilayer, the final reflected spectrum should be a weighted

combination of the original defect spectrum (sinc or Gaussian) and the decaying

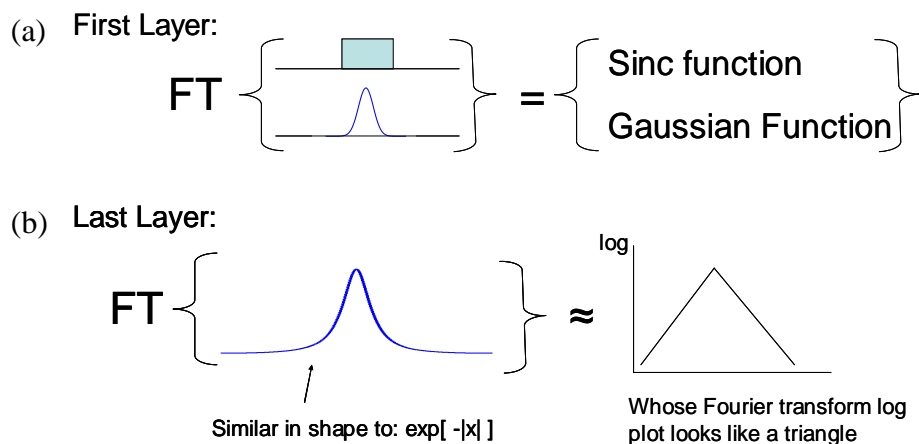triangular function of the top layer of the multilayer.

This implication is confirmed in Figure 6.11 which compares the multilayer

spectrums of a small 20x20nm box defect and a large 100x100nm box defect. The

original sinc function of the box defect can clearly be seen at the top of the graphs. For all

the layers above the defect, the rapid degradation of the high frequencies can be

observed, until the final top layer is reached. Notice that the top layer does indeed

resemble this triangular decaying structure seen in Figure 6.10b. The multilayer spectrum

of the small box defect contains very little modulation since the small box defect

produces a very broad sinc function. The final reflected spectrum should be a weighted

combination of these flat and smooth functions, which is exactly what is shown in Figure

6.11a. This reflected spectrum can be directly contrasted to the reflected spectrum of the

large box defect in 6.11b. The large box defect produces a more compact sinc function

that is highly modulated. The growth of the upper layers decays this modulation away,

until it reaches a more flat, triangular function, however, we see that the final reflected
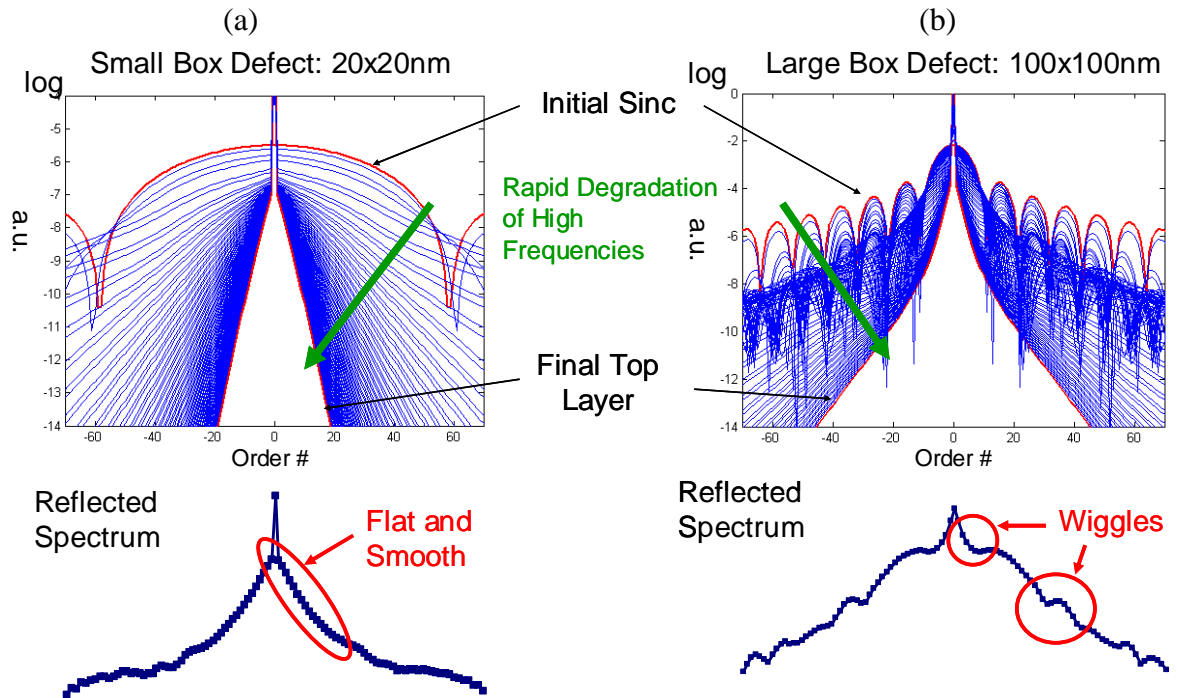
Figure 6.11. (a) A small box defect has smooth spectral properties within the multilayer, leading to a reflected spectrum that is smooth as well. (b) A large box defect has more modulated spectral properties within the multilayer, leading to a more modulated reflected spectrum.

spectrum does indeed show the modulation coming from the more compact sinc function.

This observation shows that the incident wave front is penetrating deep below the top

surface of the multilayer, since the spectral characteristics of the bottom layers can be

seen in the final reflection. Since the SSA method only uses information from the top

surface to compute the reflection, it cannot fully account for the total reflection seen, and

is precisely why the ray-tracing method provides a more accurate picture of defect

printability. However, due to the decay experienced by EM waves entering the

multilayer, the lower layers provide a smaller contribution of the total reflection

compared to the top layers, enabling the SSA method to provide a general idea of defect

printability despite its limited use of information.

6.5 Comparison of Computational Resources

The new ray-tracing method has been shown to be as accurate as FDTD simulations for both 2D and 3D defects. The great advantage of the ray-tracing method over FDTD can now be seen in the speed and memory improvements that the method provides. First, the ray-tracing method has a grid-less z-direction, having only 1 point per layer (2 per bilayer) in the z-direction. A typical discretization for TEMPEST would have about 10 points per bilayer, reducing the number of cells required to describe the physical mirror geometry by about 5X. Second, the ray-tracing method only tracks the complex electric field, and not the full 6 components of the real electric and magnetic fields that TEMPEST tracks, giving a reduction of about 3X in field components. Most importantly, the NA and sigma of the optical system gives a maximum spatial frequency that is collected by the imaging system. It is only these Through The Lens (TTL) frequencies that must be computed accurately. The maximum spatial frequency (f_{system}) that needs to be resolved by the optical system, allows a Nyquist frequency to be determined:

$$f_{Nyquist} = 2 f_{system}$$

The Nyquist frequency can now give a discretization requirement for the ray-tracing method such that it will still compute an accurate result. Since the small NA of the EUV systems gives a relatively small spatial frequency that must be resolved, the resultant required discretization for the ray-tracing method can be very large. As an example, assume a 2D domain is 1035nms wide. For an NA=0.3 and σ =1.0 optical system, only the first ±11 frequencies will enter the optical system. The Nyquist frequency tells us that

we will need to calculate the first ±22 frequencies, giving a total of 45 frequencies (including the 0th order). This means that our ray-tracing discretization, dx, can be:

$$dx = \frac{1035nm}{45} \sim 23nm$$

Thus, the ray-tracing method only needs to sample the domain every 20nms and it can still calculate an accurate result. This discretization may seem very surprising since it is about 50% greater than the wavelength of the system! Remembering that the multilayers are optically smooth and contain no vertical edges or corners, helps to understand why the discretization can be so large, as well as the small NA of the system. The ability to use such large discretizations enables the ray-tracing method to have huge speedups
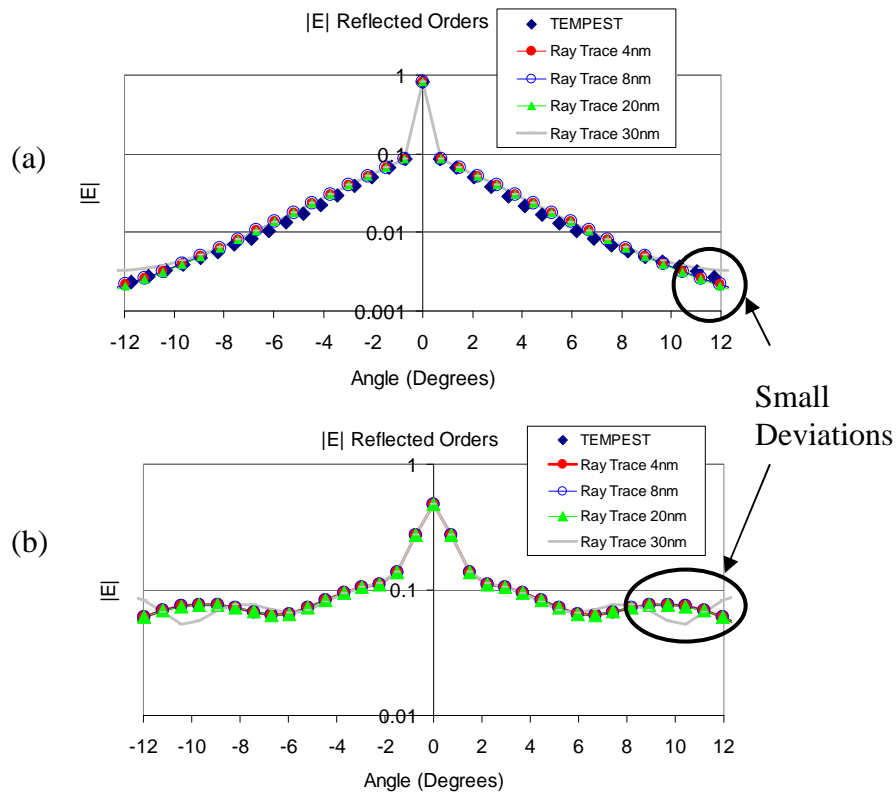
Figure 6.12. (a) Magnitude of the spectrum of a small 20x20nm Gaussian defect at various ray-tracing samples. (b) Magnitude of the spectrum of a large 100x100nm Gaussian defect at various ray-tracing samples.

relative to TEMPEST, which typically has discretizations on the order of 0.35-0.7nms for

EUV simulations.

Figure 6.12 verifies that this 20nm discretization can be used and still obtain the

same results as FDTD, regardless of defect size. Figure 6.12a shows the magnitude of the

reflected spectrum of a small 20x20nm Gaussian defect for various levels of

discretization. Notice that all ray-tracing simulations give the same results until the

discretization rises above the 20nm limit. At a 30nm discretization, small deviations can

begin to be seen. The same results apply to Figure 6.12b where the defect is now a large

100x100nms.

Table 6.2 provides speed statistics from two typical defect cases (one 2D and one

3D) that were run with TEMPEST and the ray-tracing method. The "speedup factor" is

defined as the TEMPEST runtime divided by the runtime of the method, and the

"memory reduction factor" is defined as the TEMPEST memory divided by the memory

of the method. For TEMPEST, these ratios are simply 1. TEMPEST took almost 3,300

seconds and 94.1Mb to run the 2D buried defect simulation on a 3.2 GHz processor. The

Case	Total Runtime	Speedup Factor	Main Memory	Memory Reduction Factor
Tempest (2D)	3,268s	1	94.1Mb	1
Ray Trace (2D) (20nm Res)	0.14s	23,300	1.88 Mb	50
Tempest (3D)	46.5h	1	7,600 Mb	1
Ray Trace (3D) (20nm Res)	1.61s	100,000	171.5 Mb	44

Table 6.2. Computational resource table. Comparison of FDTD (TEMPEST) and the new ray tracing method

Total Runtime: % Allocation
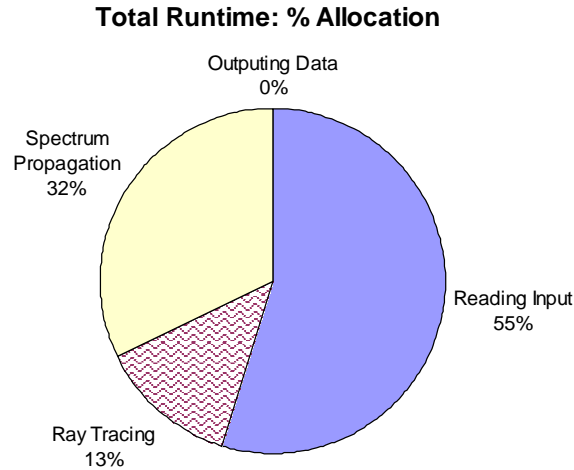
Figure 6.13. Percentage of total time spent on various duties for the 3D ray tracing example.

newly proposed method had a total runtime of 0.14 seconds and used 1.88Mb of memory

on a 3.2Ghz processor when the incident wave front was sampled every 20nm (maximum

discretization allowed). The 2D ray-tracing results have a speedup of nearly 23,000X

relative to TEMPEST, and a memory reduction factor of about 50X. To emphasize just

how much quicker the ray-tracing method is, relative to FDTD, we recall the 3D

TEMPEST result from the defect landscape that took 46.5 hours to run and 7.6 Gbs of

memory. Using the ray-tracing approach, the 3D results took only 1.61 seconds (a

speedup of about 100,000X) and used only 171.5Mb of memory (a memory reduction of

about 44X). It is also noted that further optimizations to the code could produce

additional gains in its speed and memory use. While the speed gains of the new method

are quite impressive, the memory reduction is even more important because FDTD

simulations are limited to about 2Gbs on 32-bit architecture non-parallel systems due to

addressable memory constraints and operating system allocation of memory. This new

method allows much larger 3D simulations to be accomplished on desktop computers. Of

final note, Figure 6.13 shows a breakdown of where the ray tracing program spent most

of its time for the largest 3D case. Only 13% of the runtime was spent tracing the rays

into the multilayer stack, while 32% of the time was spent Fourier transforming and

propagating the spectrum of the scattered fields outside of the stack. A large portion of

the runtime, about 55%, was spent loading in the multilayer file for the locations of the

interfaces. The multilayer file also accounted for a staggering 168Mb of the memory

used, or about 98% of the total memory costs! All the multilayer interface files were

stored with sub-nm resolution (0.69nm), to obtain the most accurate representation of the

multilayer possible. However, with 55% of the time spent reading in the multilayer data,

and 98% of the memory coming from the multilayer data, great gains could be

accomplished by simply using fewer samples in the multilayer file. If the multilayer was

sampled every couple nms instead of every 0.69nms, the memory could be further

reduced by a factor of over 8, and achieve an additional speedup of about 2.

6.6 Analysis of FDTD Results

The accuracy results from the new method have been shown to be very similar to

what FDTD produces across a broad variety of shapes and sizes. One must look very

carefully to uncover the small differences that can be found, and understand which

approximations might cause such small deviations. A careful investigation of FDTD has

led to some surprising results regarding its ability to calculate accurate results due to the

resonant nature of the multilayer. Figure 6.14a shows the analytic reflection from a

perfect multilayer structure as a function of incident angle, as well as the FDTD

predictions of the reflection. Clearly the FDTD method has significant errors in its
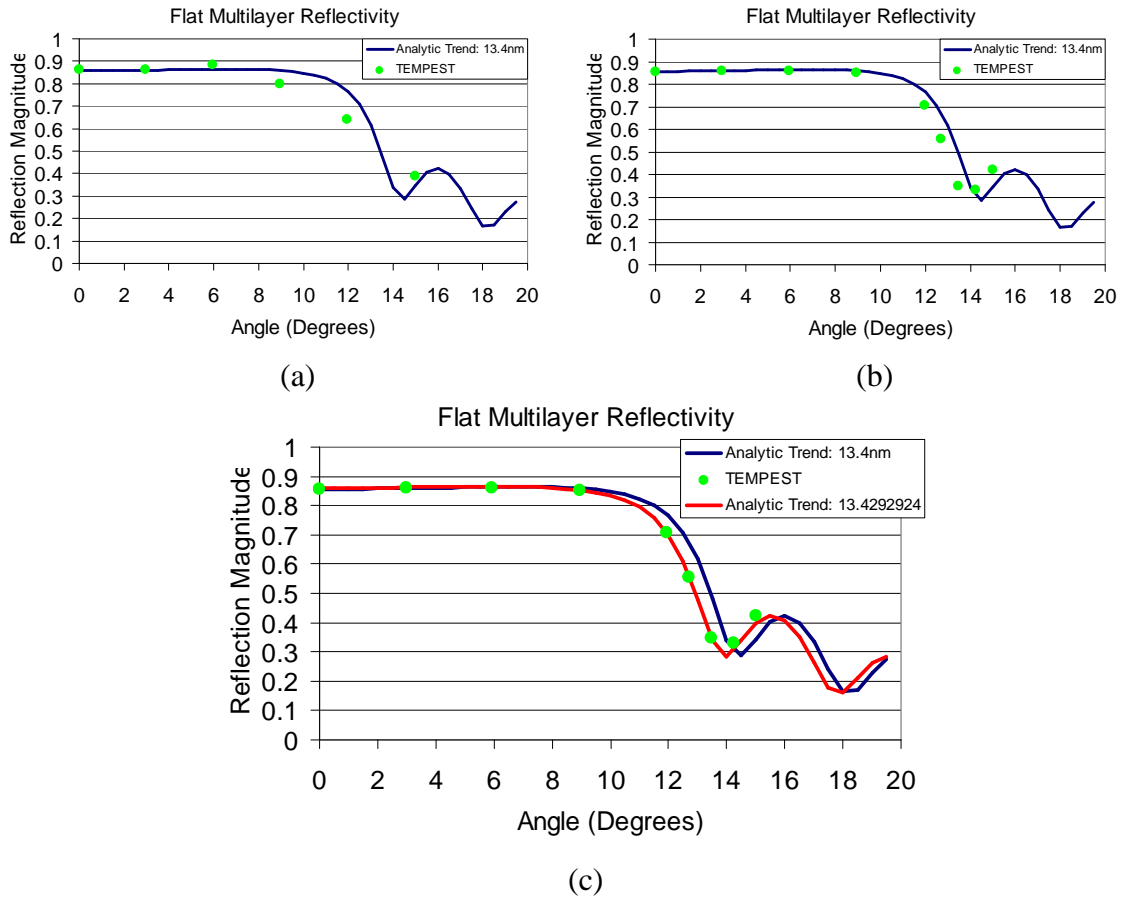
Figure 6.14. Reflectivity from a flat mirror as a function of angle (a) with temporary lull in convergence. (b) with fully converged fields. (c) with fully converged fields and analytic solution for numerical dispersion wavelength.

answer compared to the analytic solution. FDTD should produce much better results than these simulations predict, so what went wrong? To answer this, the 12° incident angle simulation was rerun again and the reflected field was outputted over many wave cycles (over 500 cycles). The results are plotted in Figure 6.15, and can be split into three regions. In the first region, the reflected field ramps up very quickly within 25 cycles. Interestingly, the distance from the excitation plane to the bottom of the mask is about 25λ, meaning that as the initial incident wave finally exits the bottom of the structure, the initial reflections from almost half the layers in the stack will have reached the measured
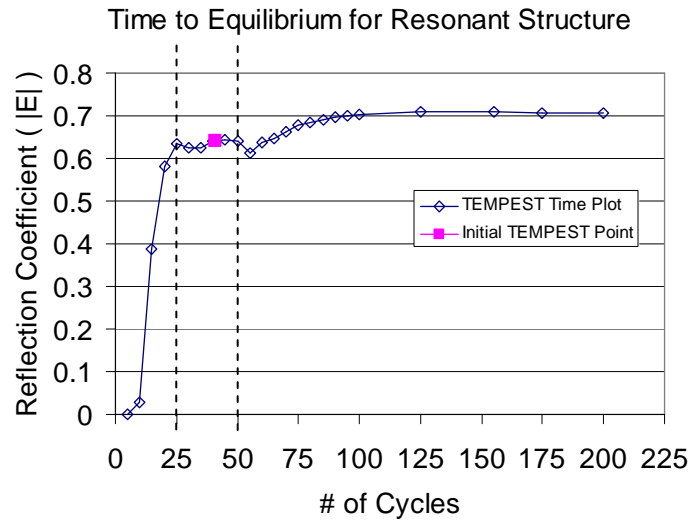
Figure 6.15. Reflection coefficient from a flat mirror at 12º incidence as a function of the number of wave cycles simulated. The reflection is spit into 3 regions: (1) High reflection ramp, (2) gathering coherence, (3) final convergence.

reflection plane. This is in good agreement with Figure 5.16 which shows that the first half of the multilayer is responsible for about 90% of the total reflected field.

In the second region, the reflected fields seem to converge to a steady value and the convergence criterion in TEMPEST is tricked into outputting the fields after 41 cycles. This region is a temporary convergence lull however, and is likely due to the movement of energy within the stack. Within the resonant structure, the reflected waves must bounce around a significant number of times. During this time period, the reflected fields inside the cavity are likely gathering coherence among all the other reflected waves, and very little energy is actually allowed to escape. After another 25 cycles, the third region is reached, where the energy begins to leak out of the structure and slowly build towards a truly converged solution. The final reflected field value is not fully reached until about 120 cycles. This implies that TEMPEST simulations might need to be run about 3 times longer than they have been run previously, in order to avoid a false convergence of the fields.

Figure 6.14a can be regenerated by allowing sufficient time for the FDTD simulations to properly converge to their final values, and the data is plotted in Figure 6.14b. The fields are certainly in better agreement with the analytic solution, but still contain quite a few errors along the falling edge of plot. This regime is where the incident angle of the wave no longer allows itself to coherently interact with the other layers of stack, resulting in reduced reflectivity. The Bragg condition is effectively no longer met. To understand where these differences come from, we need to understand numerical dispersion.

All FDTD simulators contain numerical dispersion [70], which comes from the nature of their finite differences. The finite difference approximation to a real derivative makes an error when trying to correctly compute the wave number k. The wave number error is normally very small, and scales based on the cell density [8]:

$$k_{error} = \frac{\pi^2}{3d^2}$$

Where d is the number of cells per wavelength. The simulations were run with d=38.84, so the estimated wave number error is k_{error}=0.002181. This error will produce a relative error in the simulated wavelength of:

$$\frac{\lambda_{error}}{\lambda_0} = 1.002186$$

So the simulated wavelength will be changed by about 0.2%. This wavelength change normally might only produce a few degree change in the wave propagation for DUV structures [71] , however, the resonant nature of the EUV multilayer and the long propagation distances involved, make the multilayer hyper-sensitive to small wavelength changes. The analytic reflection can be recomputed for the same multilayer at the new

wavelength based on the numerical dispersion estimate, and plot the results in Figure 6.14c. Incredibly, using the first order estimate for numerical dispersion to modify the wavelength gives excellent agreement with the TEMPEST results.

Figure 6.14c clearly shows that FDTD results can no longer be adequately trusted when the angle of propagation goes beyond 10º, where the multilayer transitions to a non-resonant structure. Past this angle, the FDTD and analytic solutions provide vastly different reflection computations due to numerical dispersion. The ray tracing spectrum and the FDTD spectrum for the example defect seen in Figure 6.1c, can be reanalyzed. The differences in their calculated spectrums become significant past about 10º, where there is a significant drop in the spectrum magnitudes before peaking again at about 17º. The significant drop and corresponding peak at 17º are very similar to the behavior seen in Figure 6.14c where the structure transitions to non-resonance. The fact that the major differences occur at greater than 10º, and are followed by a quick peak around 17º is clearly suggestive that numerical dispersion plays a role in the different results observed. These differences will affect the final image since EUV systems are telecentric about 6º, where a σ=0.3 system would collect angles between about 0º-12º. Larger σ's would result in higher collected angles and if future EUV systems have larger NAs, these differences may become more important. Numerical dispersion is a complicated phenomenon, since it also depends on the angle of propagation. Small phase changes in the propagation due to numerical dispersion will be amplified inside the resonant structure as the waves travel multiple wavelengths, so the final results will be impacted across all diffracted orders. Numerical dispersion is likely a major contributor to the observed error between FDTD and the ray tracing method.

6.7 Conclusions

The new ray-tracing method was shown to accurately and rapidly simulate buried defect printability across a wide variety of 2D and 3D defects coated with the smoothing process for EUVL multilayers. The method can produce results as accurate as FDTD, but up to 100,000X faster and with about 40-50X less memory required. To emphasize how large of a time reduction this represents, a single 3D FDTD data point took 46.5 hours on 8 processors at 500MHz, while the ray tracing simulator obtained the results in 1.61 seconds on a 3.2GHz processor. The ray-tracing approach allows a sampling reduction of about 10X in the z-direction, and more than a 10X reduction in both the x and y-directions, allowing the simulator to be up to 5 orders of magnitude faster than FDTD. It was also shown that the multilayer file represented about 98% of the memory used in the new method, and took 55% of the runtime just to read the file in. Additional lowering of the computational resources could be accomplished by using larger discretizations within the multilayer file.

Simulation results show that subtleties in the deposition process can greatly impact a defect's printability, causing smooth Gaussian defects to print worse than box defects due to an entrenchment effect during the smoothing process. As such, substrate defects should be made as compact as possible prior to deposition with the smoothing process, in order to achieve the best results. Defect printability guidelines for 2D and 3D defects were established. It was shown that 2D line defects are sub-printable below 45nms, while 3D defects are sub-printable below 70nms. Due to the phase behavior of

buried defects, these tolerances fall to 25nms in 2D and 40nms in 3D when -2 RU of defocus is applied. Reflected spectra show that the bottom layers of the multilayer do impact the final reflected spectrum, and show that it is necessary to use information from all layers to accurately compute the final reflected fields. The SSA approach was shown to underestimate defect printability at various focal regions for many defects of interest.

A surprising result was uncovered when carefully analyzing the accuracy of FDTD. The resonant nature of the multilayer can cause a temporary convergence lull to be determined, since the energy bounces around inside the resonant structure until it gathers coherence and is able to leak energy out. To avoid this convergence lull, FDTD might have to be run up to 3X longer than normal in order to assure convergence. Numerical dispersion was also shown to have a large impact on the observed scattering from FDTD. Specifically, the numerical dispersion causes a small change in the simulated wavelength which becomes noticeable when it interacts with the resonant multilayer. The multilayer is hyper-sensitive to small wavelength changes on the edge of resonance where the Bragg condition begins to fail. Numerical dispersion within FDTD can be reduced by increasing the cell density, which increases the memory requirements dramatically. Therefore, simulating buried defects accurately with FDTD would require even more memory and require even more time (to avoid convergence lulls) when computational constraints are already significantly limiting FDTD's application.

7   EUV Buried Defect Landscape Maps

This Chapter will demonstrate three applications of the new simulation methodology for scattering from non-planar buried defects as well as provide guidelines for defect requirements for mask blank tolerances. First, detailed investigations of the performance of the new simulator when applying off-axis illumination will be performed. Second, the method's performance will be tested on defects coated with a standard deposition process, which produces very low smoothing for the substrate defects. Thirdly, printability tests for defects deposited during the smoothing deposition process will be performed such as allowing defects to appear between layers inside the multilayer. These types of defects can appear from particles falling onto a partially coated multilayer structure during deposition, and can have significantly greater printability impacts since there are fewer bilayers on top of the defect to smooth its presence. The goal of these investigations is to characterize the robustness and speed for the many current defect concerns as well future deposition techniques.

Finally, the chapter will explore isolated defect printability requirements for mask blank tolerances. The defect printability maps will be generated for both the standard and smoothing deposition processes, both 2D and 3D structures, as well as Gaussian and box type defects. For each of these cases, a wide range of aspect ratios will be tested to better

understand defect parameters that most influence printability. These tolerances will give a greater understanding of defect printability for a host of defect situations.

7.1 Off – Axis Illumination

The impact of off-axis illumination will likely need to be modeled for EUVL since the multilayer mirror is a sensitive function of the angle of incidence. Most imaging programs assume constant scattering regardless of the angle of incidence on the mask, allowing a single near field simulation to be used as a template for scattering from all angles coming from the partial coherence. Pistor [23] showed that this approximation works very well for angles <10º when using FDTD to simulate DUV masks. This approximation, however, cannot be justified when simulating EUV masks, as seen in Figure 7.1 which shows the analytic sensitivity of the multilayer stack to off-axis illumination. For instance, an NA=0.35 system, operating at 4X reduction with $\sigma = 0.3$ will collect a solid angular cone of about 13º, which will nominally be centered about 6.5º off-axis. This range implies that the optical system will collect from about 0º-13º,
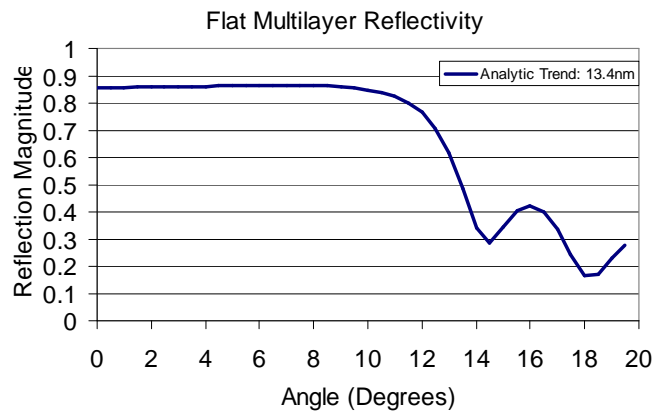

Figure 7.1. Analytic reflection magnitude of a perfect multilayer as a function of angle of incidence.

137

where the tail end of this range will dip into the region where the structure transitions out of being a Bragg reflector. Also, if dipole illumination or other illumination setting which emphasizes off axis waves is used to print features, then the edges of the angular range will be used, and more accurate simulations of the reflectivity will be needed. The ability to simulate multiple angles of incidence will thus allow even better predictions of defect printability under partial coherence.

Multiple simulations at off-axis angles will likely be needed for accurate simulations of EUV masks. Multiple FDTD simulations are feasible, but highly impractical as Chapter 6 showed that the computational resources required to run a single simulation are already significantly challenging in 3D. The SSA assumes a normally incident plane wave onto the multilayer structure, and thus provides no information on how the printability of a defect differs at various angles of incidence. The ray-tracing methodology is therefore a very good candidate to explore multiple off-axis simulations as long as its accuracy holds for various angles of incidence.

The accuracy of the ray-tracing simulation methodology was tested for various angles of incidence and compared to the SSA and FDTD methods for both a large (60x60nm) and small (30x30nm) 2D line Gaussian defect. Each defect was simulated at a few off-axis angles, and the reflected spectrums were shifted to place the main order at the normal incidence position. Shifting the spectrum actually mimics an imaging system that is telecentric about the incident off-axis angle so that the images could be properly investigated without energy loss from the main order scattering outside of the pupil. An NA = 0.3 and partial coherence of $\sigma = 0.3$ was assumed, and the constant scattering approximation was also used.

Off – Axis Illumination: 60x60nm 2D Gaussian Defect
Smoothing Deposition

(a)

f = 0nm

(b)

f = -150nm

(c)
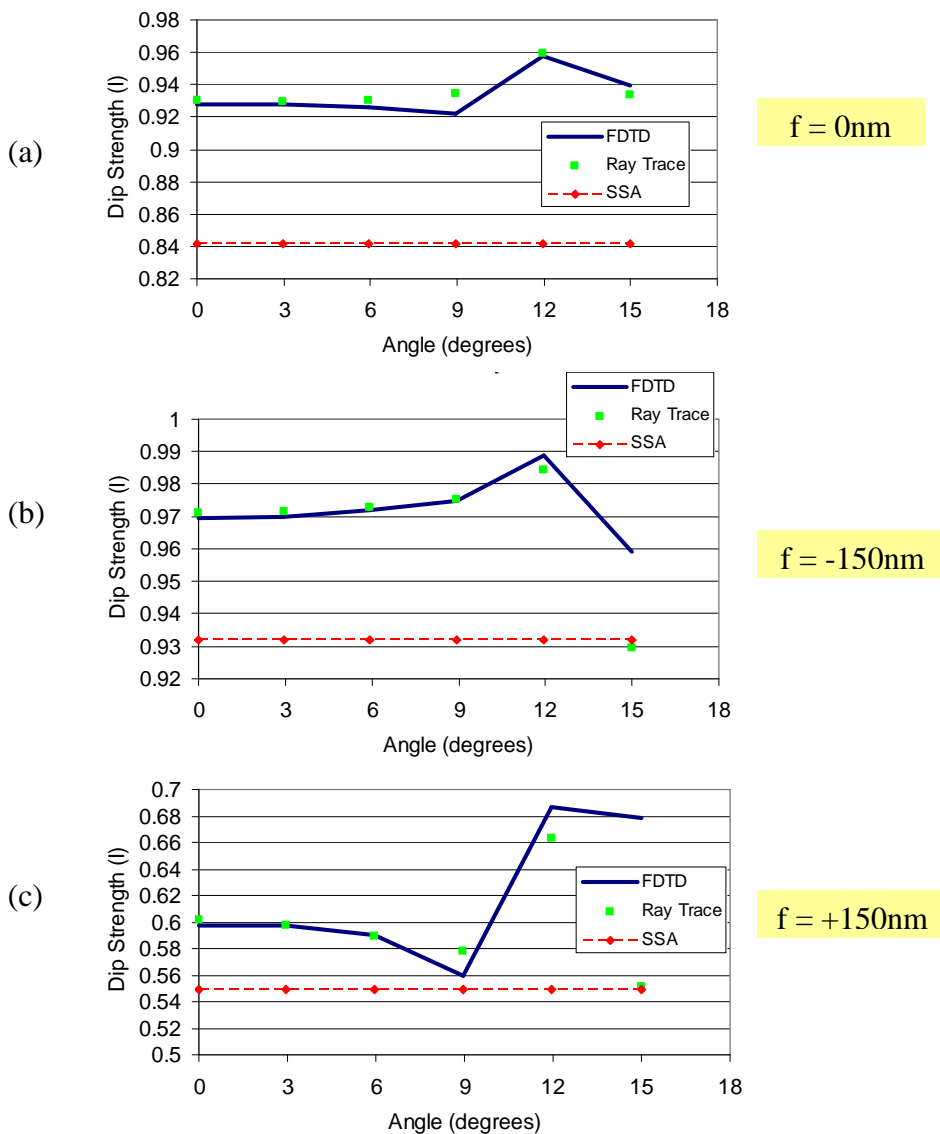
f = +150nm

Figure 7.2. Plot of the image dip strengths for a 2D line 60x60nm defect coated with the smoothing process as a function of illumination angle: (a) best focus. (b) -150nm focus. (c) +150nm focus.

The dip strength, given by Equation 6.1, is plotted as a function of the angle of incidence in Figure 7.2 for focus values of -2 RU, 0 RU, and +2 RU for a 60x60nm 2D line Gaussian defect. The ±2 RU positions were chosen based off of the plots in Figures 6.3d, 6.4d, and 6.5 which show that the peak signal for smoothed defects generally occurs
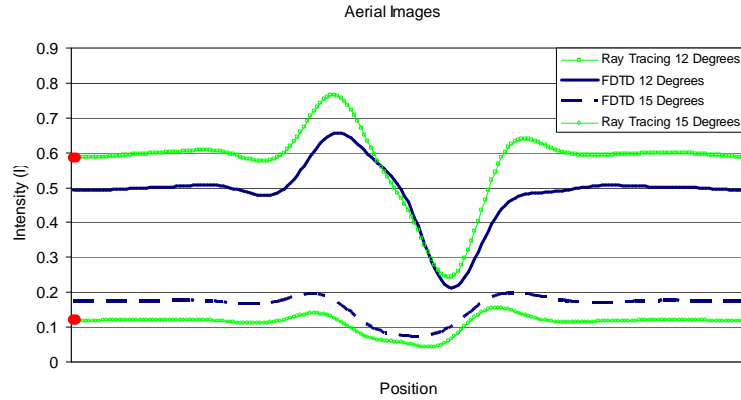
Figure 7.3. Analytic reflection magnitude of a perfect multilayer as a function of angle of incidence showing that the ray tracing method picks up the defect intensity shape while not suffering the inaccuracy of a level shift of FDTD due to numerical dispersion.

at about -2 RU. Clearly the FDTD results in Figure 7.2 change as the angle of incidence is increased. The ray tracing method tracks these small changes fairly well below 6º angle of incidence, but starts to differ from the FDTD results at higher angles. These differences largely stem from the differences in the background level that FDTD predicts at angles greater than about 9º due to the numerical dispersion inherent to the method, as shown in Chapter 6. Figure 7.3 shows a plot of the full images at angles greater than 9º, showing that FDTD is predicting significantly different background results from the ray tracing method despite showing the shape of the curves are similar. For comparison, the analytic background values for 12º and 15º are plotted in big circles on the left hand side of Figure 7.3. Notice that the ray tracing method predicts the correct background value while the FDTD results are off. This background intensity difference influences the dip strength metric, especially when the value of the background is significantly reduced from losing the Bragg coherence at angles greater than 9º. Because of this background level offset, the ray tracing results are believed to be more accurate than the FDTD results for angles greater than 9º.

140

For a smaller defect (30x30 nm 2D line Gaussian defect), the results are similar. Figure 7.4 shows the dip strengths of the small defect plotted as a function of the angle of incidence for focus values of -2 RU, 0 RU, and +2RU. The ray tracing method is again producing results in agreement with FDTD for angles less than 6º, while beginning to

Off – Axis Illumination: 30x30nm 2D Gaussian Defect
Smoothing Deposition
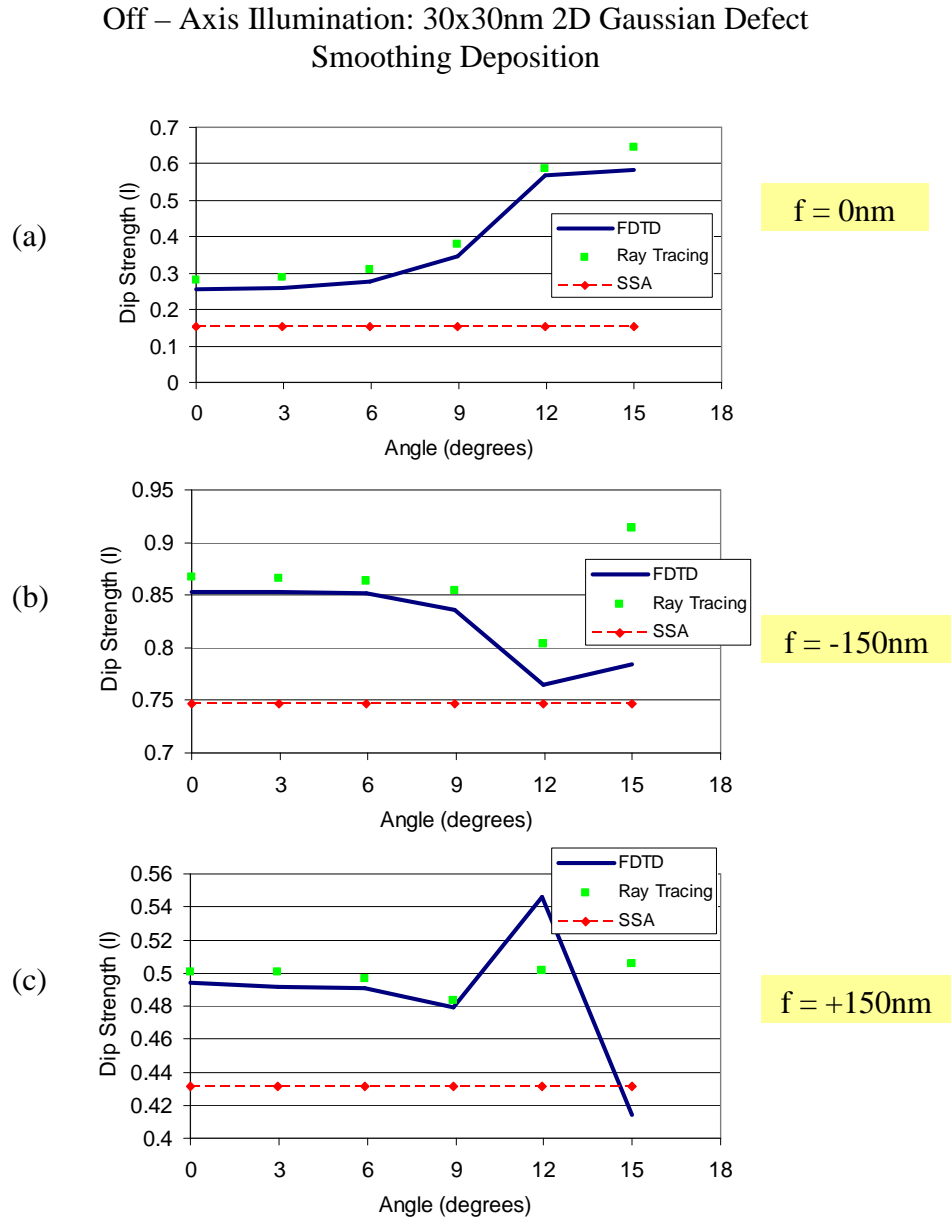

(a) f = 0nm

(b) f = -150nm

(c) f = +150nm

Figure 7.4. Plot of the image dip strengths for a 2D line 30x30nm defect coated with the smoothing process as a function of illumination angle: (a) best focus. (b) -150nm focus. (c) +150nm focus.

diverge at larger angles. The divergence can be similarly shown to stem from the background level differences between FDTD and analytic solutions. The SSA unfortunately cannot capture the dramatic increase in defect printability shown in Figure 7.4a from off axis illumination because it does not include the appropriate information.

These two defect examples show that the ray tracing method is able to accurately model off axis illumination relative to FDTD when the angles are less than 9º. Past 9º, the FDTD method starts giving erroneous background levels which directly impact the dip strength metric, and the results can no longer be trusted. It is expected that the ray tracing results are more accurate than FDTD at these larger angles of incidence. An unfortunate result of the above studies is that buried defects print worse when off axis illumination is used. This result is likely due to a cosine effect for the defect volume since the defect is fairly localized in x and y but propagates a long distance in the z direction. When the plane wave is normally incident, only a small x-y cross section of the plane wave is disturbed by the defect, while an off-axis plane wave will begin to be impacted by the vertical presence in the multilayer, broadening the defects impact. This fact will have a negative impact on EUVL since off-axis illumination schemes, such as dipole or Quasar, are common engineering techniques used to enhance feature printability, but will also enhance the printability of buried defects in EUVL.

7.2 Standard Deposition Techniques

It is important to test the robustness of the ray tracing method to various deposition strategies since EUVL implementation is still significantly far away. In this

time frame, various deposition strategies may be developed to help cope with buried

defect printability and the simulation tool must be able to handle the new techniques.

The ray tracing method was shown in Chapter 6 to be capable of handling defects coated

with the smoothing process, and the method is now tested for defects coated with a

standard deposition process. Since the standard deposition process does not contain an

etching step, defects coated with such a process have significantly more challenging

topographies which result in greater printability. Therefore, much smaller defect sizes

are expected to become printable relative to those found for defects coated with the

smoothing process.

Figure 7.5 shows the image dip strengths for 2D line Gaussian defects coated with

the standard deposition process. FDTD, SSA, and ray tracing results are all plotted. For

all focus values, the ray tracing method is giving excellent results compared to FDTD,

showing that even defects coated with standard deposition techniques can be accurately

simulated with the ray tracing methodology. Notice that significantly smaller defect sizes

are printable (~12.5x12.5nm in focus) relative to defects coated with the smoothing

process when the simple dip strength metric of 0.7 is applied as a printability condition.

The SSA results are actually quite good as well and offer much better results for

these standard coated defects compared to those defects coated with the smoothing

process. This fact makes intuitive sense, since the SSA assumes the top surface is

representative of all the layers inside the multilayer. During standard deposition, the

deposited layers change very little compared to the smoothing process and so the top

layer is expected to be much more representative of the whole structure. Notice, however,

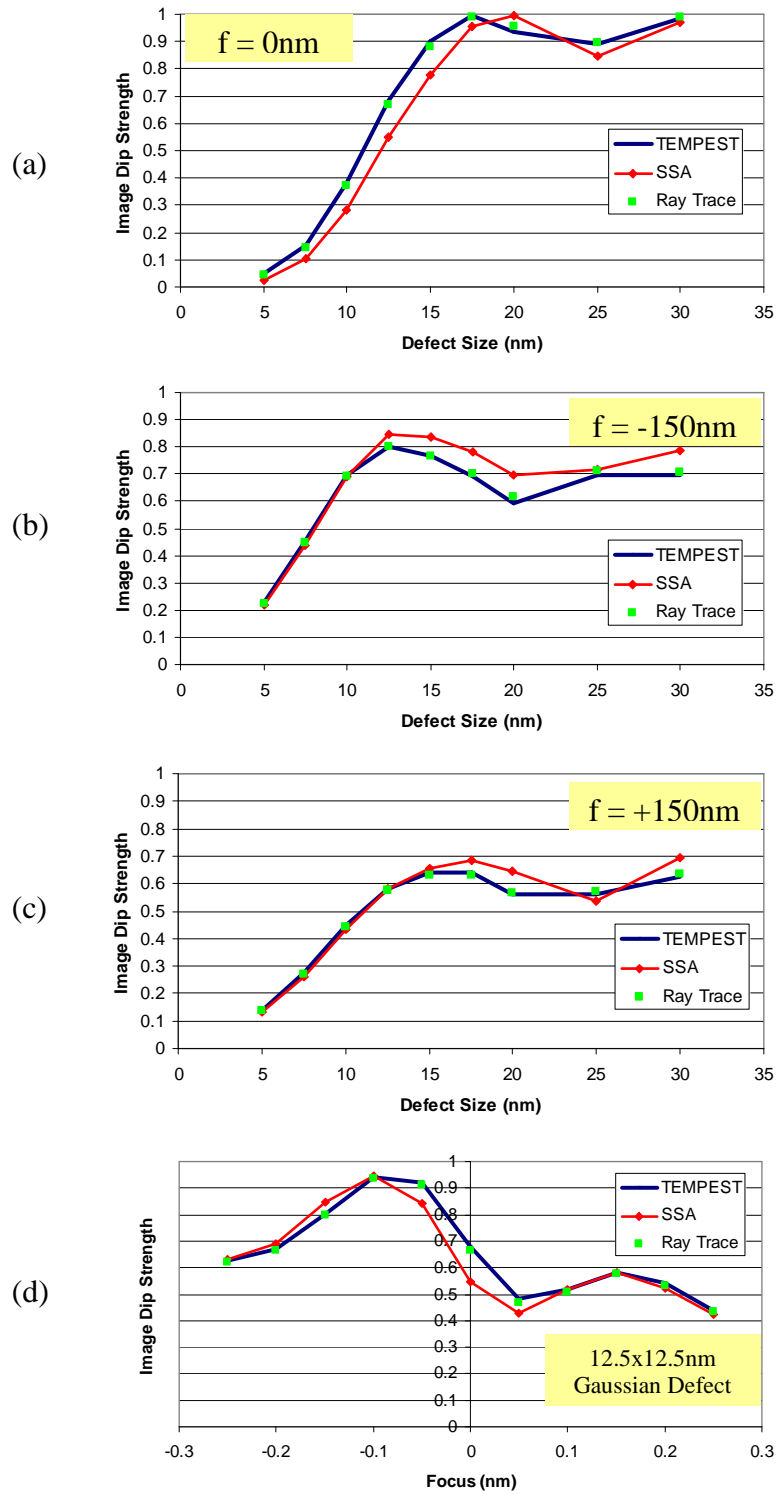# 2D Line Gaussian Defect Printability – Standard

Figure 7.5. Plot of the image dip strengths versus size for defects coated with a standard deposition process: (a) best focus. (b) -150nm focus. (c) +150nm focus. (d) Image dip strengths for a 12.5x12.5 nm Gaussian defect through focus.

that the SSA results are not nearly as good as the ray tracing results for predicting the quantitative numbers from FDTD.

Even though the above results are only for one 2D line shape, the ray tracing method can be expected to produce excellent results for other 2D line shapes, as well as 3D shapes coated with a standard deposition process. Chapter 6 already detailed the evolution from 2D results to 3D results for the smoothing process, and similar results can be expected for defects coated with the standard deposition process.

7.3 Defects Located Inside the Multilayer

Another important class of buried defects to consider is those which are partially buried inside the multilayer due to a particle falling on the mask blank during deposition. Their imaging severity will be increased since there are fewer layers above the defect to help mitigate its presence. The ray tracing method is once again compared to FDTD and SSA to test its accuracy on this class of defects. Three defect sizes were chosen to represent various defect categories: a 20x20nm box defect (very sub-printable), a 40x40nm box defect (slightly sub-printable), and a 60x60nm box defect (printable). These three sizes of defects were simulated at various locations inside the multilayer, starting from the substrate and moving up to the 35 bilayer of a 40 bilayer structure.

Figure 7.6 shows a matrix plot of the dip strengths at various locations within the multilayer for the three defect sizes at three different focal positions. From the in focus plots, it is clear that a buried defect will generally print worse as it is raised upwards inside the multilayer. A maximum printability impact begins to occur somewhere around
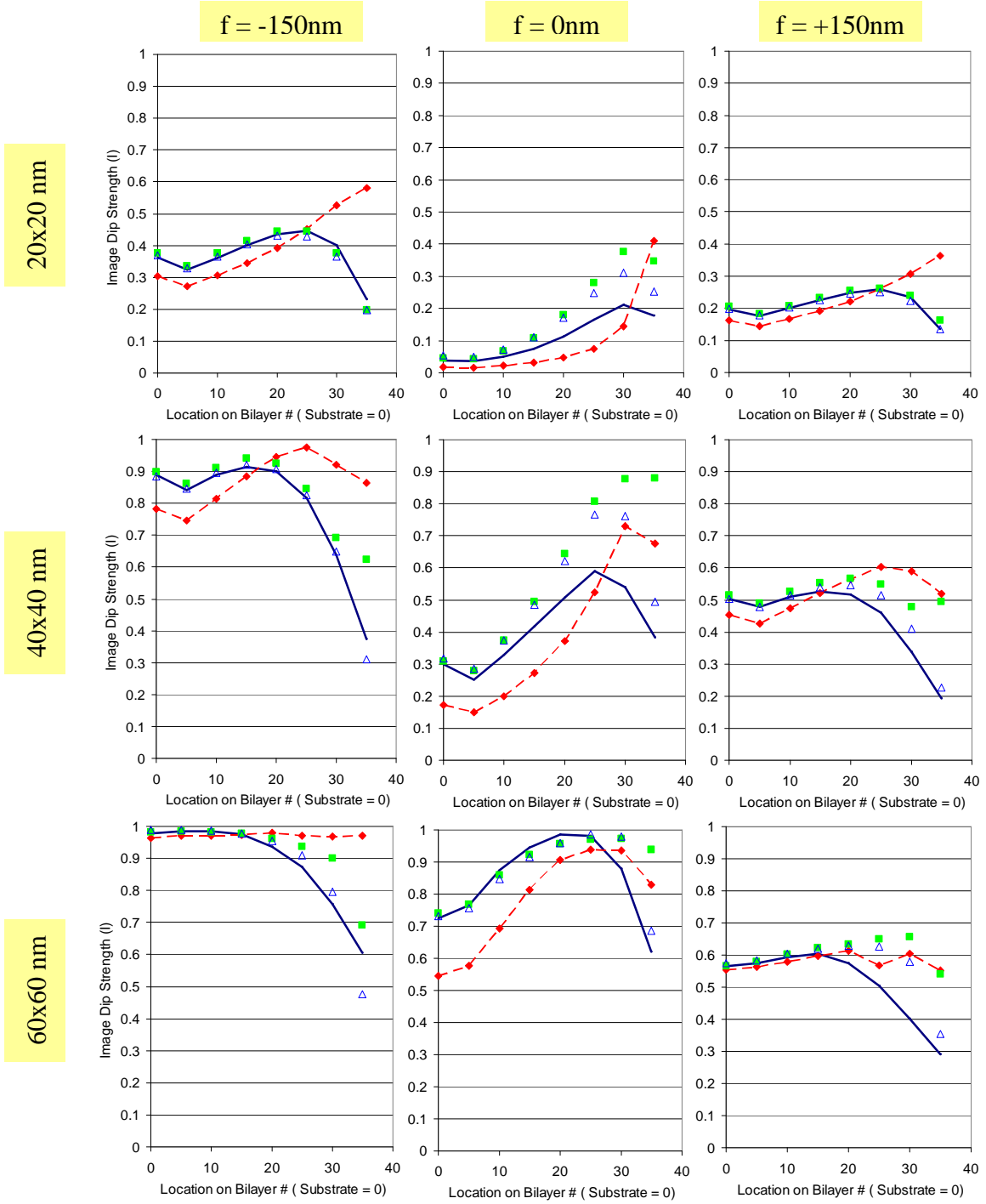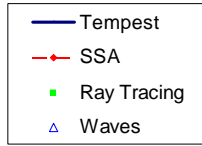
145

Figure 7.6. Matrix plot of the image dip strengths for 2D line box defects coated with the smoothing process. Three defect sizes and three focal positions can be compared.

the middle of the multilayer (depending on the defect size) since the defect begins to split the upper and lower portions of the multilayer in half, effectively limiting the multilayer's reflectivity. When a defect is raised extremely high in the multilayer (about top 10 bilayers, depending on defect size), it's printability impact is actually lessened since it leaves a large chunk of the multilayer undisturbed directly below it which can begin to compensate for the distorted layers above it. The printability impact for out of focus values remains relatively unperturbed, until the defect reaches about the middle of the multilayer, where the out of focus impact begins to decrease.

The SSA clearly shows strong deviations from FDTD predictions of defect printability when the defect is located higher in the multilayer, regardless of defect size or focal position. The ray tracing method generally shows good agreement with FDTD for defects located below 20 bilayers, but can begin to show large deviations for defects located very high in the multilayer. As the defect is pushed higher in the multilayer, the incident rays begin to see much more challenging topography and begin to refract to fairly large angles. The bilayers directly above the defect are no longer adequately approximated by two similar shaped layers and thus the second layer cannot act to undo the lensing effect of the first layer in the bilayer. So forward diffraction no longer can be neglected and the ray tracing method begins to become less accurate as the downward traced rays in the vicinity of the defect begin to cross each others paths and create shadow regions where diffraction must be modeled.

A fourth method is shown on the plots as the triangles and is listed as "waves". This method uses the spectrum approach for the inward push to deliver the incident energy into the multilayer, rather than ray tracing. All other aspects of the two methods

147

are the same. The waves approach generally does not differ significantly from the ray tracing approach (as stated in Chapter 6), however, the waves approach can be seen in Figure 7.6 to be more accurate than ray tracing for this particular application. While the waves approach still neglects the forward diffraction, it does not suffer from ray crossings or other errant rays which are diffracted to larger angles from the steep side walls of the defect when it is located very high in the multilayer. So, for this particular application, the use of the wave method is recommended to avoid the complications that arise from ray tracing into the more challenging topographies.

The ray tracing and waves approaches give good estimates of defect printability when the defects are located below at least 20 bilayers of material. While both the waves approach and the ray tracing approach fail to reliably give quantitative numbers of defect printability for defects located very high in the multilayer, both methods do give a general understanding of the trends involved and can thus still serve as a useful tool for understanding qualitative information in this regime.

7.4 Standard Deposition Landscapes

The simulation method can now be used to map out the landscape of 2D line defects that are printable when coated with a standard deposition process. Both Gaussian and box defects were simulated with heights and widths ranging from 2.5nm – 25nm in steps of 2.5nm. This range produced a total of 100 simulations per defect shape, and the dip strengths of all aerial images were taken and plotted at three different focal positions corresponding to 0 RU, +2RU, and -2RU (0nm, +150nm, -150nm). Contours were taken

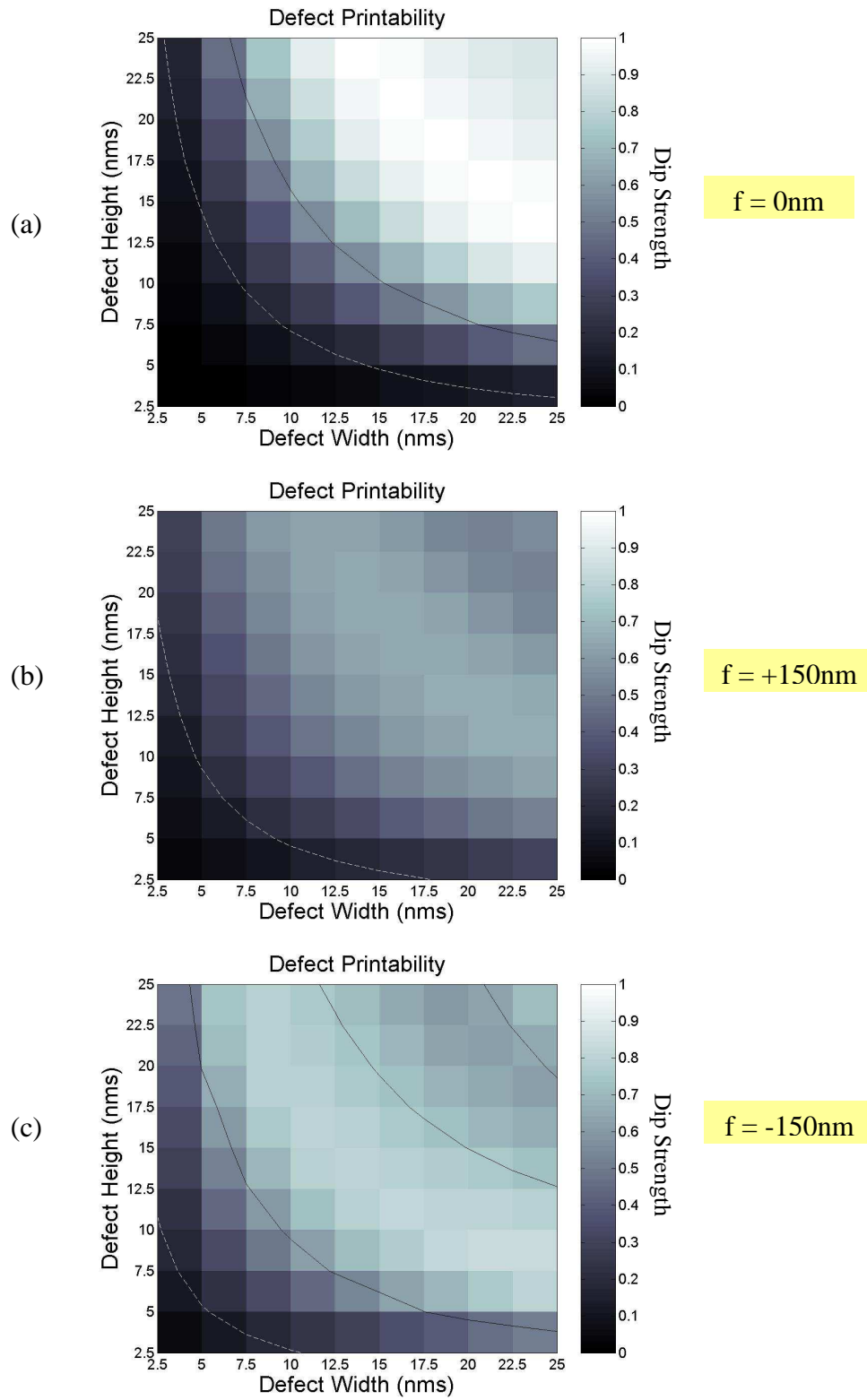2D Line Gaussian Defect Printability – Standard Deposition

Figure 7.7. Printability landscape maps for 2D line Gaussian defects coated with a standard deposition process for various heights and widths. Contour lines are also shown: black (0.7) and white (0.25).

at the 0.7 and 0.25 dip strengths to better show regions of printability. All defect sizes with dip strengths at or above the 0.7 contour represent isolated defects that are printable. All defect sizes above the 0.25 dip strength contour, but below the 0.7 contour, represent a warning region that are potentially printable when features are present above the surface.

Figure 7.7 shows the printability maps for 2D line Gaussian defects coated with a standard deposition process. The dark black lines represent the 0.7 dip strength contours, while the white dashed lines represent the 0.25 dip strength contours. Similar maps could be made for box defects, but are not shown. Notice that the in focus printability maps for Gaussian defects report a fairly large printability region in the upper right portion of the graph, with a thin warning region. All the defects are nominally sub-printable on the positive 150nm focal side, however, most of these defects still fall in the warning region which flags potential problems when features are present. The defects print very strong on the negative 150nm focal side, with a slight lull in the printability near the upper right corner, before being pulled back up with larger defect sizes. The greater imaging severity on only one side of focus shows that buried defects are behaving just as DUV phase defects were shown to behave in Section 4.2. Once again, the buried defect can be viewed as subtracting its electric field and reinjecting the reflected light with a new phase, while the focal variation serves to rotate a defect vector arm about the background electric field, as shown schematically in Figure 4.5. The addition of these vectors serves to create a maximum printability impact at the focal value that rotates the defect vector arm so that it points completely opposite the background field (180° phase difference). As a side note,

150

Box Defect			Gaussian Defect		
Original Size (nm)		**Volume**	**Original Size (nm)**		**Volume**
Width	Height	(nm^3)	FWHM	Height	(nm^3)
7.2389	25	180.9725	6.579	25	175.0782
7.5	24.1508	181.131	7.1797	22.5	171.9575
8.0316	22.5	180.711	7.5	21.3698	170.6059
8.8745	20	177.49	8.0335	20	171.0279
9.8328	17.5	172.074	9.091	17.5	169.3487
10	17.1398	171.398	10	15.6865	166.9776
11.2537	15	168.8055	10.4441	15	166.761
12.5	13.1987	164.9838	12.3393	12.5	164.1847
13.2636	12.5	165.795	12.5	12.332	164.0876
15	11.2369	168.5535	15	10.2097	163.0183
16.4644	10	164.644	15.2907	10	162.7645
17.5	9.3395	163.4413	17.5	8.8341	164.5631
20	8.3307	166.614	20	7.7282	164.5283
21.6772	7.5	162.579	20.5726	7.5	164.2414
22.5	7.2173	162.3893	22.5	6.991	167.438
25	6.5215	163.0375	25	6.4691	172.1536

Table 7.1. Printability size parameters extracted from 0.7 dip strength contours of 2D line defects coated with a standard deposition process.

the plots from Figure 7.5abc can be compared to the diagrams in Figure 7.7 by simply imagining a diagonal cut line across the printability maps.

One of the more useful aspects of these maps can be demonstrated by comparing all the defect sizes along the 0.7 contour at zero focus, which will allow the extraction of a key parameter that will characterize whether a defect will be printable without running a simulation. Table 7.1 shows the defect sizes along the 0.7 dip strength contour for both Gaussian and box defects, while Figure 7.8a plots the original defect volumes as a function of the original defect's aspect ratio (max height/FWHM or max height/width) for both the Gaussian and box defects. A striking similarity can be immediately seen, that their volumes are nearly constant for all aspect ratios and both shapes. This implies that a defect must have a minimum volume (~160 nm^3) in order to be printable, regardless of its physical shape or dimensions. A general rule can now be formulated: an arbitrary 2D line

Figure 7.8. (a) Original substrate defect volumes for printable defects coated with a standard deposition process at zero focus. (b) Zoomed picture of (a).

defect coated with a standard deposition process will be printable if its defect volume exceeds 160nm^3.

A closer look at Figure 7.8b shows that there is a slight dependence on the aspect ratio, namely that slightly larger defect volumes can be tolerated if their aspect ratios are large. The plot in Figure 7.8b is slightly deceptive however, because larger aspect ratio defects actually undergo a slight clipping effect that may not be physically real when coated with the growth model. Figure 7.9 demonstrates how larger aspect ratio defects begin to become clipped, so their actual volumes are slightly smaller than those calculated from their original defect dimensions. As such, the upward trend seen in

Figure 7.9. Effects of standard model growth on various aspect ratio defects. Clipping begins to affect aspect ratios greater than about 1.5. (a) Low aspect ratio. (b) Mid level aspect ratio. (c) High aspect ratio.
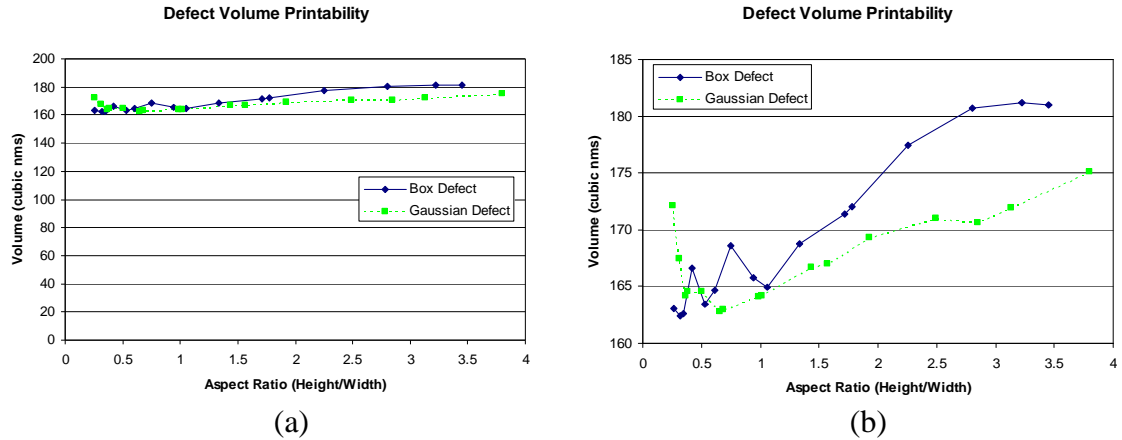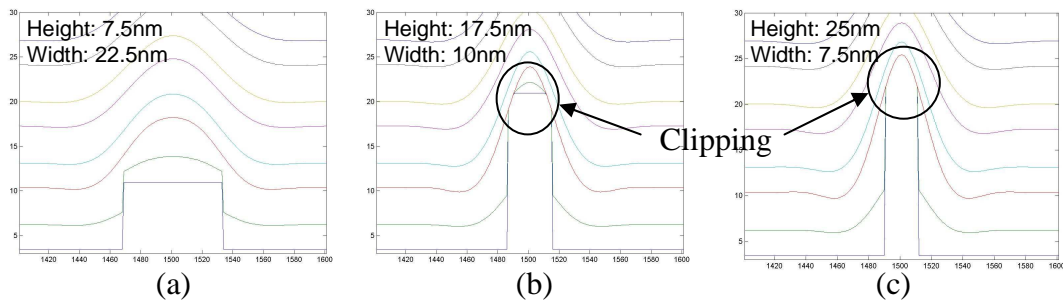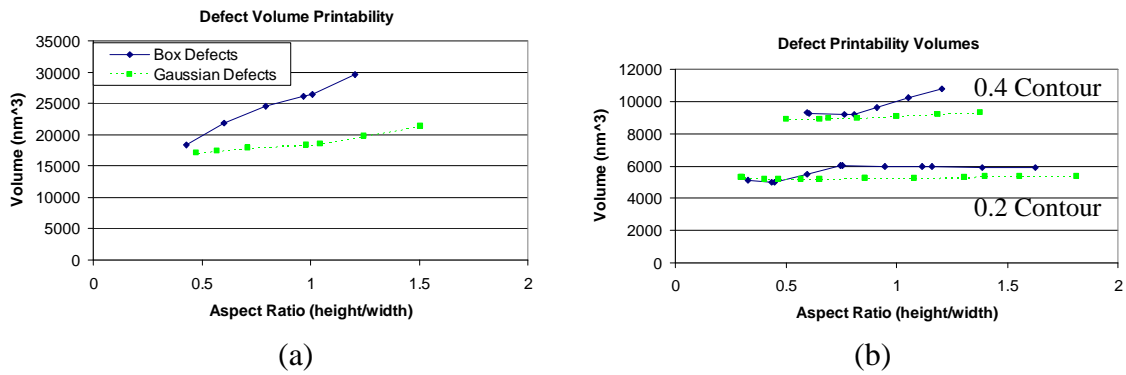
Figure 7.10. (a) Original substrate defect volumes for printable 3D defects coated with the standard deposition process at zero focus. (b) Various contours for smaller defects at constant dip strength show constant volume. Clipping is therefore likely responsible plot (a) not being constant in volume.

Figure 7.8b is slightly exaggerated by this clipping effect, and the actual volumes of these higher aspect ratio defects are probably smaller and thus the defect printability volume is more constant across all aspect ratios than the graph might suggest.

Defect printability maps for 3D defects coated with the standard deposition process can also be generated. For simplicity in generating the 3D defects, the width in both the x and y directions was assumed to be the same. Figure 7.10a plots the volumes of printable 3D defects as a function of their aspect ratio for both Gaussian and box defects, while Table 7.2 lists the defect sizes along the 0.7 contour. Constant volumes for defect

Box Defect			Gaussian Defect		
Original Size (nm)		Volume	Original Size (nm)		Volume
Width	Height	(nm^3)	FWHM	Height	(nm^3)
29.0838	35	29605.36	23.206	35	21356.65
29.7345	30	26524.21	24.0908	30	19728.23
30	28.9742	26076.78	25	26.1378	18510.3
31.3796	25	24616.98	25.4875	25	18401.74
33.1026	20	21915.64	28.0548	20	17836.46
34.9466	15	18318.97	30	17.1121	17450.59
			31.6912	15	17069.98

Table 7.2. Printability size parameters extracted from 0.7 dip strength contours of 3D defects coated with a standard deposition process.

153

printability are no longer observed to be true. However, the size of these defects are larger than their 2D counterparts and have a large amount of clipping that occurs for all aspect ratios, especially box defects. Box defects are more vulnerable to clipping, since they have sharp corners that protrude outwards and this manifests itself in the larger upward slope in Figure 7.10a for box defects. To verify that clipping is the cause for non-constant volumes across aspect ratios, Figure 7.10b compares various dip strength contours which are generated by 3D defects that are smaller and thus have less clipping. It can be seen that these contours obey a more constant volume prediction just like in 2D.

7.5 Smoothing Deposition Landscapes

The same procedure in Section 7.4 can be performed on 2D line defects coated with the smoothing process. Both Gaussian and box defects were simulated with widths of 20nm – 100nm in steps of 10nm and with heights of 10nm – 100nm in steps of 10nm. The printability maps for 2D line Gaussian defects coated with the smoothing process are plotted in Figure 7.11 along with the same 0.7 and 0.25 dip strength contours. The contour extraction of both shapes allows the defect sizes and volumes to be computed for defects that just start to become printable. Figure 7.12 plots the original defect volumes as a function of the original defect's aspect ratio (max height/FWHM or max height/width) for both the Gaussian and box defects with a focus of zero, while the defect sizes on the 0.7 contour are listed in Table 7.3. Clearly, no such general rule of thumb based on the volume of the substrate defect can be formed since the smoothing process changes the defect profile based on its shape. This effect was previously noted in Chapter 6 when

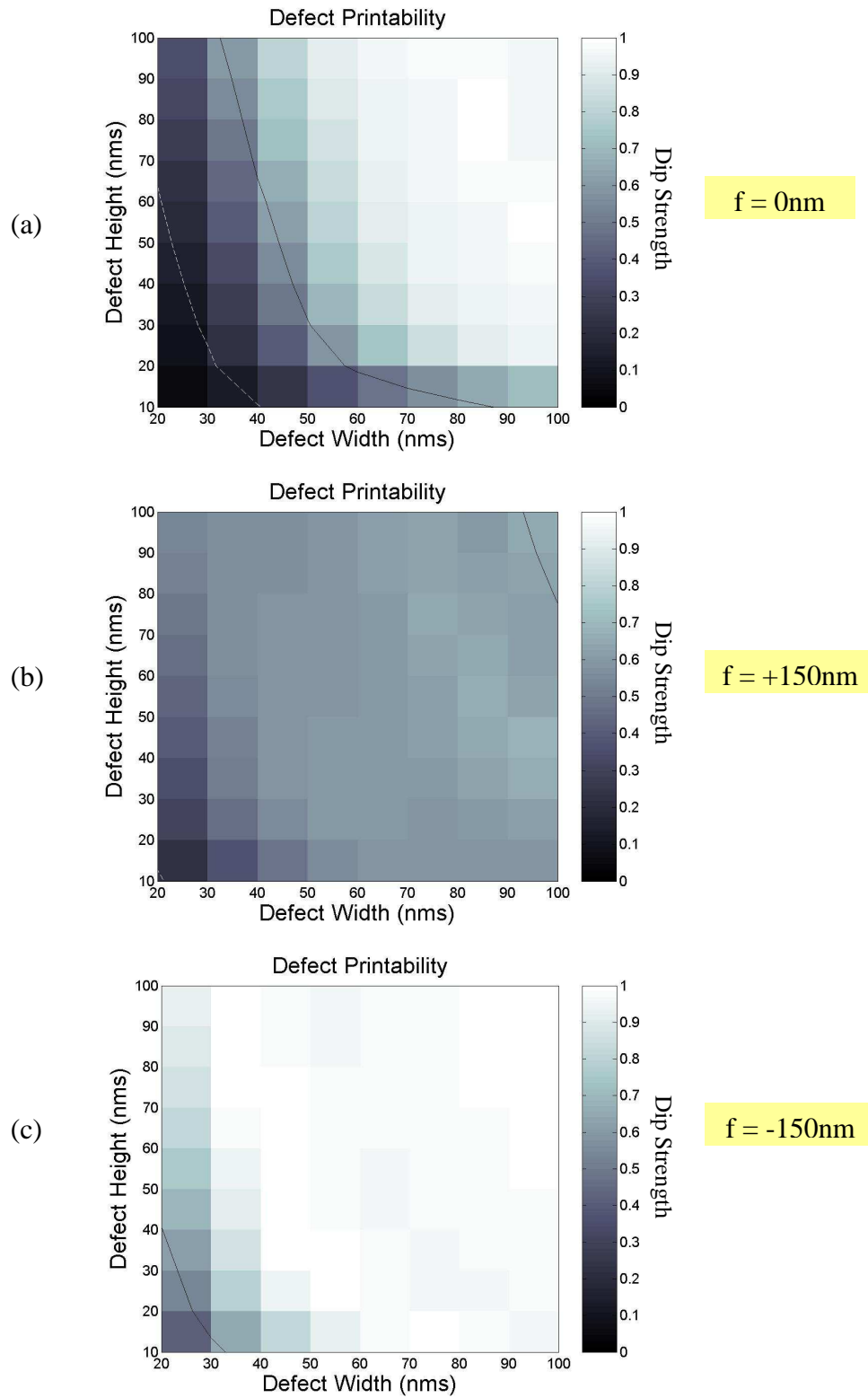2D Line Gaussian Defect Printability – Smoothing Deposition

Figure 7.11. Printability landscape maps for 2D line Gaussian defects coated with the smoothing process for various heights and widths. Contour lines are also shown: black (0.7) and white (0.25).

Box Defect Original Size (nm)		Volume	Gaussian Defect Original Size (nm)		Volume
Width	Height	(nm^3)	FWHM	Height	(nm^3)
41.7276	100	174119.3	67.5717	100	129033.2
43.8851	90	173331.2	68.908	90	123484.7
46.1953	80	170720.5	70	82.5104	116832.9
48.7172	70	166135.6	70.5194	80	108860.1
50	65.4978	163744.5	72.7662	70	99626.1
51.9945	60	162205.7	75.1948	60	89086.69
55.819	50	155788	78.0163	50	86812.1
60	40.0313	144112.7	80	44.6177	79058.27
60.0162	40	144077.8	82.266	40	66824.23
65.5604	30	128945	88.9066	30	52342.53
70	22.3416	109473.8	90	29.048	49903.83
71.5864	20	102492.3	100	22.2058	38009.58
78.727	10	61979.41			

Table 7.3. Printability size parameters extracted from 0.7 dip strength contours of 2D line defects coated with the smoothing deposition process.

Gaussian defects were shown to print worse than box defects when using the smoothing process. Figure 7.12 demonstrates the ability of the smoothing process to rapidly mitigate the effect of a defect with steep sidewalls, as box defects are allowed to have much larger volumes compared to the more smooth Gaussian shape before beginning to print. Figure 7.12 also shows that higher aspect ratio defects can be tolerated significantly better than low aspect ratio defects due to the smoothing. For instance, a defect with an aspect ratio of 3 is required to have 3 times more volume than a very low aspect ratio defect to
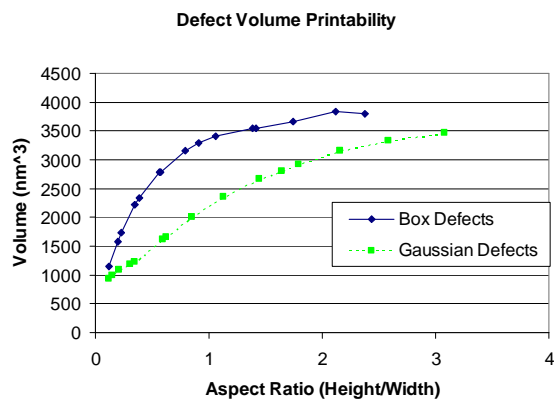

Figure 7.12. Original substrate defect volumes for printable 2D line defects coated with the smoothing deposition process at zero focus.
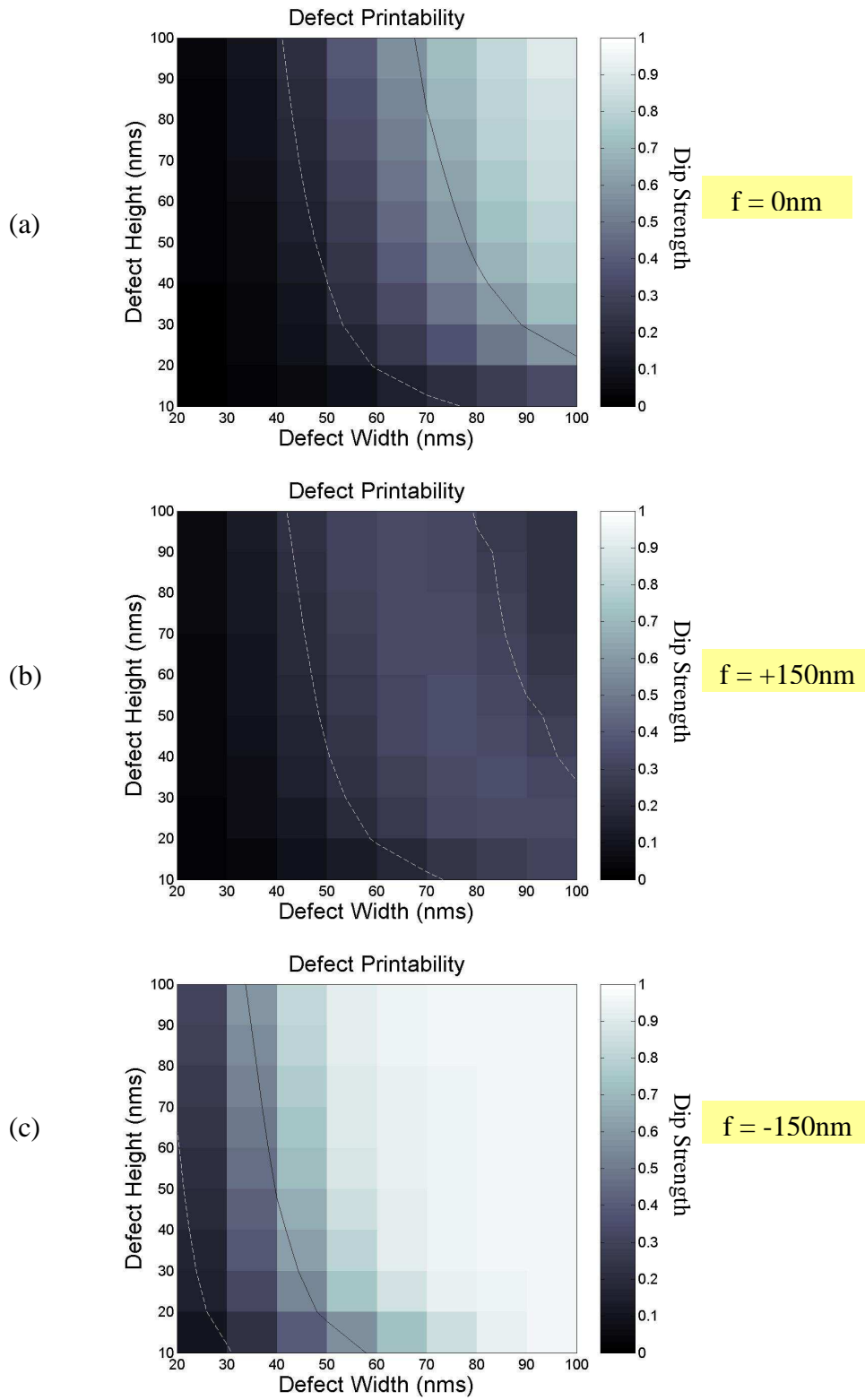
Figure 7.13. Printability landscape maps for 3D Gaussian defects coated with the smoothing process for various heights and widths. Contour lines are also shown: black (0.7) and white (0.25).

achieve the same printability. The smoothing deposition makes understanding defect printability much more difficult because there is not a single defect parameter that can be directly linked to printability (like volume was for standard coated defects). Thus, simulations will be needed to understand a smoothed defect's printability.

Finally, 3D printability maps can be generated for defects coated with the smoothing process. Figure 7.13 shows the image dip strengths for 3D Gaussian defects across a host of different sized defects. For simplicity, all 3D defects were assumed to have the same width in the x and y directions. These printability maps are similar to their 2D counterparts and the 0.7 dip strength contour can be extracted from the f=-150nm plot and the defect volumes can be plotted in Figure 7.14. Figure 7.14 is very similar to Figure 7.12 and shows the same generality that box defects are smoothed much better than Gaussian defects. Again, it is seen that the smoothing deposition process turns defect printability into a complicated process that is shape and aspect ratio dependent, allowing no general rules of thumb can be utilized to understand defect printability without performing simulations.
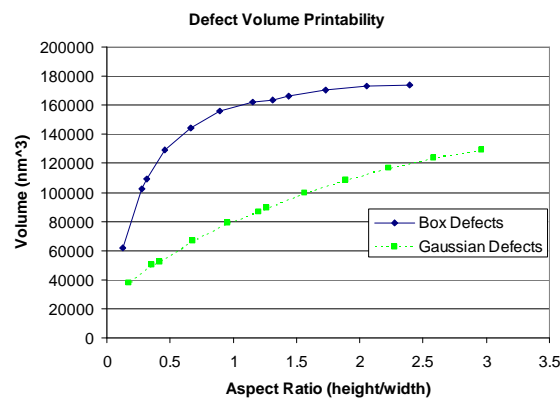

Figure 7.14. Original substrate defect volumes for printable 3D defects coated with the smoothing deposition process at f = -150nm.

7.6 Conclusions

The ray tracing method was shown to be accurate for modeling off axis illumination incident on the EUV mask blank. The accurate modeling of off axis illumination will be necessary for more accurate studies of EUV printability when more advanced illumination settings are used, since the constant scattering approximation will begin to break down. FDTD and the ray tracing method begin to differ in dip strength predictions for angles >9º. This difference stems from the numerical dispersion documented in Chapter 6 which changes the Bragg transition region and leads the FDTD method to predict wrong background reflection levels. At these larger angles of illumination, the ray tracing method may very well be more accurate than FDTD.

The ray tracing approach was also shown to accurately predict defect printability for defects coated with the standard deposition process. The accuracy attained on the smoothed defects shown in Chapter 6 as well as standard coated defects, which are more topographically challenging, shows that the ray tracing method is very robust for different deposition techniques and should be sufficient to predict defect printability as future deposition strategies are unveiled.

The defect printability maps generated for standard coated defects showed that a key parameter for defect printability is the defect's volume. In 2D, any arbitrary shape and dimensions were found to successfully print when the defect's volume was larger than $160nm^3$. The extrapolation of this rule to 3D defects coated with the standard deposition process was more difficult. The size of 3D defects that began to print under standard deposition conditions was large enough that the growth model began to show

clipping of the defect. This clipping is probably not physically real since the standard deposition process does not have an etching step. The impact of clipping, however, is seen in the volume results which require greater volumes at higher aspect ratios in order to successfully print.

Defect printability maps for 2D and 3D defects coated under the smoothing process were generated. Smoothed defects have significant clipping of the defect from the etching step which dramatically lowers the actual volume of the defect on the substrate and alters its printability. The clipping effect is highly shape and aspect ratio dependent, making it difficult to create a general printability rule for such defects. However, if the substrate volume after clipping were calculated, it is likely a constant or nearly constant volume rule would result. The difficult part is predicting the changed volume from the deposition process.

Of final note, Chapter 6 showed that the defect printability is highly dependent on the deposition process. The defect printability maps in this Chapter were generated from defects coated with the growth model developed by Stearns [42]. Different multilayer growth models will likely produce different printability results.

8 EUV Simulation Extensions: Defect Feature Interactions and Inspection

This Chapter will explore extensions of the ray tracing methodology to two additional challenges in EUV lithography. The first extension is to link the buried defect simulator to a new thin mask model for transmission through absorber features to rapidly assess a buried defect's impact on the printability of nearby features. Toward this end, the underlying physics of an absorber edge scattering is thoroughly investigated and simplified models for two of the key physical effects are shown to produce excellent results when compared to FDTD edge scattering. The simplified model effectively converts the electrically thick nature of the absorber patterns (~70nm or ~5λ thick) into a thin mask model, while capturing all of the appropriate effects that are demonstrated in the far field image. Line and space example patterns for dense 32nm, 22nm, and 15nm features (on wafer) will be shown which demonstrate the accuracy of the new thin mask model for even very tight pitches.

The second extension is to show the buried defect simulator can accurately handle the case of optical inspection, where the wavelength of light is much larger (488nm or 266nm) than the EUV 13.4nm exposure wavelength. At these larger wavelengths, the refractive indices are considerably different from those at EUV wavelengths and the defect sizes become significantly sub-wavelength, resulting in vastly different scattering

profiles and conditions. The buried defect simulator will be shown to accurately handle the case of optical inspection, despite a dramatically altered scattering environment.

All of the simulations performed in this Chapter assume that the absorber features are 70nm in height and made of TaN with a refractive index at $\lambda = 13.4$nm of $n_{TaN} = 0.9272128642 - j*0.0429253317$. For the inspection simulations, the refractive indices of the multilayer materials at $\lambda = 488$nm are $n_{silicon} = 3.2942 - j*3.6812$, $n_{moly} = 4.47784 - j*1.14546$, and $n_{ru} = 3.16 - j*4.71$. All other parameters for the multilayer are similar to those used in previous chapters.

8.1 Method for Linking Feature Transmissions and Buried Defects

The complete EUV photomask scattering problem is shown schematically in Figure 8.1 and can be decomposed into two smaller problems: 1) a transmission through the absorber features and 2) a reflection from a non-planar multilayer. Evanschitzky [53] has also noted a similar decomposition can effectively handle the full scattering problem by linking FDTD transmission through absorber features to a simplified model for
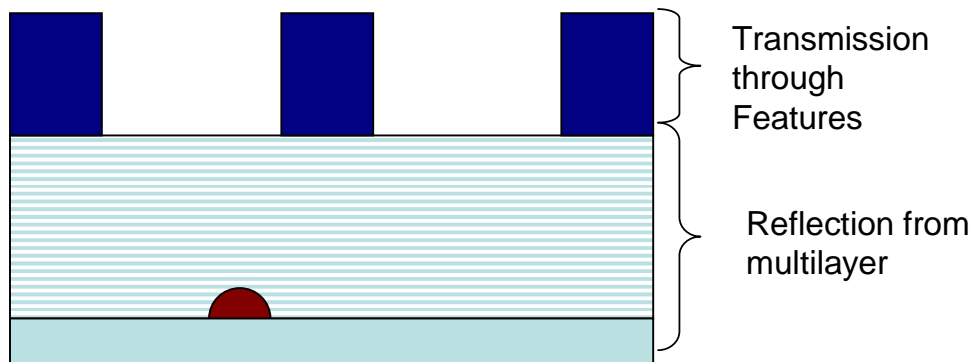

Figure 8.1. Complete EUV photomask domain with absorber features placed on top of a multilayer reflection stack. A buried defect is shown sitting below the multilayers.
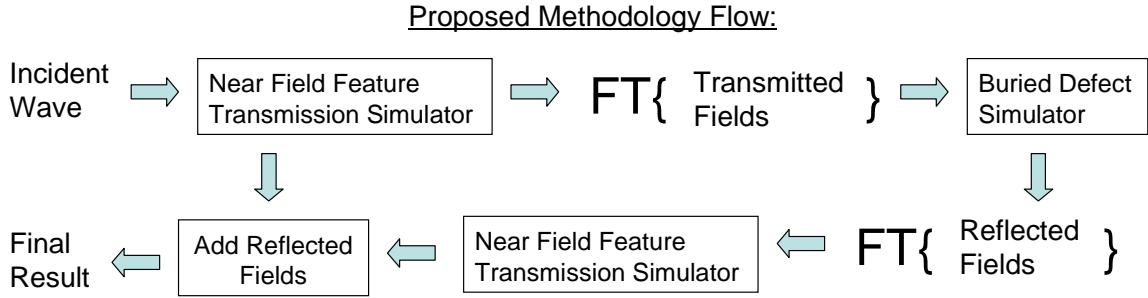
Figure 8.2. Proposed methodology flow for linking feature printability and buried defect printability.

defective multilayers. The methodology developed in Chapter 5 has already been

demonstrated to effectively handle the second part of the EUV scattering problem, and so

a fast and accurate method for handling the transmission through the absorber features is

all that is needed to completely model the problem.

Once appropriate methodologies have been identified for each part of the

problem, they can be linked together by the flow chart in Figure 8.2. An incident plane

wave onto the example structure in Figure 8.1 can be reflected and transmitted through

the absorber features via an appropriate simulator. The electric fields below the absorber

features can be Fourier transformed into its plane wave spectrum and each plane wave

fed into the buried defect simulator. The total reflection from the defective multilayer can

again be Fourier transformed into its plane wave spectrum and each plane wave

transmitted upward through the absorber features a second time. In this manner the

electric fields have been doubly diffracted by the absorber features during the downward

and upward pass. The total scattering from the EUV problem can then be made by adding

the initial reflection from the absorber features with the final output of the doubly

diffracted electric fields. This simple process ignores any secondary coupling between the

absorber features and the multilayer reflection. A full scattering matrix approach could

also be used to understand multiple re-reflections between the absorber features and the

163

multilayer structure. This approach would cause a significant increase in the computation time since each individual plane wave would couple into a set of many diffracted plane waves. However, the reflected fields computed from both objects for each angle of incidence could be reused for each additional reflection that occurs. It is anticipated that these second order effects are relatively small, since the reflection from the absorber features is on the order of 4% and should decay very quickly. Of final note, the initial incident plane wave can be generalized to a set of plane waves to account for partial coherence incident on the mask. The above process would then be repeated for each plane wave.

The full process outlined in Figure 8.2 will undoubtedly take longer to fully simulate an EUV structure than the buried defect simulator alone. While the additional step of creating a thin mask transmission function will not add appreciably to the runtime, the buried defect simulator will have to be run multiple times to properly reflect the diffracted fields passing down through the absorber features. A single incident plane wave will transmit through the absorber and be diffracted into a new set of n plane waves which each must be simulated with the buried defect simulator. Each of the n plane waves incident on the multilayer will produce another n plane waves that must be propagated upwards through the absorber features. In this sense, the full method will need to run the buried defect simulator at least n times, and thus should be at least n times slower when simulating features on top of a buried defect. A good estimate for a large 3D simulation would be about 50-100 times slower.

8.2 Analysis of Physical Edge Scattering

Before developing an appropriate model for transmission through the absorber features, the physical mechanisms that occur during transmission must be characterized and understood. There are three distinct regions in Figure 8.3 that must be analyzed to understand the transmission through the absorber features. First, a large dark area of absorber can be simply understood and characterized by understanding the transmission and reflection from a single bilayer made of the absorber material with the absorber's thickness. This can be easily modeled by Equations 5.7 and 5.8 which characterize the reflection and transmission from an arbitrary bilayer. Second, a large open area of the photomask can easily be understood by simply propagating the incident plane wave in free space by a distance equal to the absorber thickness. The last region consists of the area in the vicinity of an absorber edge. This region is the most interesting electromagnetically and the most complicated to understand. FDTD analysis will aid in verifying some of the physical characteristics that can be expected from scattering near an edge.
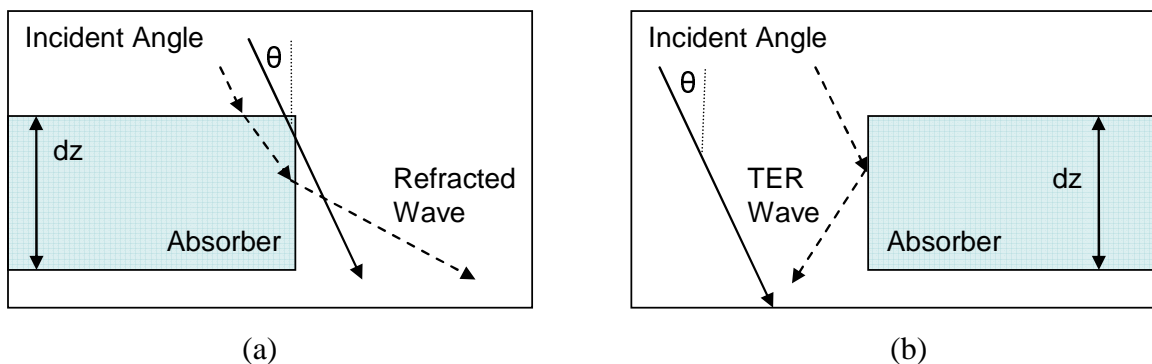

Figure 8.3. Definitions of (a) left absorber edge and (b) right absorber edge.

A simple manner to probe the edge scattering effects is to take the large dark area solution (a thick bilayer) and the large open area solution (propagating a wave in free space) and place each one next to an edge. This analysis forces two imposed solutions on Maxwell's equations on each side of the edge. Maxwell's equations will then respond to these imposed solutions, creating additional fields that will simply add via superposition to make the imposed solutions satisfy the appropriate boundary conditions at the edge interface. These additional fields can be viewed as physical response fields associated with approximating a thick mask scattering problem with a thin mask model based on vertical propagation. These response fields must also be modeled to fully calculate the near field transmission.

Two types of edges, a left edge and a right edge, will have to be investigated to deal with the edge orientation relative to off-axis illumination. A left edge is defined in this analysis as an edge with absorber on the left and air on the right with the incident light coming across the edge from left to right, as shown in Figure 8.3a. A right edge is defined in this analysis as an edge with absorber on the right and air on the left with the incident light coming across the edge from left to right, as shown in Figure 8.3b. Each type of edge can be analyzed under normal incidence and off-normal incidence.

Under normal incidence light, both a left edge and a right edge behave as mirror images of each other, so only a left edge will be investigated. The first half of the imposed solution, the light propagating down on the air side of the edge, will have to set up a new set of fields within the absorber to satisfy the boundary conditions on the edge. Snell's Law and the Fresnel Equations (Equations 5.3 and 5.5) show that the plane wave propagating down the interface will have a transmission coefficient of 0 along the

interface, showing that no energy is transferred across the vertical interface and an evanescent wave is set up in the absorber that decays exponentially laterally into the absorber but propagates vertically down the edge interface. The second imposed solution, a plane wave propagating vertically down the interface in the absorber region, the plane wave will actually refract out of the absorber material and begin propagating in the air at an angle of about 23° relative to the vertical. This angle can be directly calculated by solving Equations 5.3 for θ_2 given $\theta_1 = 90°$. These two effects can be seen in Figure 8.4, where FDTD has simulated a TE plane wave scattering from an isolated left absorber edge. Figure 8.4a shows the total electric fields in the vicinity of the edge, while Figure 8.4b shows the total electric fields of an edge with the imposed solutions subtracted out. Obviously from Figure 8.4b, the response fields from imposing these two solutions come from the edge effects, which were expected.

The physical response fields can be further analyzed by looking at their phase and instantaneous magnitudes. On the left of the edge location in Figure 8.5, an evanescent field is set up inside of the absorber while a refracted transmitted wave is being generated on the right side of the edge location in air. These effects are the two first order corrections that were described above to the imposed solutions. The refracted wave's angle can be measured and it appears to be traveling at approximately 23° which was predicted. Another interesting effect is seen in Figure 8.5a whereby a point source is actually radiating from the top corner of the absorber edge. Figure 8.5b confirms the cylindrical nature of the point source by looking at the phase of the error fields.

A left and right edge can be analyzed at an off-axis angle by looking at FDTD simulations as well. A left edge will still have a refracted wave propagating from the

167

(a)

(b)
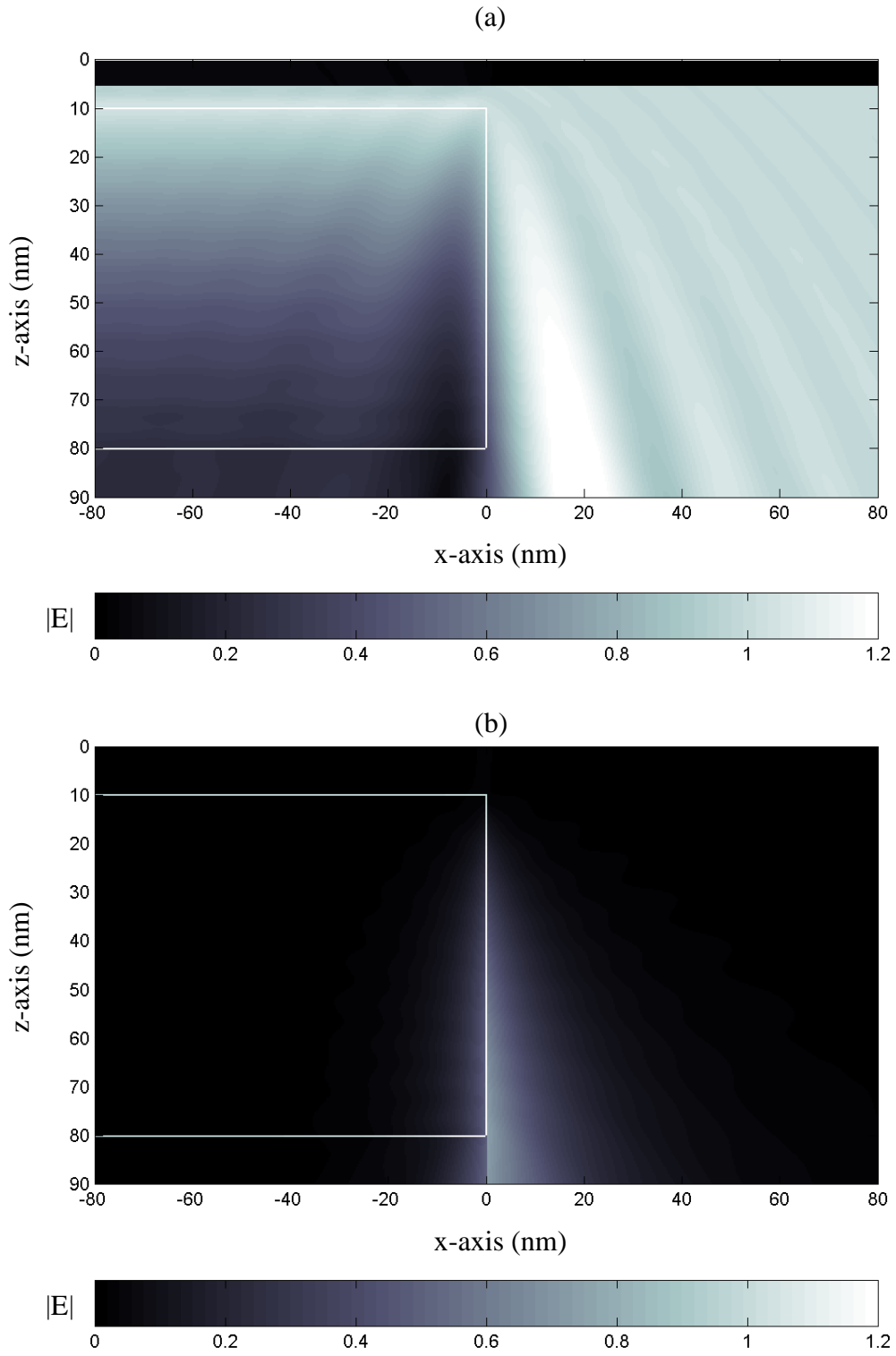
Figure 8.4. (a) |E| for isolated left absorber edge with absorber outline, (b) |E| of error field for isolated left absorber edge with absorber outline.

(a)

|E|

(b)

Phase
(radians)

Figure 8.5. (a) Instantaneous error field for isolated left absorber edge with absorber outline at normal incidence, (b) Phase of error field for isolated left absorber edge with absorber outline at normal incidence.
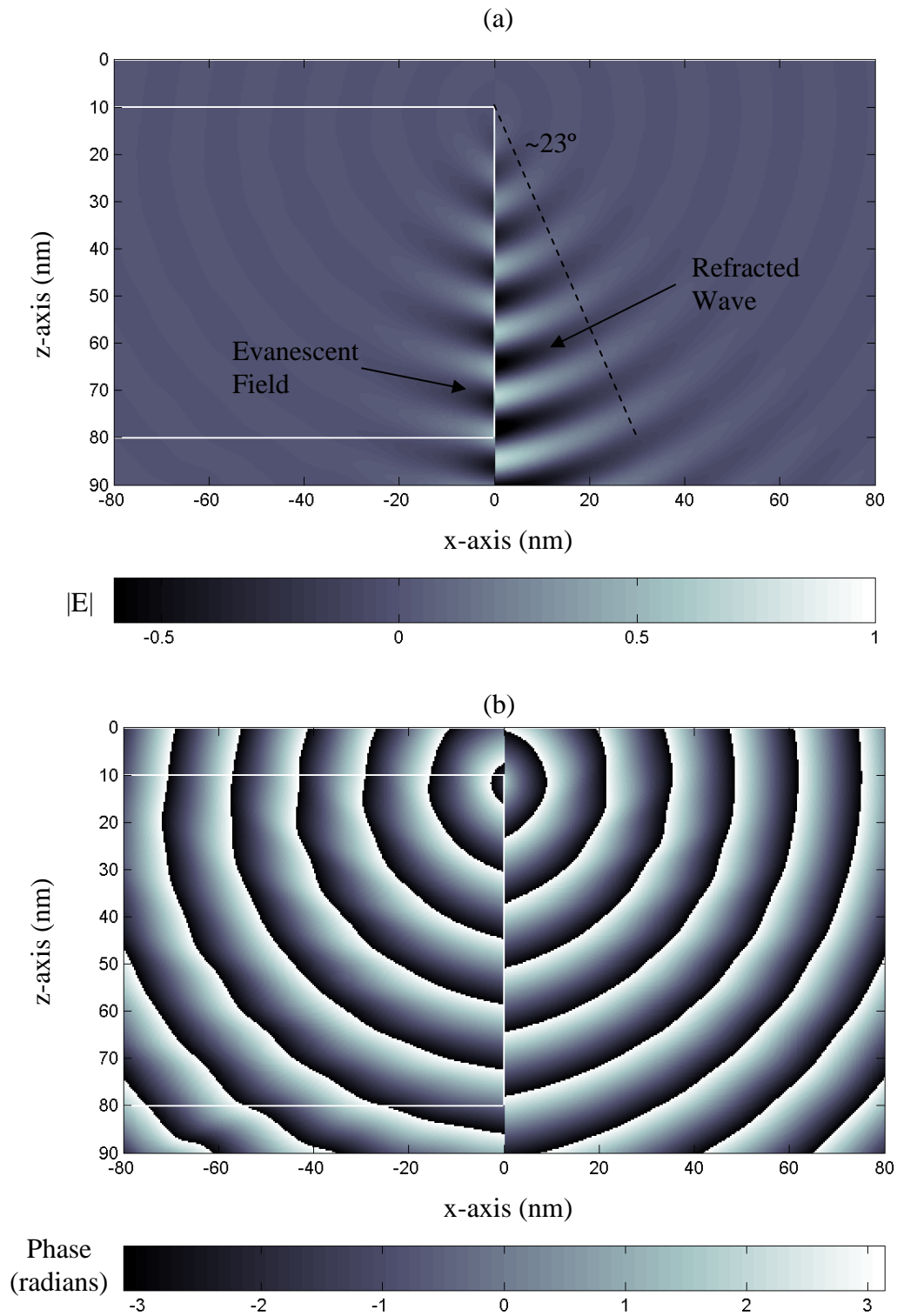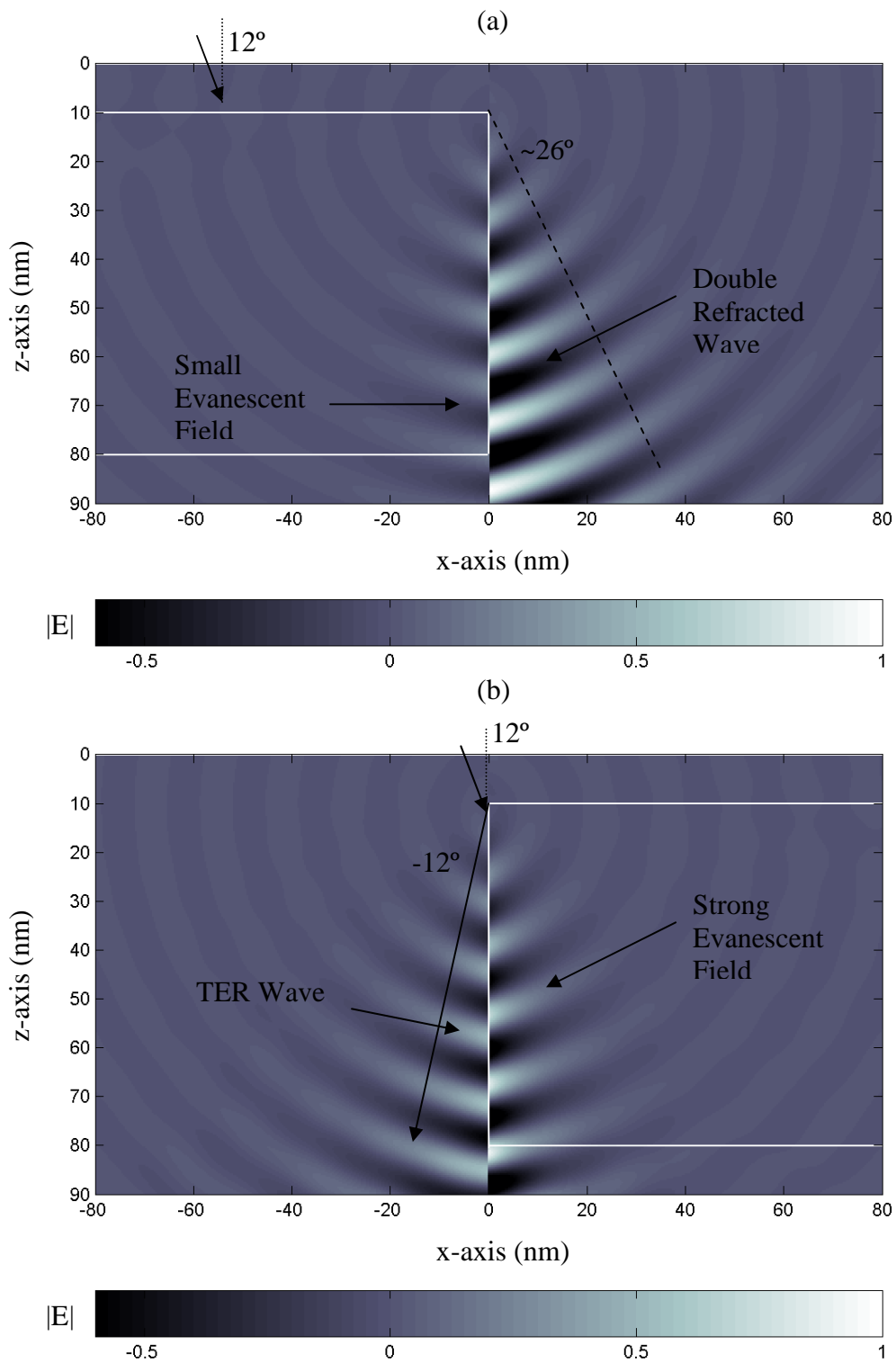
Figure 8.6. (a) Instantaneous error field for isolated left absorber edge with absorber outline for a 12° incident wave, (b) Instantaneous error field for isolated right absorber edge with absorber outline for a 12° incident wave.

absorber material into the air region due to the double refraction at the top surface and the edge interface. The angle of the refracted wave will be larger with an off-axis incident wave since the additional incident angle will provide an even larger refracted angle. The evanescent field within the absorber material, however, will be greatly diminished with angle due to the shadow region created by the thick absorber feature. Figure 8.6a shows the response fields for a left absorber edge for an incident off-axis plane wave. The double refracted wave is clearly seen and the evanescent field inside the absorber is significantly reduced. A point source at the top corner of the absorber is also present, just like at normal incidence. A right edge will have some interesting changes at off-normal incidence. First, the incident light impinging on the edge will be totally externally reflected (TER) from the edge interface for any incident angle less than 23º (note that this angle is consistent with the previous angle of minimum angular deviation for a refracted wave due to reciprocity). This reflection creates a wave propagating at the negative incident angle that folds back on top of the original incident wave. The TER at the interface also creates an evanescent field inside the absorber material. The refraction at the top surface of the absorber creates a shadow region in the absorber material that limits any refraction of light back out of the absorber into the air. Figure 8.6b shows the instantaneous response electric fields from a right absorber edge. The TER can be immediately seen to the left of the edge location and its angular spread is significantly less than the double refracted wave (which is absent from the right edge) for the left edge case. The evanescent field from the TER can also be seen inside of the absorber. A point source can once again be seen emanating from the top corner of the absorber edge.

8.3 Simplified Model of Feature Transmission

The simple thin mask transmission model that was used as an imposed solution on Maxwell's equations is the starting point of a simplified model for predicting the transmission of a plane wave through the absorber features. The physical response fields discussed in the above section represent the sources of error that the thin mask model makes relative to a rigorous solution for the diffraction scattering. It appears that significant errors are encountered when imposing the thin mask model onto the scattering from an isolated edge. Point sources, refracted fields, TER fields, and evanescent fields are all missing from the thin mask model and cause significant deviations to be encountered in the vicinity of an absorber edge. Each one of these effects would need to be accurately modeled and added to the thin mask approximation to obtain an accurate near field description of the edge scattering.

However, all except for one of these sources of error can be largely ignored in the far field image since their effects are mostly contained in the high spatial frequencies that scatter outside of the imaging optic. This limited angular collection will allow three of the four response fields to be neglected in a new scattering model. First, the evanescent fields are likely negligible in the far field due to the nature of evanescent fields and the high spatial frequency content of their laterally localized fields. Second, the refracted waves can also be largely ignored because they propagate at a minimum angle of 23°, which is significantly larger than the maximum collection angle of the EUV optic with an NA = 0.4. Similarly, the TER fields can be neglected because they propagate at negative the incident angle. This is because EUV systems are telecentric about 6° and the TER fields
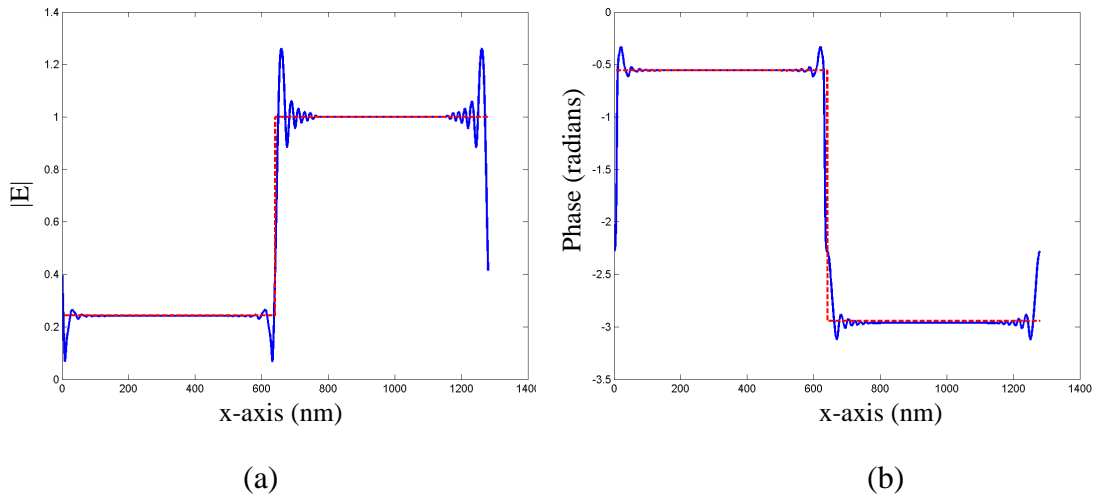
Figure 8.7. Cut lines below the absorber for the electric field from a normally incident plane wave. Solid blue lines are FDTD and red dashed lines are the thin mask model. (a) magnitude and (b) phase.

would scatter to an angle equal to their propagation angle plus 6º out of the center of the pupil. This argument means the TER fields will likely scatter outside of the pupil as well for incident angles greater than 3º. A sine effect can be used to argue that TER fields under 3º are also negligible since the amount of absorber edge that the incident fields actually see is proportional to the sine of the incident angle. Thus, the magnitude of those TER fields that are under 3º is likely very small. The point sources observed in Figures 8.5 and 8.6 cannot be neglected, however, since they fill the entire pupil of the imaging system and will definitely contribute some energy to the final observed image.

To prove that the above approximations are reasonable, cut lines of the thin mask model and the rigorous FDTD results must be compared. Figure 8.7 shows the calculated magnitude and phase of the near field transmissions of a normally incident plane wave for FDTD and the thin mask model for two edges separated by a large distance. The thin mask model is quite accurate far away from the edge locations, while significant errors are observed close to the edge. A better understanding of the errors can be obtained by
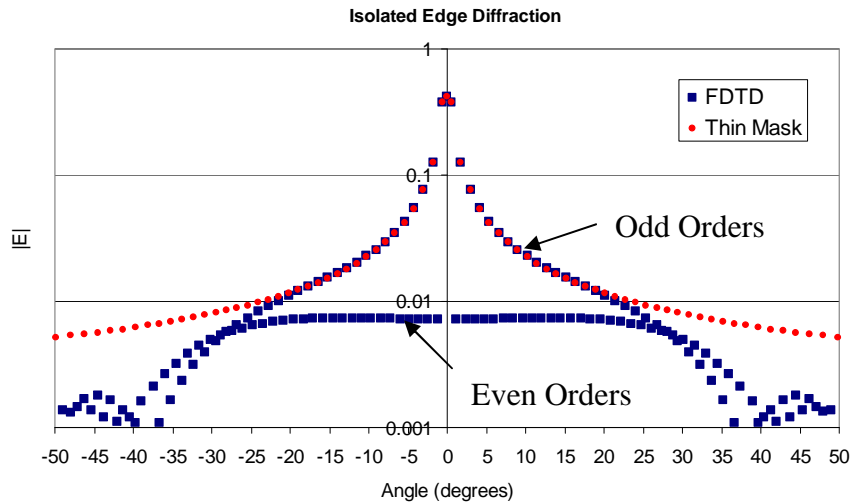
173

Figure 8.8. Angular spectrum of cut lines for two absorber edges very far apart for both FDTD and the thin mask model.

looking at the spectrums of the two methods, as shown in Figure 8.8. For angles within a ±20° cone, the thin mask model is predicting very nice results compared with FDTD for all of the odd orders, but all of the even orders are wrong. The thin mask model assumes a perfectly odd function describes the transmission function, leaving all the even orders set to zero. From Fourier analysis, the even orders come from an even symmetry in the transmission function that is double the period of the original odd function. Figure 8.8 shows that the even orders are nearly flat across all the angles of interest, and so a simple model for these even orders is to simply add a constant background to the even orders that exactly matches those taken from the FDTD solution. Doing this and inverse Fourier transforming the constant even orders, results in a spatial representation of the error fields between FDTD and the thin mask model when looking inside a small angular cone. These error fields turn out to simply be shifted and scaled impulse functions that occur at the absorber edges! So in fact, the point sources observed in Figures 8.5 and 8.6 at the corners of the absorber are the only edge effects needed to improve the thin mask model. And these can be modeled by simply adding the scaled impulse functions to every edge
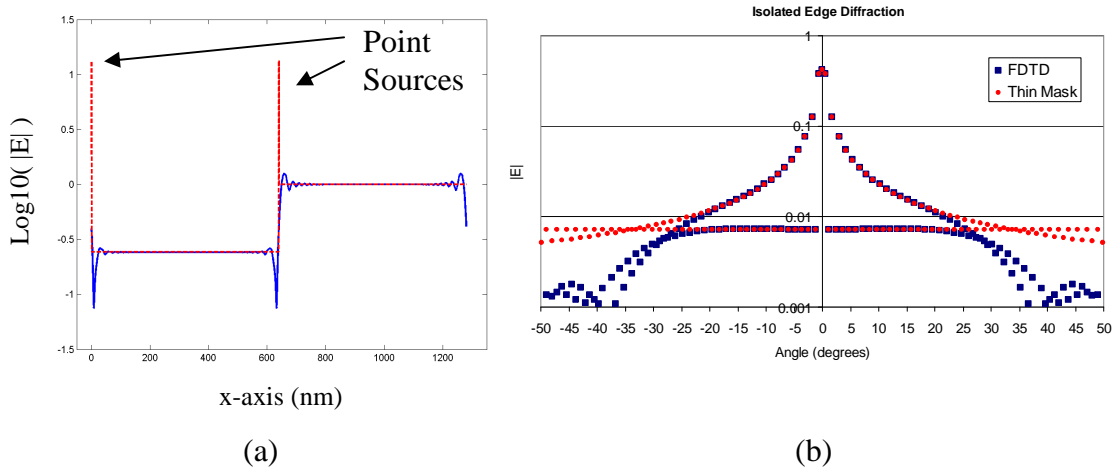
Figure 8.9. (a) New transmission function with corner point sources plotted on a log10 scale with the FDTD results. Solid blue lines are FDTD while red dashed are the thin mask model. (b) the spectrum of the two methods showing excellent agreement in all of the orders.

in the simulation. Figure 8.9a shows a new transmission function with the corner point sources added plotted on a log10 scale, while Figure 8.9b shows the |E| of the spectrum from both FDTD and the improved thin mask model. The point sources can be more clearly seen on the log scale and provide a constant background in the even orders in the corresponding spectrum. In this manner, the corner point sources will need to be characterized for the type of material and thickness that is used for the absorber using a single FDTD simulation, but these point sources will then scale any arbitrary configuration. The point sources for the TaN absorber with thickness of 70nms are:

Equations 8.1, 8.2:
$$E_{TE\_pt\_source} = 13.35e^{-j0.140971}$$
$$E_{TM\_pt\_source} = 13.35e^{-j0.035537}$$

An investigation into the phase of the spectrum is needed to fully characterize an isolated edge scattering. Figure 8.10a shows the phases of the angular spectrums for the FDTD results and the improved thin mask model for a normally incident plane wave. Clearly the phases of the thin mask spectrum are significantly different from the phases
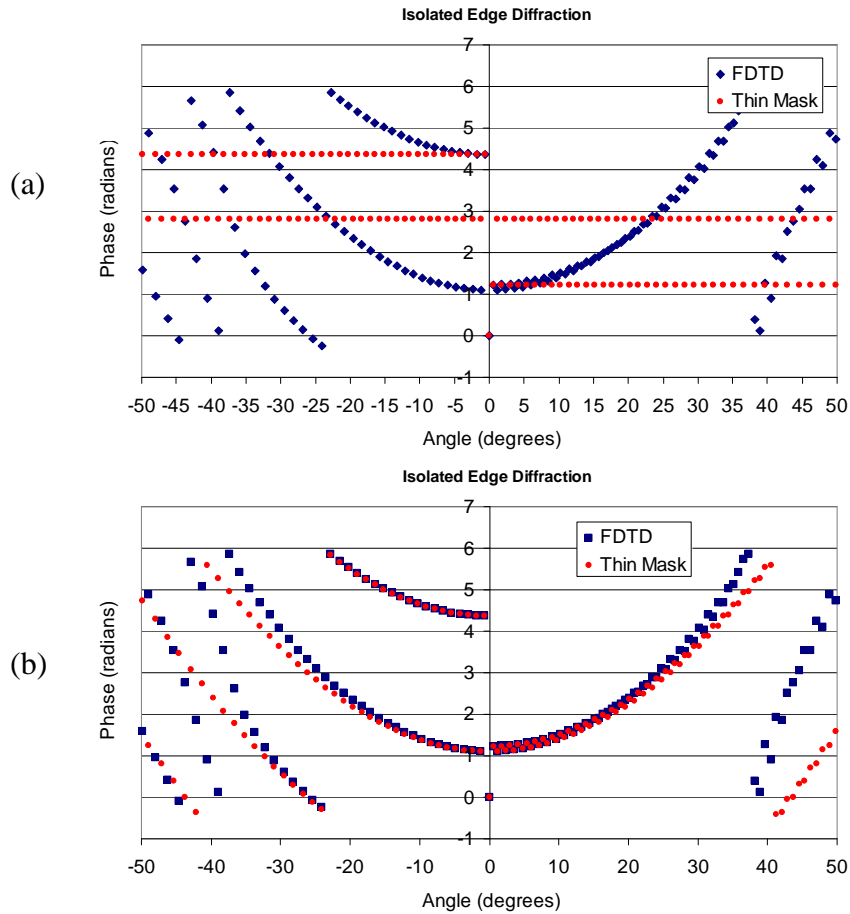
Figure 8.10. (a) Spectrum phases of thin mask model and FDTD without propagation (b) Spectrum of phases of thin mask model and FDTD with 40nm propagation.

of the FDTD results. The thin mask model has zero phase dependence on the angular

spectrum while the FDTD has an almost parabolic dependence on spectrum angle. This

effect most likely comes from the instantaneous aperturing assumptions built into a thin

mask model. As its name suggests, a thin mask is infinitely thin and its effects on an

incident plane wave are instantaneous. However, the EUV absorber features are very

thick (~5λ) and take some propagation distance to actually arrive at their final values

below the mask absorber. If the improved thin mask model is propagated forward by

some distance z_o, the flat phase dependence will begin to take on the characteristic

parabolic (or spherical wave) phase dependence for the angular spectrum. The propagation distance z_o will also depend on the material properties and thickness of the absorber, just like the corner point sources. However, the propagation distance can be characterized for the type of absorber and then used for arbitrary configurations of absorber edges. For the 70nm thick TaN absorber in these simulations, $z_o = 40$nm was found to match the spectrum phases very nicely, as seen in Figure 8.10b. The 40nms seems reasonably valid since it represents about half the absorber thickness.

The simple model proposed above should work for off-axis illumination as well, since the point sources are relatively independent of angle of incidence. The constant spectrum approximation can therefore be used as a simple way to model off-axis illumination. The final methodology for obtaining a thin mask model of transmission through EUV absorber features is a four step process:

1) Create an on-axis, binary transmission function by looking at the transmission through a large open area and a large dark area of the mask.

2) Add scaled impulse functions to every edge in the pattern.

3) Shift the 0th order of the transmission function to the appropriate incident angle.

4) Propagate the orders by z_o and inverse Fouier transform to obtain the near fields.

8.4 Examples: Dense Line and Space Pattern Transmissions

The simplified model for a thin mask transmission function described in the previous Section worked very well for modeling an isolated EUV absorber edge. It is only natural to question whether such a simple model will hold as feature edges become significantly closer together. This Section provides several examples of feature transmissions through dense line and space patterns. Since the targeted entry of EUV lithography is below the 32nm node, three line space patterns (32nm, 22nm, and 15nm features on wafer) will be tested for both polarizations at three different angles of incidence ($0°$, $\sim6°$, $\sim12°$), resulting in 18 test cases.

The 32nm line and space pattern actually has dimensions of 128nm on the mask (4X magnification). To properly compare the FDTD and thin mask model results, the final transmissions can be filtered down to only those plane waves physically entering a NA=1.0 system operating at 4X reduction, resulting in an angular collection cone of about $\pm15°$. Since real EUV systems will operate at significantly reduced NA's, the true results are expected to be even better than those compared here. Figure 8.11 shows the filtered near field magnitude and phase for the TE polarization at various angles of incidence on the mask. Clearly, the thin mask model does an exceptional job of modeling the FDTD results for $0°$ and $6°$, however, the model becomes less accurate as the angles

Near Fields. TE Polarization. 32nm Features

Figure 8.11. Filtered (NA = 1.0), coherent, near field transmissions of a TE plane wave for various angles of incidence through line space patterns giving 32nm features on the wafer.

Figure 8.12. Filtered (NA = 1.0), coherent, near field transmissions of a TE plane wave for various angles of incidence through line space patterns giving 22nm features on the wafer.

Near Fields. TE Polarization. 15nm Features

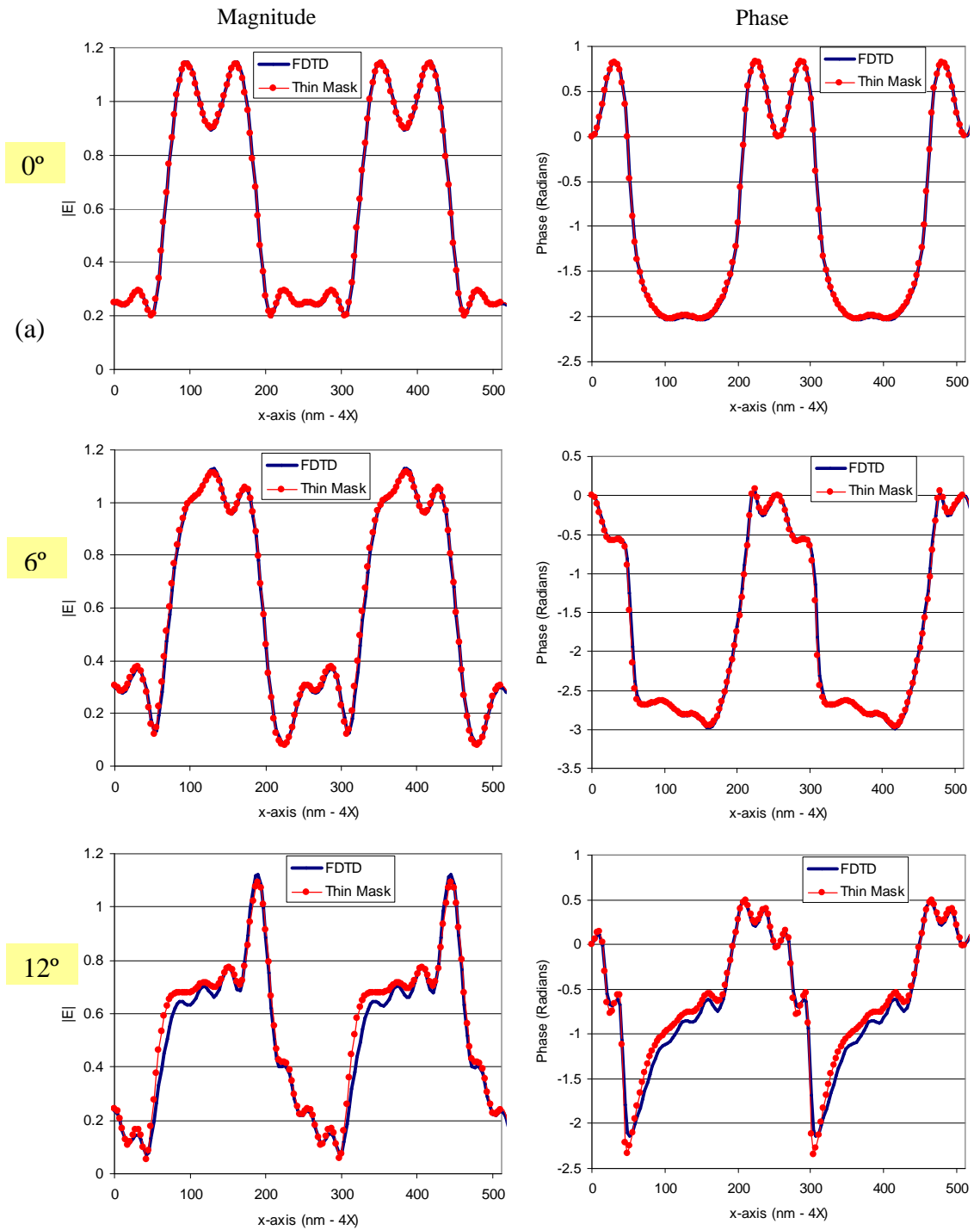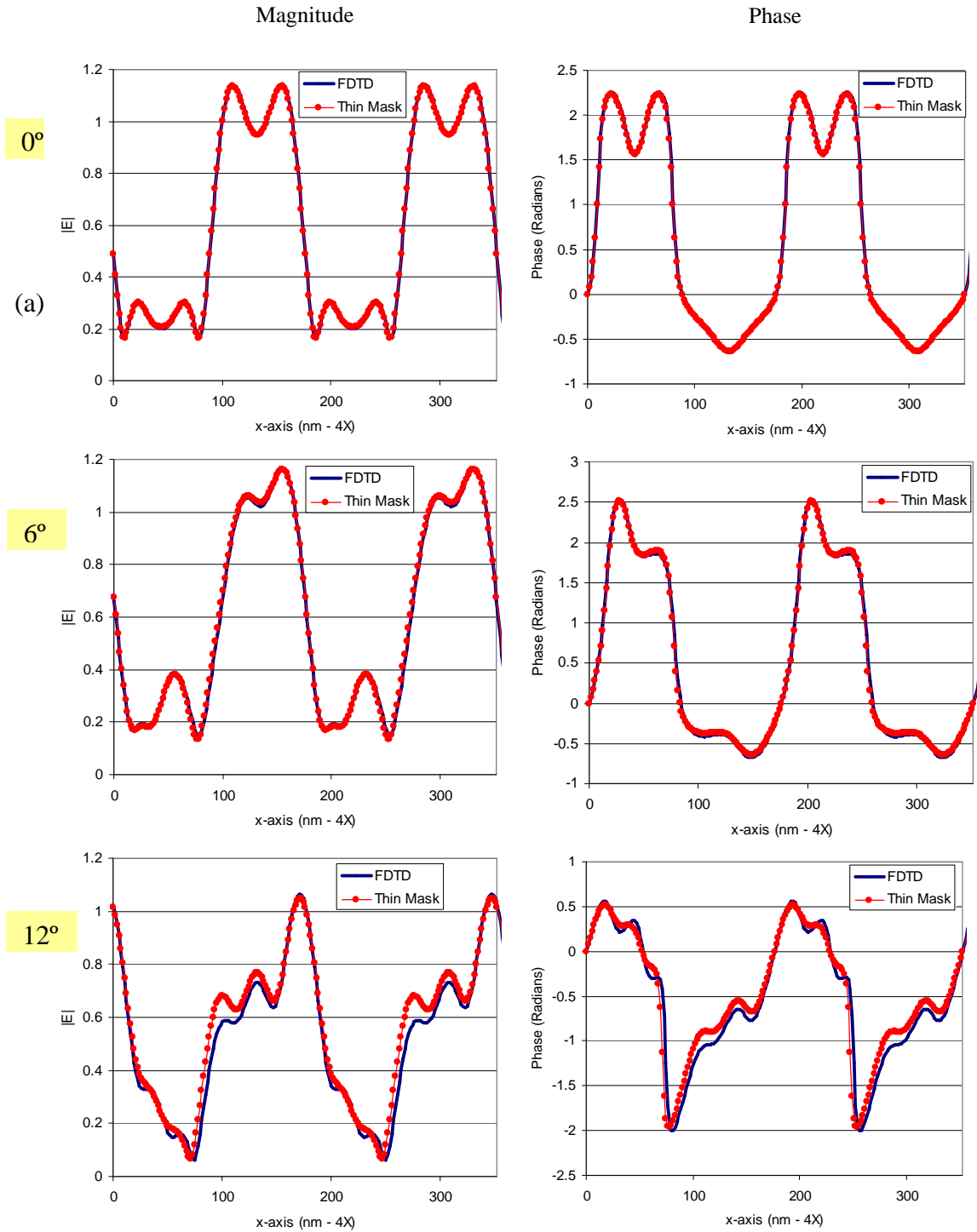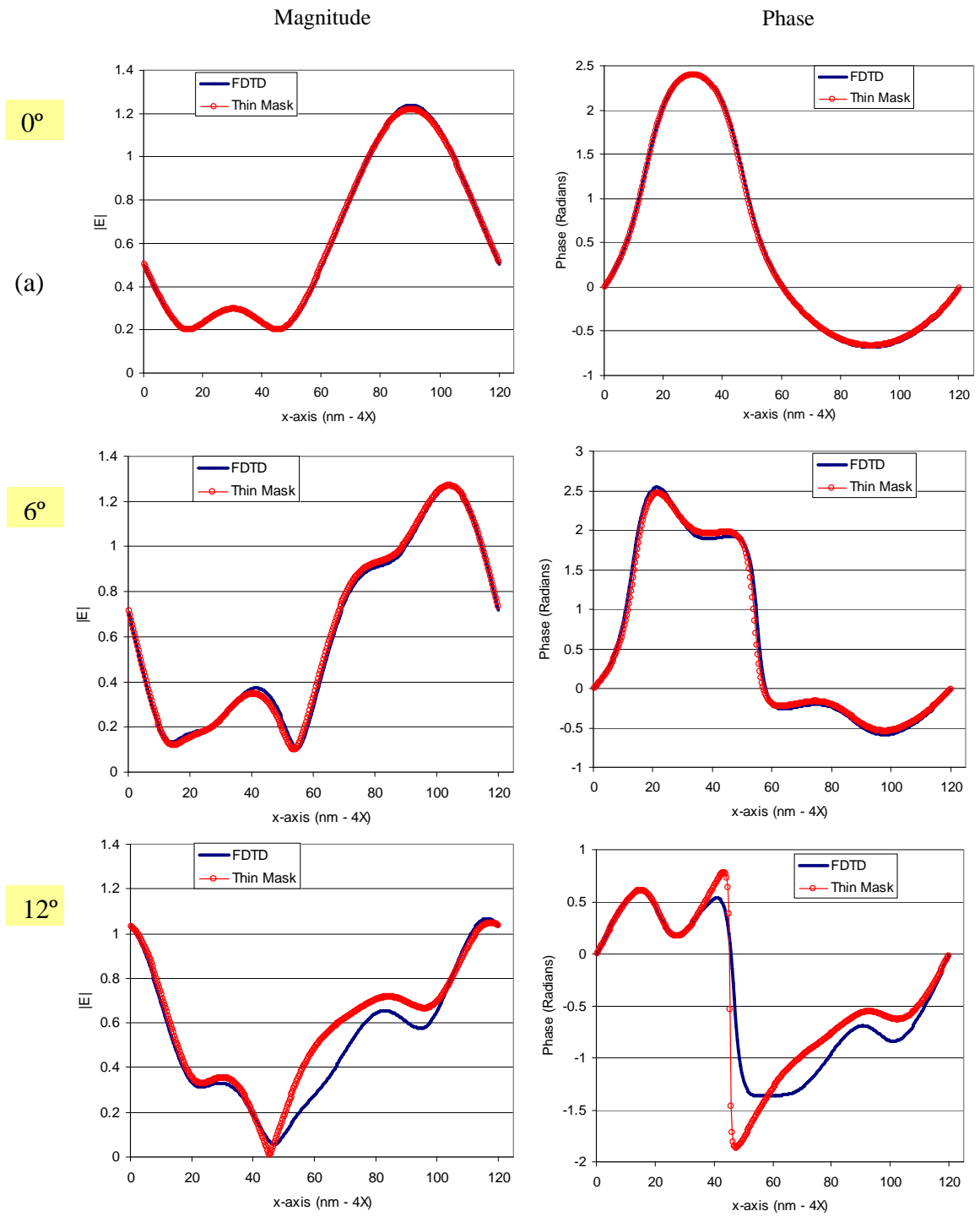Magnitude   Phase

Figure 8.13. Filtered (NA = 1.0), coherent, near field transmissions of a TE plane wave for various angles of incidence through line space patterns giving 15nm features on the wafer.

approach the more oblique 12º angles. While the TM data is not shown, the thin mask model works very well for this polarization as well.

The 22nm line and space pattern actually has dimensions of 88nm on the mask (4X magnification). Again, the near fields can be filtered down to an angular collection cone of about ±15º. Figure 8.12 shows the filtered near fields for the TE polarization for various angles of incidence on the mask. Once again, the thin mask model does an exceptional job of modeling the 0º and 6º angles, while the model becomes less accurate as the angles approach more oblique incidence. While the TM data is not shown, the thin mask model works very well for this polarization as well.

Finally, a very aggressive 15nm line and space pattern was tested which actually has dimensions of 60nm on the mask (4X magnification). Figure 8.13 shows the filtered (±15º) near fields for the TE polarization at various angles of incidence on the mask. Even at these very small feature sizes, the thin mask model predicts the filtered near fields very well for the 0º and 6º fields, while the 12º fields become significantly prone to errors. While the TM data is not shown, the thin mask model works very well for this polarization as well.

The above examples show that a simplified model for absorber feature transmission can be implemented and have extremely good accuracy. All the structures tested began to lose accuracy as the angles approached more oblique 12º. Most likely the simple point source model begins to break down at higher angles of incidence, and a
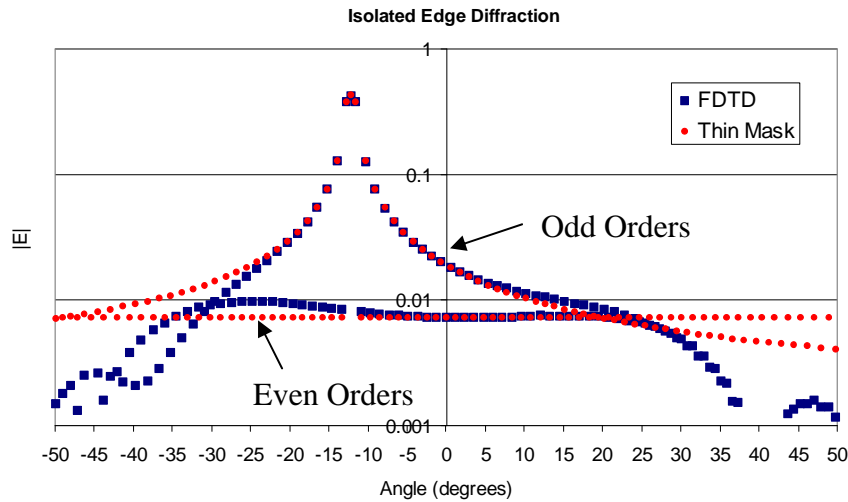
Figure 8.14. Angular spectrum of cut lines for two absorber edges very far apart for both FDTD and the thin mask model.

more complicated model that takes into account the angular dependency of the point source will have to be implemented if higher accuracy is desired. To confirm this, an isolated edge illuminated at 12º incidence can be use to observe what happens to the even orders. Figure 8.14 shows the magnitude of the diffracted spectrum from the isolated edge with a 12º incident plane wave. The even orders begin to become asymmetrical for off-axis illumination and this is a likely cause for the errors observed in the above examples. The examples also show absorber edges on EUV masks can be modeled as independent edges with very little interactions on a single transmission through the features. Dense line and space features down to 15nm were shown to be sufficiently independent to allow the thin mask model to accurately approximate the transmission.

As a final proof of concept, the total reflection from a defect free 32nm line and space pattern will be calculated according to the procedure outlined in Figure 8.2 and

Line-Space Mask Transmission - 32nm Features

Line-Space Mask Transmission - 32nm Features
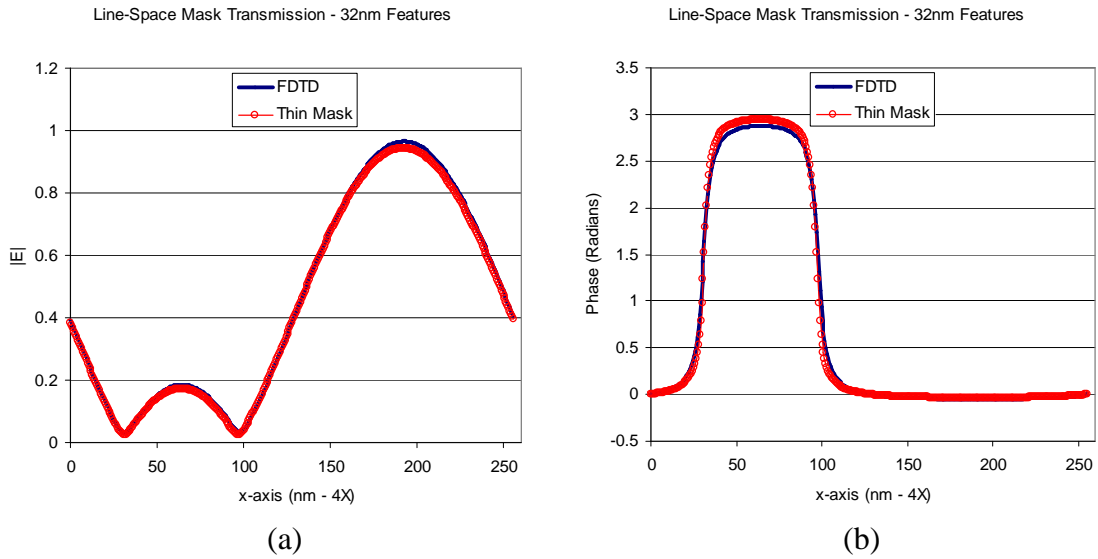
Figure 8.15. Full reflection from a 32nm line and space pattern for FDTD and the thin mask model linked to analytic calculations of reflection from a perfect multilayer structure. (a) Magnitude, (b) Phase.

compared to a full FDTD simulation for the same pattern. Figure 8.15 shows the final reflected electric fields which have been filtered down to only those waves entering a 4X system centered at 0° with an NA = 0.4. Clearly, the thin mask model and FDTD are agreeing very well, and so this method for simulating features has been verified.

8.5 Inspection Simulations

Inspection simulations present a vastly different scattering environment compared to exposure wavelengths since the material properties (see beginning of Chapter 8) of the multilayer are significantly changed at optical (488nm or 266nm) wavelengths. For instance, the top surface of the capping layer is now responsible for about 85% of the observed reflection coefficient. The top layer's importance is due to a significantly larger refractive index contrast between air and the capping layer, and also that optical

wavelengths entering the multilayer experience a 5-50X smaller skin depth (more decay) than at EUV wavelengths. Therefore, it is only the top few bilayers that actually contribute any significant part of the total reflection.

Inspection simulations are always challenging since the imaging systems operate at 1X and typically have very large NAs. The resulting angular collection cone is very wide and nearly all propagating orders must be computed correctly. This need for highly accurate results across all angles of propagation might severely constrain the implementation of a simple and fast method to model inspection. Aside from this concern, an investigation into the 3 key assumptions of the ray tracing method is needed to really understand whether it is sufficient to simulate the reflection in this changed material environment. The first key assumption that the forward diffraction is negligible has not changed. This assumption relied on the inverse nature of the two surfaces within the bilayer, which is directly related to the geometry. Since, only the scattering wavelength has changed in inspection simulations, this key assumption has not been violated.

Second, the ray tracing method assumed that multiple back scattering was negligible. This assumption relied on the fact that the largest multiple back scatter event had to undergo at least 2 more reflections relative to the primary reflection. So the magnitude of these events would scale as ρ^2 in the worst case. The reflection coefficients for the interfaces in the multilayer are about 7X larger than at EUV wavelengths, resulting in multiple back scatter events that are likely 50X larger. This increase is tempered, however, by knowledge that the first layer is responsible for 85% of the observed reflection coefficient, which makes it impossible for a majority of the energy to

even enter the multilayer and undergo multiple back scatter events. Additionally, the skin depth of the multilayer materials at these optical wavelengths is 5-50X shorter than at EUV wavelengths. This creates an environment where it is very difficult for light to move large distances inside the multilayer and retain its energy, limiting multiple reflections inside the stack. The shorter skin depth and larger reflection at the top surface act in conjunction to allow multiple back scatter events to be ignored.

The third and final key assumption is that resonance can be anticipated and analytically corrected for inside the stack. Nothing physical has changed to compromise this assumption and it can easily be accomplished. The shorter skin depths discussed in the previous paragraph also help to cut the efficiency of resonance in the multilayer such that the resonance conditions have not changed too dramatically from that seen at EUV wavelengths.

The accuracy of TEMPEST, the ray tracing method, and the SSA were all tested on a buried Gaussian defect that was 100nm high with a 100nm FWHM. The defect was coated with the smoothing process resulting in a peak disturbance of 15nm on the top surface of the multilayer. Each of the three simulation methods were then used to calculate the reflected fields. Figure 8.16 shows the near reflected fields, filtered down to all propagating waves (NA=1.0, 1X) for the FDTD and ray tracing methods. The SSA method is producing nearly identical results as the ray tracing method and is not shown. The similarity between the SSA and the ray tracing results at inspection wavelengths is expected since so much of the reflection coefficient is dependent on the top surface. All methods appear to be giving reasonably similar results. Once again, an inconsistency exists between the background level that FDTD is predicting compared to the ray tracing
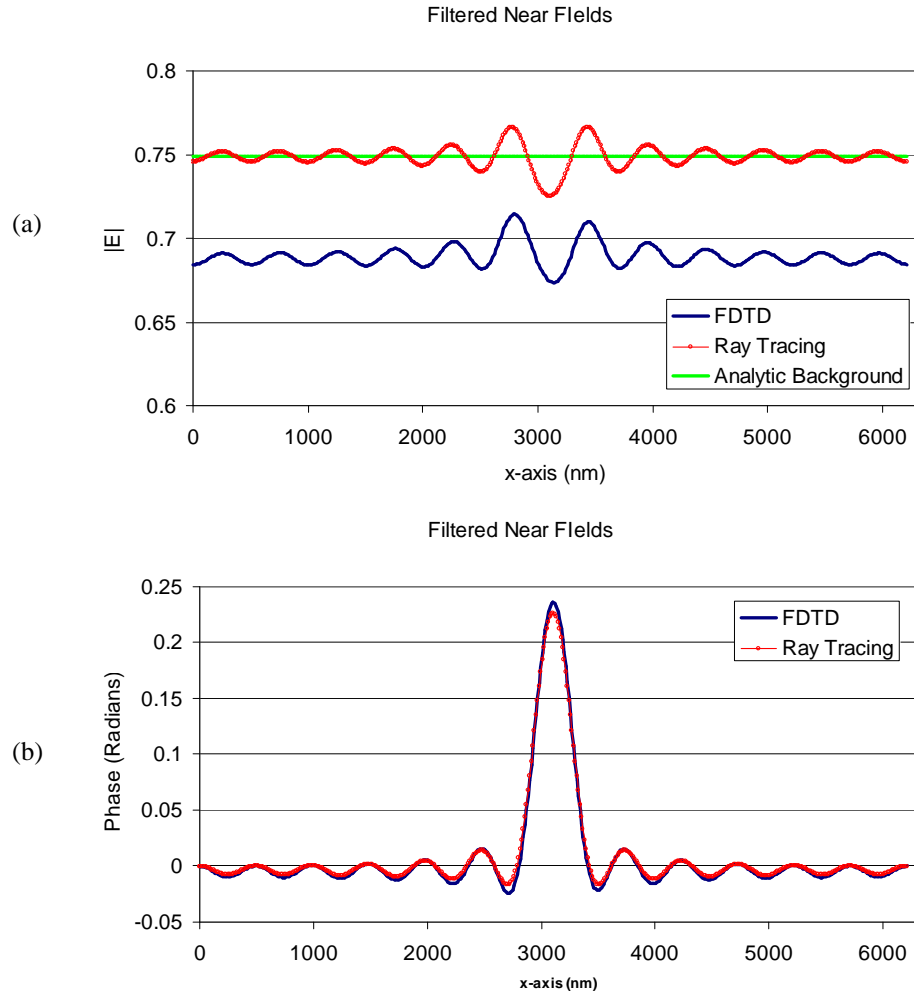
Figure 8.16. Filtered near fields of 100nm high Gaussian defect with 100nm FWHM imaged at λ=488nm. (a) magnitude, (b) phase.

method. To understand which background level is more accurate, the analytic

background electric field was calculated and is plotted in Figure 8.16a. Clearly, the ray

tracing methodology is calculating the background level more accurately than FDTD.

The discrepancy of the FDTD results likely stems from the unusually high cell density

(~700 cells/wavelength) that inspection simulations must operate at to accurately describe

the multilayer geometry. The extremely high cell densities might allow roundoff errors to
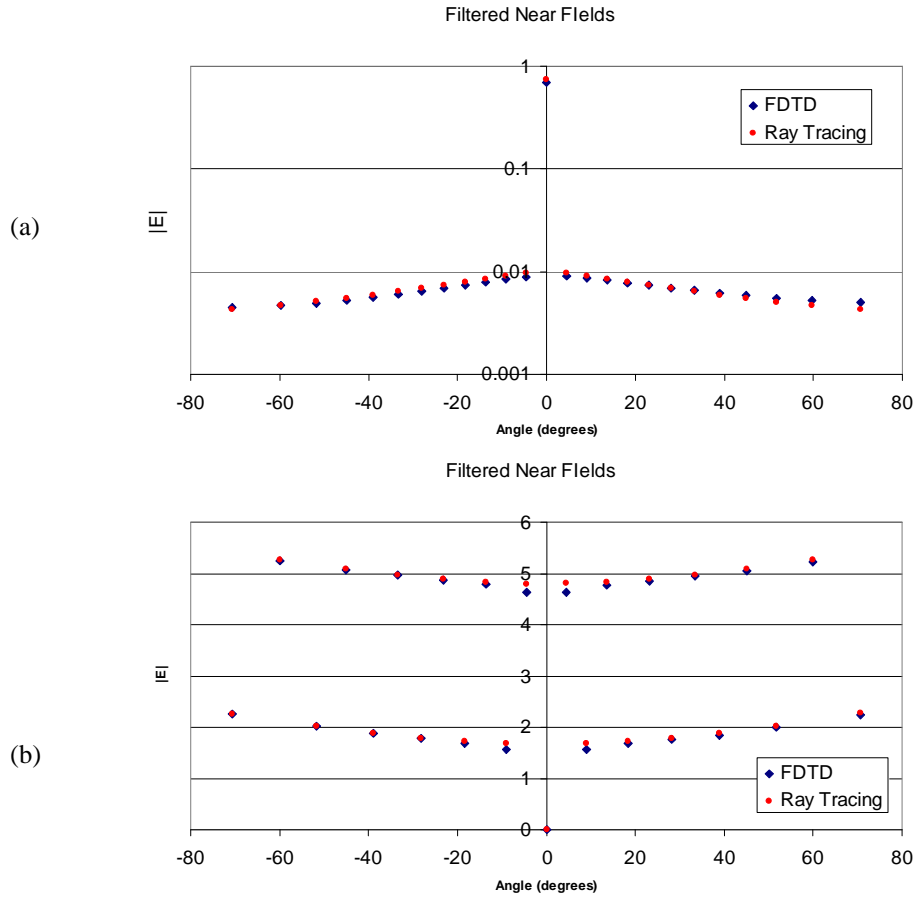
Figure 8.17. Plots of the filtered near field spectrum for all propagating waves scattered from a 100nm high Gaussian defect with a FWHM of 100nm coated with the smoothing process. (a) Magnitude, (b) phase.

significantly increase when subtracting neighboring cells that have electric fields that are too similar due to their close proximity.

Another issue with the FDTD data is that there is an asymmetry to the reflection coming from a perfectly symmetric scattering object. The asymmetry shows up more clearly in the diffracted orders shown in Figure 8.17. The FDTD spectrum is tilted with respect to the spectrum from the ray tracing method, which is perfectly symmetric. The asymmetry is therefore due to some numerical noise within the FDTD algorithm or possibly due to the staggered electric field grid that FDTD uses for updating the E and H

fields. Because of these inconsistencies, the ray tracing method and the SSA are believed to be more accurate than FDTD for simulating the case for inspection. Also, since SSA and the ray tracing methodology are giving nearly identical results, the SSA method should probably be used because of its simple implementation.

8.6 Conclusions

A complete methodology was proposed for simulating the impact of buried defects on absorber feature printability. The methodology relied on breaking the full EUV scattering problem into two simpler parts: 1) a transmission through the absorber features, and 2) the reflection from a non-planar multilayer. The buried defect simulator proposed in Chapter 5 clearly solves the second part of the scattering problem. A simplified thin mask transmission model was introduced to solve the first part of the scattering problem. The thin mask model was derived from investigations of the physical edge scattering associated with a thick (~5λ) mask. Studies of the additional physical contributions from edges showed to first order, that only one out of the four observed physical effects contribute non-negligble energy to the final transmitted fields. The response fields could therefore be accurately approximated in the thin mask model by only including point sources that scatter from the top corners of the absorber material. The thin mask model must also be propagated vertically to account for the mask thickness. The magnitude and phase of the modeled point sources can be characterized based on the type and thickness of material used for the absorber. Additionally, the

vertical propagation distance must be characterized based on the same parameters, but is expected to be about half the mask thickness.

The thin mask model was tested on the transmissions through 32nm, 22nm, and 15nm (wafer dimensions) line and space patterns to confirm its accuracy. The thin mask model works very well for all of the line and space patterns, demonstrating that it should be sufficient to model absorber features for a few generations. However, the accuracy of the model does depend fairly strongly on the angle of incidence on the mask. For angles approaching about 12º incidence, the thin mask model begins to predict some erroneous results, but still gives a generally good idea of the behavior that can be expected. The breakdown of the method is likely do to the simple model used for the point sources at the corners of the mask. Asymmetries in the scattering of the point sources begin to occur at larger angles of incidence, and these effects will need to be modeled to achieve more accuracy at these oblique angles.

This Chapter only offered a proof of concept that feature transmissions could be linked into the multilayer reflection. Much work is still needed to be done to characterize the material and thickness effects of the mask absorber on the generation of the thin mask model. More detailed studies will also need to be performed to investigate the accuracy of linking the features to the multilayer reflection. Specifically, whether resonance between the absorber features and the multilayer can be ignored, and whether []. Investigations into the numerical dispersion of FDTD and its effect on propagation through a thick absorber feature and the reflection from the multilayer will need to be accomplished to better understand sources of error when comparing the linked fields with FDTD simulations.

Finally, the buried defect simulator was shown to accurately calculate the reflection from EUV mask blanks during simulated inspection cases. In fact, the ray tracing method is believed to be more accurate than FDTD due to erroneous background level and asymmetries observed in the FDTD data. The SSA also was tested, giving nearly identical results with the ray tracing method. The similarities between the SSA and the ray tracing method are due to the fact that 85% of the reflection coefficient from the multilayer stack is due to the top surface alone. This regime allows the SSA to model the inspection reflections very well, despite its limitations in other areas.

9   Conclusions

The fast simulation methods described within this dissertation will provide a significant enhancement to the modeling tools used for better understanding the printability of phase defects in photomasks for DUV and EUV lithography. The greatly improved speed will allow more thorough printability studies to be performed, while retaining the detailed accuracy needed for predicting small perturbations in CD.

Each of the new methods began by breaking the physical scattering problem into smaller pieces and isolating the physics of each phenomenon. The individual pieces could then be analyzed to understand the magnitude of their impact on the final solution. Those pieces whose impact were minimal could then be removed from the process and simple models for the remaining components could be linked together to produce a final model. In this sense, each of the methods described here are approximate models that capture only the necessary physics that pertain to each application. Their broad application to other areas of engineering and science might be limited by this customized strategy; however, the customization of each method has allowed tremendous gains in speed that might not otherwise be possible. There exists a tradeoff in speed between a more customized solution and a more general solution for a larger class of problems.

This dissertation provided a better physical understanding of DUV phase defect behavior by investigating the differences found by Adam[7] between thin mask model defects and rigorously modeled defects. The differences were found to be physically

linked by the three-parameter algebraic models proposed by Neureuther and Mastromarco [25,26,27], and these models were extended to incorporate these differences. The degeneracy of phase defects at sub-wavelength dimensions allowed a systematic method for extracting new thin mask model parameters that could be used to capture the same electromagnetic behavior as rigorously modeled defects. This equivalence could then be used to rapidly simulate the effects of a given defect without resorting to a rigorous simulation tool.

Domain Decomposition Methods were extended to model inspection simulations, where the implementation of edge-DDM is complicated by the high NA and 1X imaging system of inspection tools. A Corner Error Function (CEF) was introduced into the edge-DDM library to allow the simulated errors to be reduced by as much as 60% compared to traditional edge-DDM when simulating inspection. A significant portion of the calculated error for both edge-DDM and corner-DDM was shown to stem from highly oblique TE waves that are a result of the inability of rigorous simulations to isolate the structure of interest. The error estimates for DDM when applied to inspection are therefore conservative in nature, and are likely significantly lower when synthesizing the fields of isolated structures.

The defect projector method was introduced to rapidly sift non-critical defects from a host of possible locations. It can predict the CD change of features containing defects to within 30% of rigorous simulations (worst case), but can be expected to perform much better in general. The defect projector can be combined with edge-DDM to produce an extremely fast and reliable simulation tool for modeling defective DUV photomasks.

The largest contributions of this dissertation are the methodologies developed for simulating EUV photomasks. The electrically large nature of an EUV photomask combined with the seemingly complex interactions within the multilayer have made the problem difficult to handle in the past. The buried defect simulator presented in the dissertation is as accurate at predicting defect printability when compared to more rigorous methods like FDTD. The hybrid method combines ray tracing and Fourier optics to understand the scattering that occurs from non-planar surfaces inside a resonant cavity. The ability to neglect forward scattering, neglect multiple back scattering, and analytically anticipate the resonance conditions inside the multilayer have produced an effective and efficient method for assessing a buried defect's printability impact. The method is extremely robust, correctly predicting the printability of very large and small defects, coated with a variety of deposition techniques.

The ray tracing method is not without its limits. Some of the underlying assumptions begin to break down as the buried defect is placed higher in the multilayer. The extension of the method to handle these defects would be nice addition to its capabilities. While the defective layers become more seriously contorted as the defect nears the surface, the rest of the multilayer is unperturbed by the defect's presence and may lead to a simplification of the physics needed to model these defects.

A detailed analysis of the FDTD method was investigated when applied to the EUV scattering problem. Significant new challenges were uncovered that amplify the already demanding computational difficulties with simulating EUV structures. The resonant multilayer undergoes temporary convergence lulls on its path to equilibrium which can cause TEMPEST to mistakenly predict convergence, resulting in incorrect

results. Numerical dispersion inside the FDTD algorithm also causes a small (0.2%) shift in the simulated wavelength. This wavelength shift is usually imperceptible in DUV applications, but its effect is amplified in EUV photomasks due to the resonance within the multilayer structure which makes the stack extremely sensitive to small wavelength changes. The net result is that FDTD results can predict significantly incorrect reflection coefficients for a given multilayer stack at angles greater than about 10°. The ray tracing methodology is therefore believed to be more accurate for this application.

Defect landscape maps were calculated to aid in predicting buried defect tolerances for the manufacturing of EUV mask blanks. A defect's initial volume was found to play a crucial role in determining whether the defect would be printable. The smoothing process thus provides an excellent means to decrease the printability of a buried defect.

The printability of a defect was also found to be very sensitive to the shape and growth of the multilayer interfaces. This dissertation used the growth model developed by Stearns [42]. To the extent that this model accurately predicts the bilayer growth over the defect, the printability maps should be accurate. However, the clipping effects observed on standard coated defects are probably physically incorrect. Also, it is unlikely that extremely high aspect ratio defects actually exist on EUV mask blanks, and is unknown whether the smoothing growth model correctly predicts the defect evolution of such defects. The buried defect simulator is highly accurate relative to FDTD on the structures simulated, but future work in EUVL will need to verify that a robust and accurate growth model exists so that the simulated structures are indeed correct.

Various extensions to the buried defect simulator were presented, including a method for solving the full EUV scattering problem. The buried defect simulator could be linked directly into a near field transmission simulator to accurately predict the printability of 2D features in the presence of 2D defects. Investigations of the physical scattering of an isolated absorber edge were used to understand the essential physics that needed to be captured into a transmission model. These investigations resulted in a simplified thin mask model for the transmission through the electrically thick absorber features. The thin mask model gives accurate results even for dense line and space patterns of 15nm (wafer dimensions). This model incorporated a simple model for point sources located at the top corner of absorber edges.

A significant amount of work can still be accomplished in this area. The proposed thin mask model was only tested in 2D as a proof of concept, and investigations need to be performed to understand its extendibility to 3D features. Characterizations of the physical effects associated with scattering from a 3D corner will need to be performed. Additionally, a more intelligent model for the top corner point sources could be used to eliminate some of the errors predicted in the thin mask model at more oblique angles of incidence (~12º). Investigations need to be performed to show whether the effects of resonance between the mask absorber and the multilayer can truly be neglected. Also, a better understanding of the errors in FDTD and their impact on the final observed reflection will give a greater understanding of the sources of differences between the calculated fields that can be used to better ascertain the accuracy of the method.

Finally, the last extension of the buried defect simulator is to the case of optical inspection. The large jump in wavelength relative to EUV wavelengths results in a

significantly different scattering environment. The refractive index contrast is very large

at the top surface of the capping layer, resulting in the top surface producing 85% of the

reflection coefficient from the entire structure. Additionally, the skin depths of the

materials at the larger optical wavelengths have decreased by 5-50X, resulting in a

tremendous amount of decay upon propagation inside the multilayer. None of the 3 key

assumptions of the ray tracing methodology are violated in this regime, allowing it to

successfully model the reflection from EUV mask blanks at optical wavelengths. Both

the SSA and ray tracing give nearly identical results for the calculated reflection, as

expected since the top surface is responsible for 85% of the reflection coefficient. In fact,

both methods produce results that are believed to be more accurate than FDTD since

background level inconsistencies and asymmetries were observed in the FDTD data.

References

1. N. Cobb, "Fast Optical and Process Proximity Correction Algorithms for Integrated Circuit Manufacturing." Ph.D. Dissertation, University of California at Berkeley, 1998.

2. Adam, K. and A.R. Neureuther. "Algorithmic implementations of domain decomposition methods for the diffraction simulation of advanced photomasks." Proceedings of Spie, vol.4691, 2002, pp.107-24.

3. Erdmann, A., et al. "Efficient simulation of light diffraction from three-dimensional EUV masks using field decomposition techniques." Proceedings of Spie, vol.5037, 2003, pp.482-93.

4. Tirapu-Azpiroz, J. and E. Yablonovitch. "Fast evaluation of photomask near-fields in subwavelength 193-nm lithography." Proceedings of SPIE, vol. 5377, 2004.

5. Gullikson, E.M., et al., "Practical approach for modeling extreme ultraviolet lithography mask defects." Journal of Vacuum Science & Technology B, 2002. 20(1): p. 81-6.

6. J.J. Sakurai, *Modern Quantum Mechanics*, (Addison-Wesley Publishing Company, 1994), p. 325.

7. Adam, K., S. Hotta, and A.R. Neureuther. "Characterization of phase defects in phase shift masks." Journal of Vacuum Science & Technology B, vol.18, no.6, Nov. 2000, pp.3227-31.

8. A. Wong, "Rigorous Three-Dimensional Time-Domain Finite-Difference Electromagnetic Simulation," Ph.D. Dissertation, University of California at Berkeley, 1994.

9. Nguyen, K.B., et al. "Printability of substrate and absorber defects on extreme ultraviolet lithographic masks." Journal of Vacuum Science & Technology B, vol.13, no.6, Nov.-Dec. 1995, pp.3082-8.

10. Ray-Chaudhuri, A.K., et al. "The use of programmed multilayer defects in validating a defect compensation strategy for EUV lithography." Proceedings of Spie, vol.3873, pt.1-2, 1999, pp.838-43.

11. Moonsuk, Y., et al. "Characterization of extreme ultraviolet lithography mask defects from extreme ultraviolet far-field scattering patterns." Journal of Vacuum Science & Technology B, vol.18, no.6, Nov. 2000, pp.2930-4.

12. Gullikson, E.M., et al., "Modeling the defect inspection sensitivity of a confocal microscope." Proceedings of SPIE, 2005. 5751(1): p. 1242-8.

13. Moonsuk, Y., et al. "'Actinic-only' defects in extreme ultraviolet lithography mask blanks-native defects at the detection limit of visible-light inspection tools." Appl. Phys. Japanese Journal of Applied Physics Part 1, vol.41, no.6B, June 2002, pp.4101-4. Japan.

14. Windt, D.L., et al. "EUV multilayers for solar physics." Proceedings of Spie, vol.5168, no.1, 2004, pp.1-11.

15. M. Born and E. Wolf, *Principles of Optics, 7th (Expanded) Edition*, (Cambridge University Press, 1999)

16. J.W. Goodman, *Introduction to Fourier Optics*, 2nd Edition, (McGraw-Hill, 1996)

17. J.W. Goodman, *Statistical Optics*, (John Wiley and Sons, 2000)

18. J. Sheats and B. Smith, eds., *Microlithography: Science and Technology*, Marcel Dekker, 1998.

19. P. Rai-Choudhury, ed., *Handbook of Microlithography, Micromachining, and Microfabrication*, SPIE Press, 1997.

20. J. Plummer, M. Deal, and P. Griffin. Silicon VLSI Technology: Fundamentals, Practice, and Modeling, (Prentice Hall, 2000)

21. A. Wong, *Resolution Enhancement Techniques in Optical Lithography*, SPIE Press, 2001.

22. F.M. Schellenberg, ed., *Selected Papers on Resolution Enhancement Techniques in Optical Lithography*, SPIE Press, 2001.

23. T. Pistor, "Electromagnetic Simulation and Modeling with Applications in Lithography." Ph.D. Dissertation, University of California at Berkeley, 2001.

24. Watanabe, H., et al. "Detection and printability of shifter defects in phase-shifting masks. II. Defocus characteristics." Japanese Journal of Applied Physics Part 1, vol.31, no.12B, Dec. 1992, pp.4155-60. Japan.

25. Neureuther, A.R., P. Flanner, III, and S. Shen. "Coherence of defect interactions with features in optical imaging." Journal of Vacuum Science & Technology B, vol.5, no.1, Jan.-Feb. 1987, pp.308-12.

26. Mastromarco, V., A.R. Neureuther, and K. Toh. "Printability of defects in optical lithography: polarity and critical location effects." Journal of Vacuum Science & Technology B, vol.6, no.1, Jan.-Feb. 1988, pp.224-9.

27. Neureuther, A.R. "Modeling phase shifting masks." Proceedings of Spie, vol.1496, 1991, pp.80-8.

28. K. Toh, "Two Dimensional Images with Effects of Lens Aberrations in Optical Lithography," M.S. Thesis, Memorandum #UCB/ERL M88/30, University of California at Berkeley, May 1988.

29. Attwood, D., *Soft X-rays and extreme ultraviolet radiation: principles and applications*, (Cambridge University Press, 1999), pp.404.

30. Pistor, T. and A.R. Neureuther. "Calculating aerial images from EUV masks." Proceedings of Spie, vol.3676, pt.1-2, 1999, pp.679-96.

31. Kittel, C., *Introduction to Solid State Physics*, (John Wiley and Sons 1996), p.29.

32. P. Kearney, et al. "Overcoming substrate defect decoration effects in EUVL mask blank development." Proceedings of SPIE, vol. 5567, 2004.

33. Barty, A., et al. "EUVL mask blank repair." Proceedings of Spie, vol.4688, pt.1-2, 2002, pp.385-94.

34. Hau-Riege, S.P., et al. "Defect repair for extreme-ultraviolet lithography (EUVL) mask blanks." Proceedings of Spie, vol.5037, 2003, pp.331-8.

35. Mirkarimi, P.B., et al., "Method for repairing Mo/Si multilayer thin film phase defects in reticles for extreme ultraviolet lithography." Journal of Applied Physics, 2002. 91(1): p. 81-9.

36. Ray-Chaudhuri, A.K., et al. "Method for compensation of extreme-ultraviolet multilayer defects." Journal of Vacuum Science & Technology B, vol.17, no.6, Nov. 1999, pp.3024-8.

37. Mirkarimi, P.B. and D.G. Steams, "Investigating the growth of localized defects in thin films using gold nanospheres.*"* Applied Physics Letters, 2000. 77(14): p. 2243-5.

38. Ray-Chaudhuri, A.K., A.C. Fisher, and E.M. Gullikson. "Defect printability modeling of smoothed substrate defects for EUV lithography." Proceedings of Spie, vol.4186, 2001, pp.781-6.

39. Cardinale, G.F., et al. "Effects of smoothing on defect printability at extreme ultraviolet wavelengths." Journal of Vacuum Science & Technology B, vol.18, no.6, Nov. 2000, pp.2944-9.

40. Mirkarimi, P.B., et al., "An ion-assisted Mo-Si deposition process for planarizing reticle substrates for extreme ultraviolet lithography." IEEE Journal of Quantum Electronics, 2001. 37(12): p. 1514-16.

41. Mirkarimi, P.B., et al., "Developing a viable multilayer coating process for extreme ultraviolet lithography reticles." Journal of Microlithography, Microfabrication, & Microsystems, 2004. 3(1): p. 139-45.

42. Stearns, D.G., P.B. Mirkarimi, and E. Spiller, "Localized defects in multilayer coatings." Thin Solid Films, 2004. 446(1): p. 37-49.

43. T. Pistor, A.R. Neureuther, R.J. Socha, "Modeling oblique incidence effects in photomasks." Proceedings of SPIE, vol. 4000, 2000.

44. Y. Lin and J. Bokor, "Minimum critical defects in extreme-ultraviolet lithography masks." Journal of Vacuum Science & Technology B, vol.15, no.6, Nov. 1997, pp.2467-2470.

45. Brukman, M.J., D. Yunfei, and A.R. Neureuther. "Simulation of EUV multilayer mirror buried defects." Proceedings of Spie, vol.3997, 2000, pp.799-806. USA.

46. Pistor, T. and A. Neureuther. "Extreme ultraviolet mask defect simulation." Journal of Vacuum Science & Technology B, vol.17, no.6, Nov. 1999, pp.3019-23.

47. Pistor, T., D. Yunfei, and A. Neureuther. "Extreme ultraviolet mask defect simulation: Low-profile defects." Journal of Vacuum Science & Technology B, vol.18, no.6, Nov. 2000, pp.2926-9.

48. Y. Deng, "Modeling Innovations in EUV and Nanoimprint Lithography," Ph.D. Dissertation, University of California at Berkeley, 2005.

49. Pistor, T.V., K. Adam, and A. Neureuther. "Rigorous simulation of mask corner effects in extreme ultraviolet lithography." Journal of Vacuum Science & Technology B, vol.16, no.6, Nov.-Dec. 1998, pp.3449-55.

50. Ito, M., et al., "Simulation of multilayer defects in extreme ultraviolet masks." Japanese Journal of Applied Physics Part 1, 2001. 40(4A): p. 2549-53.

51. Evanschitzky, P. and A. Erdmann. "The impact of EUV mask defects on lithographic process performance." Proceedings of Spie, vol.5504, no.1, 31 Dec. 2003, pp.111-19.

52. Evanschitzky, P. and A. Erdmann. "Enhanced model for the efficient 2D and 3D simulation of defective EUV masks." Proceedings of Spie, vol.5374, no.1, 2004, pp.770-9.

53. Evanschitzky, P., et al. "Simulation of extreme ultraviolet masks with defective multilayers." Proceedings of Spie, vol.5130, no.1, 26 Aug. 2003, pp.1035-45.

54. Sambale, C., et al. "Rigorous simulation of defective EUV multilayer masks." Proceedings of SPIE, vol. 5256, 2003.

55. P. Schiavone, G. Granet and J. Y. Robic, "Rigorous electromagnetic simulation of EUV masks: influence of the absorber properties", Microelectronic Engineering, Volumes 57-58, September 2001, Pages 497-503.

56. Besacier, M., et al. "Modeling of the influence of the defect position on the reflected intensity in EUV mask." Proceedings of SPIE, vol. 5751, 2005.

57. Seong-sue, K., et al., "Defect printability and defect inspection simulations of patterned EUVL mask using rigorous coupled-wave analysis." Proceedings of Spie, 2005. 5751(1): p. 697-705.

58. Besacier, M., et al. "The Rayleigh method applied to EUV lithography simulation." Proceedings of SPIE, vol. 5037, 2003.

59. Bollepalli, B.S. and F. Cerrina. "On the computation of reflected images from extreme ultraviolet masks." Proceedings of Spie, vol.3676, 1999, pp.587-97.

60. Bollepalli, S.B., M. Khan, and F. Cerrina. "Modeling image formation in layered structures: application to X-ray lithography." Modeling and Simulation of Microsystems, Semiconductors, Sensors and Actuators. Computational Publications. 1998, pp.53-8. Cambridge, MA,

61. Yunfei, D., T. Pistor, and A.R. Neureuther. "Models for characterizing the printability of buried EUV defects." Proceedings of Spie, vol.4343, 2001, pp.551-8.

62. Adam, K. and A.R. Neureuther. "Methodology for accurate and rapid simulation of large arbitrary 2D layouts of advanced photomasks." Proceedings of Spie, vol.4562, 2002, pp.1051-67. USA.

63. Adam, K. and A.R. Neureuther. "Simplified models for edge transitions in rigorous mask modeling." Proceedings of Spie, vol.4346, pt.1-2, 2001, pp.331-44.

64. Adam, K. "Modeling of electromagnetic effects from mask topography at full-chip scale." Proceedings of Spie, vol.5754, no.1, 2004, pp.498-505.

65. Pierrat, C., et al. "Phase-shifting mask topography effects on lithographic image quality." Proceedings of Spie, vol.1927, pt.1, 1993, pp.28-41.

66. V.A. Borovikov, *Geometrical theory of diffraction*, (Institute of Electrical & Electronics Engineering, 1994)

67. Center for X-Ray Optics (CXRO), Lawrence Berkeley National Laboratory, http://www-cxro.lbl.gov/optical_constants/getdb2.html

68. Socha, R.J., A.R. Neureuther, and R. Singh, "Models for characterizing phase-shift defects in optical projection printing." IEEE Transactions on Semiconductor Manufacturing, 1995. 8(2): p. 139-49.

69. Lam, M. and A. Neureuther, "Algebraic model for the printability of nonplanar phase defects." Journal of Vacuum Science & Technology B (Microelectronics and Nanometer Structures), 2003. 21(6): p. 2815-20.

70. A. Taflove, *Computational Electrodynamics: The Finite-Difference Time – Domain Method* (Artech House, Norwood, MA, 1995).

71. Pistor, T.V. "Accuracy issues in the finite difference time domain simulation of photomask scattering." Proceedings of SPIE, vol. 4346, 2001.

72. Ma, Andy, et. al. "Progress towards the development of a commercial tool and process for EUVL mask blanks." Proceedings of SPIE, 5751, 2005.

73. Nicolle, C. Charpin, et al. "A new absorbing stack for EUV masks." Proceedings of SPIE, 5567, 2004.